Modeling and State Estimation of Lithium-Ion Battery Packs for Application in Battery Management Systems

by

Manoj Mathew

A thesis
presented to the University of Waterloo
in fulfillment of the
thesis requirement for the degree of
Doctor of Philosophy
in
Chemical Engineering

Waterloo, Ontario, Canada, 2018

Examining Committee Membership

The following served on the Examining Committee for this thesis. The decision of the Examining Committee is by majority vote.

External Examiner	Professor Jennifer Bauman Electrical & Computer Engineering, McMaster University
Supervisor(s)	Professor Michael Fowler Chemical Engineering, University of Waterloo
Internal Member	Professor Jeff Gostick Chemical Engineering, University of Waterloo
Internal-external Member	Professor Roydon Fraser Mechanical and Mechatronics Engineering. University of Waterloo
Other Member(s)	Professor Michael Pope Chemical Engineering, University of Waterloo

AUTHOR'S DECLARATION

This thesis consists of material all of which I authored or co-authored: see Statement of Contributions included in the thesis. This is a true copy of the thesis, including any required final revisions, as accepted by my examiners

I understand that my thesis may be made electronically available to the public.

Statement of Contributions

In Chapter 3, the author was responsible for developing the comprehensive cell model, conducting thermal experiments, carrying out the simulations, preparing the results, graphs and manuscript. Mehrdad Mastali, John Catton, Ehsan Samadani, Stefan Janhunen and Michael Fowler offered advice and guidance, while Mehrdad, John and Ehsan offered additional assistance with the experimental set-up.

In Chapter 4, the author was responsible for developing the resistance model and algorithms, conducting all experiments, carrying out the simulations, preparing the results, graphs and manuscript. Stefan Janhunen and Michael Fowler offered guidance on the research, while co-operative education undergraduate students Mahir Rashid and Frank Long helped in implementing the MATLAB code.

In Chapter 5, the author was responsible for developing the SOH model and algorithms, conducting all experiments, carrying out the simulations, preparing the results, graphs and manuscript. Stefan Janhunen and Michael Fowler offered guidance on the research.

Finally, in Chapter 7, the author was responsible for developing the cell replacement framework and algorithms, conducting experiments, carrying out the simulations, preparing the results, graphs and manuscript. Michael Fowler offered guidance on the research, while Quing Kong and Jake McGrory were co-operative education undergraduate student who assisted with implemented the code in MATLAB.

Abstract

As lithium-ion (Li-Ion) battery packs grow in popularity, so do the concerns of its safety, reliability, and cost. An efficient and robust battery management system (BMS) can help ease these concerns. By measuring the voltage, temperature, and current for each cell, the BMS can balance the battery pack, and ensure it is operating within the safety limits. In addition, these measurements can be used to estimate the remaining charge in the battery (state-of-charge (SOC)) and determine the health of the battery (state-of-health (SOH)). Accurate estimation of these battery and system variables can help improve the safety and reliability of the energy storage system (ESS). This research aims to develop high-fidelity battery models and robust SOC and SOH algorithms that have low computational cost and require minimal training data. More specifically, this work will focus on SOC and SOH estimation at the pack-level, as well as modeling and simulation of a battery pack.

An accurate and computationally efficient Li-Ion battery model can be highly beneficial when developing SOC and SOH algorithms on the BMS. These models allow for software-in-the-loop (SIL) and hardware-in-the-loop (HIL) testing, where the battery pack is simulated in software. However, development of these battery models can be time-consuming, especially when trying to model the effect of temperature and SOC on the equivalent circuit model (ECM) parameters. Estimation of this relationship is often accomplished by carrying out a large number of experiments, which can be too costly for many BMS manufacturers. Therefore, the first contribution of this research is to develop a comprehensive battery model, where the ECM parameter surface is generated using a set of carefully designed experiments. This technique is compared with existing approaches from literature, and it is shown that by using the proposed method, the same degree of accuracy can be obtained while requiring significantly less experimental runs. This can be advantageous for BMS manufacturers that require a high-fidelity model but cannot afford to carry out a large number of experiments.

Once a comprehensive model has been developed for SIL and HIL testing, research was carried out in advancing SOH and SOC algorithms. With respect to SOH, research was conducted in developing a steady and reliable SOH metric that can be determined at the cell level and is stable at different battery operating conditions. To meet these requirements, a moving window direct resistance estimation (DRE) algorithm is utilized, where the resistance is estimated only when the

battery experiences rapid current transients. The DRE approach is then compared with more advanced resistance estimation techniques such as extended Kalman filter (EKF) and recursive least squares (RLS). It is shown that by using the proposed algorithm, the same degree of accuracy can be achieved as the more advanced methods. The DRE algorithm does, however, have a much lower computational complexity and therefore, can be implemented on a battery pack composed of hundreds of cells.

Research has also been conducted in converting these raw resistance values into a stable SOH metric. First, an outlier removal technique is proposed for removing any outliers in the resistance estimates; specifically, outliers that are an artifact of the sampling rate. The technique involves using an adaptive control chart, where the bounds on the control chart change as the internal resistance of the battery varies during operation. An exponentially weighted moving average (EWMA) is then applied to filter out the noise present in the raw estimates. Finally, the resistance values are filtered once more based on temperature and battery SOC. This additional filtering ensures that the SOH value is independent of the battery operating conditions. The proposed SOH framework was validated over a 27-day period for a lithium iron phosphate (LFP) battery. The results show an accurate estimation of battery resistance over time with a mean error of 1.1% as well as a stable SOH metric. The findings are significant for BMS developers who have limited computational resources but still require a robust and reliable SOH algorithm.

Concerning SOC, most publications in literature examine SOC estimation at the cell level. Determining the SOC for a battery pack can be challenging, especially an estimate that behaves logically to the battery user. This work proposes a three-level approach, where the final output from the algorithm is a well-behaved pack SOC estimate. The first level utilizes an EKF for estimating SOC while an RLS approach is used to adapt the model parameters. To reduce computational time, both algorithms will be executed on two specific cells: the first cell to charge to full and the first cell to discharge to empty. The second level consists of using the SOC estimates from these two cells and estimating a pack SOC value. Finally, a novel adaptive coulomb counting approach is proposed to ensure the pack SOC estimate behaves logically. The accuracy of the algorithm is tested using a 40 Ah Li-Ion battery. The results show that the algorithm produces accurate and stable SOC estimates.

Finally, this work extends the developed comprehensive battery model to examine the effect of replacing damaged cells in a battery pack with new ones. The cells within the battery pack vary stochastically, and the performance of the entire pack is evaluated under different conditions. The results show that by changing out cells in the battery pack, the SOH of the pack can be maintained indefinitely above a specific threshold value. In situations where the cells are checked for replacement at discrete intervals, referred to as maintenance event intervals, it is found that the length of the interval is dependent on the mean time to failure of the individual cells. The simulation framework, as well as the results from this paper, can be utilized to better optimize Li-ion battery pack design in electric vehicles (EVs) and make long-term deployment of EVs more economically feasible.

Acknowledgements

I would also like to express my sincere gratitude to my industrial supervisor Stefan Janhunen and my academic supervisor Michael Fowler for their continuous support and guidance during my entire PhD program. In addition to the great deal of technical knowledge I have acquired under their supervision, I have also learned how to think critically, how to conduct myself professionally, and how to approach any challenge with fortitude and determination.

I would like to thank all the co-ops that have helped me during my PhD and to all my colleagues at the University of Waterloo including Muneendra Prasad, Ushnik Mukherjee, Ehsan Haghi, Manan Dosi, Mohamed Elsholkami, Zhiyu Mao, Zachary Cano, Navid Bismark, Zohiab Atiq Khan, Rubin Hille, John Catton, Emmanuel J Ogbe, Abdullah Al-Subaie, Mehrdad Mastali, Ehsan Samadani, Mohammad Farkhondeh, Satyam Panchal and Monu Malik. In addition, I want to thank my colleagues at Nuvation Engineering for helpful discussions. I am very thankful to all my friends at Waterloo for making my time here a very enjoyable experience.

I want to express my deepest gratitude to my family starting with my fiancée, Katherine Laycock. I will always remember the nights we spend working together at the university, including the times when you didn't have work but just wanted to keep me company. You have always been my greatest supporter and my best friend and this thesis would not have been possible without you. Finally, I am so grateful to my parents and my sister for their constant love and support through the four years.

Table of Contents

List of Figures

List of Tables

List of Symbols

A_{cs} = Cross-sectional area where heat transfer occurs[m^2]

$\hat{A}_k$ = The matrix that relates the state and the inputs to its derivative. The hat represents the EKF approximation

C_{EOL} = The capacity of the battery at its end of life [Ah]

C_{fresh} = The battery capacity for a fresh cell [Ah]

C_{min} = The battery capacity for the cell that will discharge to empty first

C_{max} = The battery capacity for the cell that will charge to full first

C_n = The estimated capacity of a single battery [Ah]

C_p = The estimated capacity of a battery pack [Ah]

C_{rated} = Rated capacity of a battery [Ah]

C_{SOH} = The battery capacity used in SOH calculations. [Ah]

C_{sp} = Specific heat capacity [J/kg˚C]

C_1 = Thevenin capacitance [F]

$\hat{C}_k^{\theta}$ = The matrix that relates the measurement and inputs to the state. The hat represents the EKF approximation

$Cap_{discharge}$ = The amount of charge that was discharged [Ah]

$Cap_{\,min\_c}$ = The minimum amount of charge before the battery is full [Ah]

$Cap_{\,min\_r}$ = The minimum amount of charge before the battery is empty [Ah]

$e_{EKF,k}$ = The error in the process equation for the Kalman filter

E_{ac} = The activation energy for the LMO degradation model [J mol^{-1}]

E_{rc} = The activation energy for the LMO degradation model [J mol^{-1}]

h_{∞} = Heat transfer coefficient [W/m^2˚C]

$L_{EKF,k}^{\theta}$ = The gain for the EKF algorithm

$L_{RLS,k}$ = The gain for the RLS algorithm

LL = Lower threshold for outlier removal in the SOH algorithm

I_L = Applied current [A]

I_{off} = Offset current used in the adaptive coulomb counting algorithm[A]

k = Constant used to represent time step

K_{const} = Constant used to tune the rate of convergence of the adaptive coulomb counting

m_c = The mass of a Li-ion battery [kg]

$M(SOC_k)$ = The cell hysteresis (V)

N_{rep} = Number of replicate runs

P_k = Covariance matrix for the parameters for the RLS algorithm

$\dot{Q}_{gen}$ = Heat generation within the cell [J/s]

$R_{CL,k}$ = The resistance used for determining the upper and lower thresholds.

R_{EOL} = The resistance of the battery at its end of life

$R_{\ filtered}$ = Resistance obtained after passing R_{inst} values through an EWMA

R_{fresh} = The resistance of a fresh battery

R_{inst} = Instantaneous resistance obtained after removal of outliers

R_0 = Ohmic resistance [Ω]

R_{ohm} = Ohmic resistance estimated using the direct resistance estimation algorithm

R_{SOH} = The resistance value used for SOH calculation

R_1 = Thevenin resistance used to describe the charge transfer resistance [Ω]

$r_{par,k}$ = Gaussian noise for the parameter EKF process equation

SOC = State of charge of an individual battery [%]

SOC_a = Final SOC value reported by the algorithm proposed in this work [%]

SOC_0 = Initial state of charge of a battery [%]

SOC_p = SOC value for a battery pack [%]

SOC_{min} = SOC value of the cell that will discharge to empty first [%]

SOC_{max} = SOC value of the cell that will charge to full first [%]

SOH_{Res} = State-of-health value obtained using resistance [%]

SOH_{Cap} = State-of-health value obtained using capacity [%]

$s_{p.e}^2$ = Pooled error variance

s_k = Used to represent the sign of the current

T_c = The temperature of the cell at the surface [˚C]

T_s = The sampling time of the measurement device

T_∞ = The ambient temperature of the environment [˚C]

t = Time [s]

u_k = Inputs into the Kalman filter

U_{exp} = Terminal voltage determined experimentally [V]

U_L = Model terminal voltage [V]

UL = Upper threshold for outlier removal in the SOH algorithm

U_{th} = The voltage drop across the first RC pair (Thevenin voltage) [V]

U_{ocv} = Open circuit voltage of an individual battery [V]

$\frac{dU_{OCV}}{dT_c}$ = Reversible heat generation term

v_k = The Gaussian noise used to describe the measurement equation in the Kalman filter

w_k = The Gaussian noise used to describe the process equation in the Kalman filter

X_{rep} = Replicated random variable

$\bar{X}_{rep}$ = Average of the replicated random variable

$\bar{X}$ = Average or moving average of a random variable

X = Design matrix for linear regression

x_k = The states or parameters in the EKF algorithm

$y_{EKF,k}$ = The measurement output from the EKF equations.

Greek Symbols

$\propto$ = Constant used to represent heat transfer coefficient

α_c = Used in the LMO degradation equation

β = Empirical Model Parameter vector

β_c = Used in the LMO degradation equation

τ = The time constant for the resistor-capacitor pair

ε = Small positive number used in hysteresis analysis

γ = Used to describe the decay of the hysteresis term

γ_c = Used in the LMO degradation equation

η = Coulombic efficacy of a battery

Δ = Change in a quantity

λ_{EWMA} = Constant used to represent depth of memory in an EWMA filter

$\lambda_{EWMA,CL}$ = Constant used to represent depth of memory in an EWMA filter for estimating the control chart bounds

$\lambda_{EWMA,LT}$ = Constant used to represent depth of memory in an EWMA filter with a small value of lamda to model long term noise attenuation

$\lambda_{EWMA,ST}$ = Constant used to represent depth of memory in an EWMA filter with a large value of lamda to model short term noise attenuation

λ_{RLS} = Constant used to represent the forgetting factor in the RLS algorithm

θ_{EKF} = Vector of state or parameters used in the extended Kalman filter

$\theta_{RLS,k}$ = Vector of parameters used in the RLS algorithm

Σ_r = Covaraince matrix for the parameter process equation

$\Sigma_{\tilde{\theta}}$ = Covaraince matrix for the parameters in the EKF algorithm

Σ_e = Covaraince matrix for the parameter measurement equation

Σ_w = Covaraince matrix for the state process equation

Σ_v = Covaraince matrix for the state measurement equation

$\Sigma_{\tilde{x},k}^{-}$ = Covaraince matrix for the states in the EKF algorithm

φ_k = The exogenous inputs in the auto-regressive model used in RLS

σ = Deviation from the mean. This is a configurable parameter in the SOH algorithm

List of Abbreviation

AEKF	Adaptive Extended Kalman Filter
ANFIS	Adaptive Neuro-Fuzzy Inference Systems
ANN	Artificial Neural Network
ARX	Auto-regressive Exogenous
BMS	Battery Management System
CCCV	Constant-Current Constant Voltage
CCD	Central Composite Design
DoD	Depth Of Discharge
DOE	Design of Experiments
DRE	Direct Resistance Estimation
ECM	Equivalent Circuit Model
EIS	Electrochemical Impedance Spectroscopy
EKF	Extended Kalman Filter
EOL	End Of Life
ESS	Energy Storage System
EWMA	Exponentially Weighted Moving Average
HEV	Hybrid Electric Vehicle
HIL	Hardware-in-the-loop
HPPC	Hybrid Pulse Power Characterization
HWFET	Highway Fuel Economy Test
ITDNN	Input Time-Delayed Neural Networks
LA	Lead Acid
LCO	Lithium Cobalt Oxide
LFP	Lithium Iron Phosphate

LMO	Lithium Magnesium Oxide
Li-Ion	Lithium-Ion
LUT	Look-up Table
NI	National Instruments
MSE	Mean Squared Error
MTTF	Meantime To Failure
NiMH	Nickel Metal Hydride
NMC	Lithium Nickel Manganese Cobalt Oxide
Non-DOE	Non-Design of Experiments
OCV	Open Circuit Voltage
ODE	Ordinary Differential Equation
PDE	Partial Differential Equation
PA	Particle Filter
PE	Portable Electronics
RBF	Radical Basis Function
RC	Resistor-Capacitor
RLS	Recursive Least Squares
RMSE	Root Mean Squared Error
PHEV	Plug-in Hybrid Electric Vehicles
SEI	Solid Electrolyte Interface
SIL	Software-in-the-loop
SMO	Sliding Mode Observer
SOC	State of Charge
SOH	State of Health
SPKF	Sigma Point Kalman Filter

UDDS	Urban Dynamometer Driving Schedule
UKF	Unscented Kalman Filter

Chapter 1: Introduction

As global fossil-fuel sources continue to deplete at a rapid rate, increased demand for renewable and sustainable alternative energy sources has become the new reality. One such source, lithium-ion (Li-ion) batteries, are emerging as a prominent energy storage device for applications in smart grid and electric vehicles [1]. They have a significant advantage to other battery chemistries such as lead acid (LA) and nickel metal hydride (NiMH), due to their high efficiency, large energy and power density and long service life [2], [3]. These properties make them ideal for use in electric vehicles (EV), plug-in hybrid electric vehicles (PHEV) and hybrid electric vehicles (HEV). In addition to their emergence in the automotive market, Li-ion batteries are also utilized in stationary or grid type applications [4]. For example, when the demand from the grid exceeds generation, Li-ion battery packs can augment power generation. On the other hand, when demand is lower than generation, the battery pack can be used to store excess energy.

For the applications described above, Li-Ion batteries are frequently combined in series and parallel configurations in order to satisfy the required energy and power demands. As the size of the battery pack grows, safe control and operation of the pack necessitates the use of a state of the art battery management system (BMS) [5]. The BMS must be able to monitor the voltage, temperature and current of each individual cell and utilize these measurements to provide safe and reliable control strategies under different operating conditions. In addition, the BMS is responsible for estimating battery states, such as state-of-charge (SOC) and state-of-health (SOH). A number of key decisions are made based on these two metrics and, therefore, accurate estimation of these two metrics is essential. The central focus of this thesis will be on improving SOC and SOH algorithms with regards to accuracy and computational time.

To provide an overview of energy storage systems (ESS) that utilize Li-ion batteries, consider Figure 1-1 below.

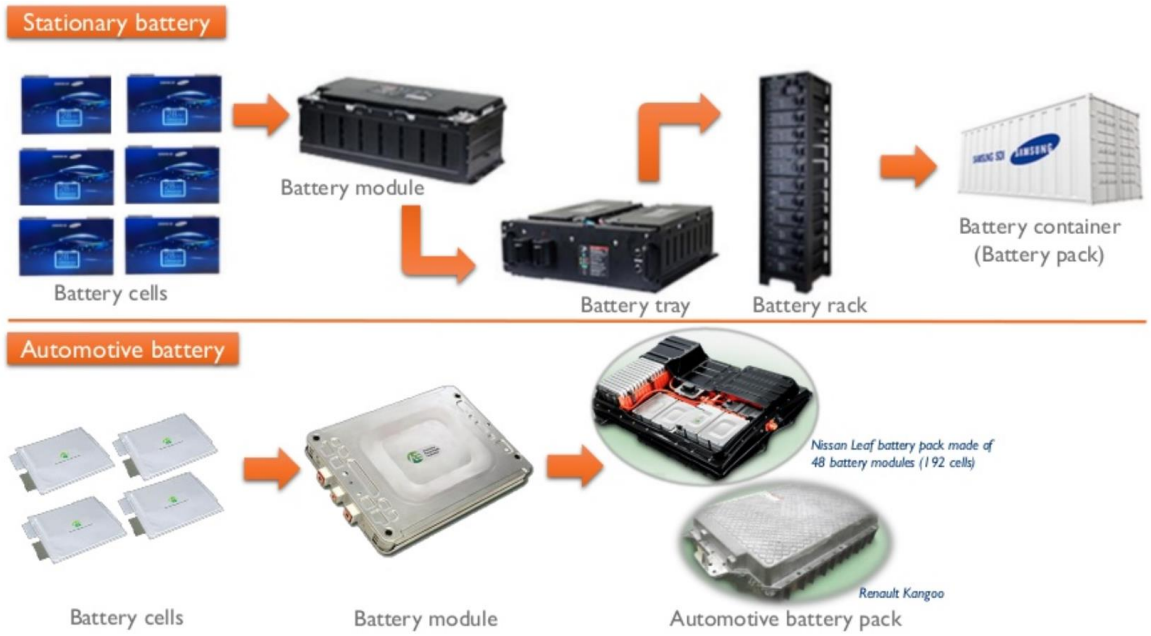

Figure 1-1: Composition of a battery pack for both stationary and automotive applications [6].

For automotive applications, individual batteries composed of sheets of anode, cathode and separator are referred to as battery cells. Combining multiple cells and enclosing these cells in a metal casing is referred to as a battery module. The connection of multiple battery modules together with a BMS and a thermal management unit is referred to as the battery pack. For stationary applications such as "smart grid", additional terms such as battery trays and battery racks can be used. These terms simply refer to the connection of multiple cells in series and parallel to generate a pack that can meet the excessive demands of the grid. The size of the pack for applications can differ, with automotive packs in the range of 20 – 75 kWh and packs for stationary applications in the range of 50 kWh to 1 Mwh.

1.1 Motivation

A large number of algorithms have been developed in literature for estimating SOC and SOH, with a number of different techniques being proposed using adaptive filter algorithms [7]–[11], learning algorithms [12]–[16], and non-linear observers [17]–[20]. These algorithms normally estimate SOC and SOH simultaneously, where battery model parameters are often used to determine battery degradation. Although such algorithms have been shown to accurately determine SOC and SOH at the cell level, problems can arise when they are extended to a battery pack.

Since no two individual batteries are the same, connecting multiple cells together will result in a battery pack with cell-to-cell variability. Inconsistency among cells could be a result of variations in the contact resistances, the amount of active material, and different temperature gradients within the pack. However, assuming no variability exists and applying the SOC/SOH algorithms to a pack can lead to erroneous results[21]. Alternately, applying these algorithms on each individual cell in the battery pack can be computationally expensive. Therefore, a significant amount of research is still required to develop an algorithm that can reliably estimate SOC and SOH at the pack level.

In addition, research is currently being carried out to build accurate battery models for battery simulation purposes as well as for hardware-in-the-loop (HIL) and software-in-the-loop (SIL) testing. These models can take a variety of different forms from multi-dimensional electro-chemical models [22]–[24], to numerous equivalent circuit models (ECM) [25]–[27]. A number of approaches have been proposed in improving the real-time simulation speed of these algorithms [28]–[30]. However not enough research has been carried out in reducing the time required to characterize these battery models. In addition, no research currently exists in simulating the effect of cell change out on a battery pack's SOH.

This thesis will shift focus away from a single cell and towards research at the pack level. It attempts to address the lack of research that currently exists in pack-level SOC and SOH estimation as well as battery pack simulation for BMS and battery manufacturers. The main objectives of this thesis are summarized in the section below.

1.2 Research Objectives

Upon development of an algorithm in simulation, there are numerous hurdles before the results can be implemented on a commercial product. Real-world scenarios must contend with additional noise, unexpected disturbances, inaccurate sampling rates, limited computational resources, and various other factors that could result in poor algorithm performance. Therefore, this thesis will focus on developing tools and algorithms that bridge the gap between academic research and product implementation.

The objectives of this thesis are two-fold:

1. First, this research will aim to develop modeling and simulation tools that will allow:
    - BMS manufactures to optimize SOC and SOH algorithms by conducting HIL and SIL testing and;
    - Battery manufacturers to design optimal battery packs for electric vehicle and other applications. The novelty of these algorithms will be on developing characterization protocols with minimal experimental time and on building simulators that can be used to assess the feasibility of cell replacement in a battery pack.
2. Second, this work will attempt to develop dynamic SOC and SOH models which can be implemented on an embedded system. The goal is to find algorithms that meet the accuracy requirements of a particular application but are still efficient enough for execution on a BMS. The algorithms should be able to accurately predict the SOC and SOH metrics for a large number of cells in a battery pack and should behave logically to the battery user. Logical behavior in this work is defined as smooth transitions in SOC, where the SOC increases only during charge, decreases only during discharge and remains constant at rest.

1.3 Thesis Outline

The chapters of the thesis are organized as follows:

- Chapter 2 provides fundamental background on batteries and BMS, cell level modeling, SOC estimation and SOH estimation. The goal is to give the reader a clear definition of these terms and provide a thorough description of the techniques currently applied in literature.
- Chapter 3 focuses on building a comprehensive battery model that can be used by BMS manufacturers for HIL and SIL testing. A new characterization approach is proposed that requires a minimal number of experimental runs and uses replication data to predict the significance of model parameters. The results are compared with currently existing techniques with regards to characterization time and prediction accuracy.
- Chapter 4 shifts towards estimating battery health with the intent of developing an algorithm that can be run for a large battery pack composed of hundreds of cells. A

carefully designed validation test is carried out and the results from the algorithm are compared to current existing techniques.

- Chapter 5 extends the resistance values obtained in the preceding chapter to generate a stable SOH metric. Issues relating to temperature and SOC dependence, outlier detection, outlier removal and noise filtering are explored. A validation test is included to demonstrate the performance of the algorithm.
- Chapter 6 discusses SOC estimation, once again at the pack level. A comprehensive algorithm is developed that accounts for variation in cell parameters under different operating conditions, cell-to-cell variability in the pack due to inefficient cell balancing and logical SOC fuel gauge behavior. Once again, a set of carefully designed validation tests are carried out to test the tracking performance of the algorithm.
- Chapter 7 shifts from algorithm development to simulation; a battery pack is modeled and the concept of cell change-out is explored. Two different battery chemistries are utilized and the results at different degradation rates are compared.
- Chapter 8 summarizes the main research contributions of this work as well as offers new directions for future research.

Chapter 2: Background and Literature Review

2.1 Battery and Battery Management System Background

2.1.1 Lithium Ion Batteries

Lithium-ion (Li-ion) batteries are electrochemical devices that provide electrical energy from stored chemical energy through the transport of lithium ions. The battery is composed of two electrodes, and a separator both of which are immersed in an electrolyte solution (Figure 2-1).

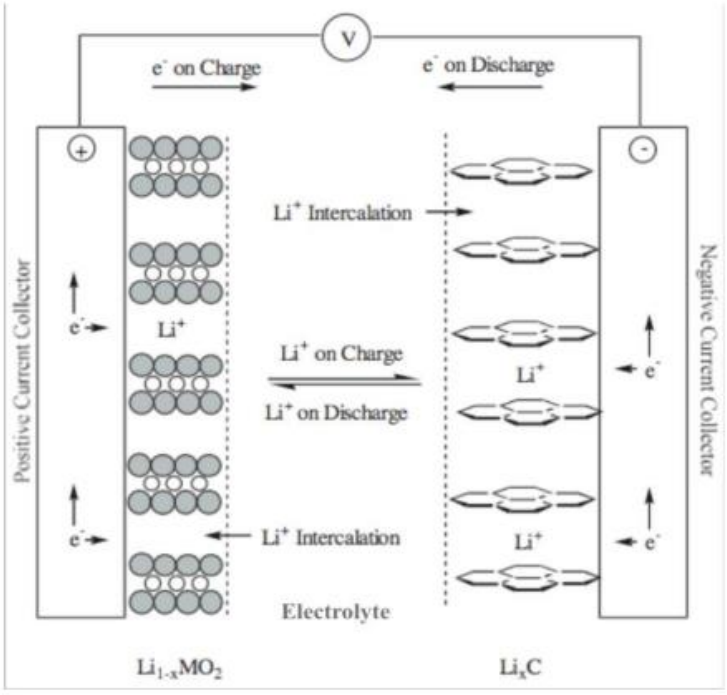

Figure 2-1: A schematic of L-Ion battery during charge and discharge [31].

The positive electrode, which is the cathode during discharge and anode during charge, is normally coated with a lithium metal oxide ($Li_{1-x}MO_2$). The negative electrode, which is the anode during discharge and is the cathode during charge, is composed of graphite. During discharge, the lithium ions deintercalate from the negative electrode giving off electrons as shown in the equation below:

$$Li_xC \rightarrow C + xLi^+ + xe^- \quad (2\text{-}1)$$

The ions from the negative electrode then move across the separator and intercalate into the metal oxide active material of the positive electrode:

$$Li_{1-x}MO_2 + xLi^+ + xe^- \rightarrow Li_xMO_2 \quad (2\text{-}2)$$

As shown in Figure 2-1, the electrons given off in the negative electrode travel across the load and are accepted by the positive electrode, completing the circuit. In the same way, during charge, the load is replaced by a power supply and energy is given to the system in order to move the lithium ions from the positive electrode to the negative electrode.

2.1.2 Battery Management System

The state-of-charge (SOC) represents the amount of useable charge remaining in the battery at any given time. When the battery is fully charged, the SOC is 100% and it is 0% when the battery is empty. It can be thought off as the ratio of the difference between the rated capacity and the discharged capacity to the rated capacity. The equation describing SOC is shown below:

$$SOC = \frac{Cap_{rated} - Cap_{discharged}}{Cap_{rated}} \quad (2\text{-}3)$$

where Cap_{rated} represents the rated capacity and $Cap_{discharged}$ represents the amount of charge that was discharged. Estimating the SOC in a battery is challenging since it cannot be measured directly from the cell; rather the SOC needs to be estimated from other measurements such as voltage, current or temperature. Therefore, the development of a robust closed-loop SOC estimator, requires significant attention and will be one of the goals of this thesis.

In addition to SOC, a reliable battery management system (BMS) must also evaluate the health of the battery. Similar to SOC, the battery state-of-health (SOH) is a percent, where 100% and 0% represents a fresh and fully aged battery respectively. Defining when a battery is fully aged can be dependent on two variables: capacity and resistance. Therefore, the BMS is responsible for estimating either the resistance or capacity of the battery and converting these estimates in a stable SOH metric. Algorithms for estimating SOH and SOC will be explored in greater detail in the sections below.

The term BMS refer to the hardware and software components required to control and monitor the charging and discharging of a battery pack in a safe and efficient manner. In addition, the BMS is responsible for cell balancing and thermal management [32]. In order to carry out these tasks,

the SOC and SOH of the battery must be continuously monitored. BMS are required in both electric and hybrid electric vehicle as well as in portable electronics (PE). The BMS is responsible for:

SOC update: The voltage, temperature and current are measured at a certain frequency for each cell in the battery pack. At each sampling interval, these measurements are used to update the SOC of the battery pack.

SOH update: The capacity of the cell as well as its internal resistance is subjected to change throughout the lifetime of the battery. The BMS is responsible for using the voltage and current measurements to estimate cell degradation and determine whether any of the cells need to be replaced.

Maximum available power: The SOC value obtained can be used to determine the maximum power that is available at a given time for charge or discharge, such that the voltage and other battery limits are not exceeded.

Equalization: An essential part of the BMS is to ensure that all the cells in the battery pack have the same SOC throughout the charge/discharge cycle. This is accomplished by individually adding charge to cells with low SOC and depleting charge from cells that have high SOC. For applications in hybrid electric vehicles (HEV), this equalization process must occur continuously as the battery pack is being used.

Safety: The number one responsibility of the BMS is to ensure the battery pack is operating within its safety limits. For this purpose, voltage and temperature readings are obtained at the cell level for a battery stack. If an individual cell goes above or below the voltage and temperature thresholds, the battery pack is disconnected from the circuit.

Fault detection: Detection of faults in the voltage, temperature and current sensors is essential for accurate SOC/SOH estimation as well as safe and reliable battery operation. Therefore, a BMS should be able to detect and isolate faults within the energy storage systems (ESS). These faults could be a result of a loose voltage sense wire, or an eroded bus-bar.

2.2 Battery Modeling

Developing SOC and SOH algorithms often require an accurate battery model. These models are generally divided into three different categories: 1) equivalent circuit models (ECM) 2) behavioral models and 3) electrochemical models. When considering these models, it is important to determine how much fidelity is required for the given task and if there are any computational limitations. ECM do not require much computational effect; however, they are not always able to adequately capture the non-linear dynamics of the battery. In addition, the estimated parameters might not have any physical meaning. Electrochemical models, on the other hand, can provide a higher degree of accuracy and estimation of model parameters provide insights into the dynamics of the battery. These models, however, often require solving ordinary or partial differential equations (PDE), which can be problematic in an embedded system with limited processing capabilities. Therefore, there is no "best" model that should always be used; rather, a thorough analysis must be carried out to determine the simplest model that can be developed while still meeting the accuracy requirements of a specific application.

2.2.1 Equivalent Circuit Models (ECM)

ECM are empirical models that replace the electrochemical phenomena found in batteries with electrical components. The simplest ECM, known as the *Rint* model, simply has a resistance in series with the open circuit voltage (OCV) [33]. The terminal battery voltage, given as $U_{L,k}$, is dependent on the current, represented by $I_{L,k}$, as shown below:

$$U_{L,k} = U_{ocv,k}(SOC_k) - R_0 I_{L,k} \tag{2-4}$$

where $U_{ocv,k}$ is the OCV and R_o is the ohmic resistor. The value of the current is positive during discharge and negative during charge. The OCV of the battery represents the battery potential when no current is flowing. It should be noted that the value of R_0 is not constant but rather is a function of battery SOC and temperature. A number of approaches in literature focus on estimating this term using computationally expensive techniques such as extended Kalman filter (EKF) and the recursive least squares (RLS) [34], [35]. One of the main contributions of this thesis will be accurately estimating the ohmic resistance value while minimizing computational cost.

Although this model is relatively simple and easy to implement, it is not able to capture the dynamic behavior of the battery as the concentration and activation polarization within the battery

cannot be modeled. To resolve this issue, models based on a pair of resistance-capacitors (RC) have also been proposed in literature. The two most commonly used models are the Thevenin model and the dual polarization model [36]–[38] and these models are shown in Figure 2-2 and Figure 2-3.

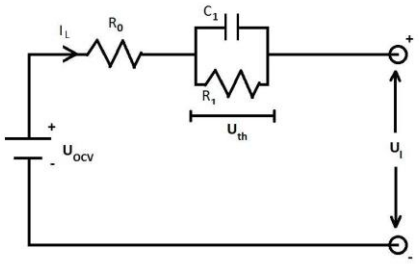

Figure 2-2: The equivalent circuit diagram for the Thevenin Model.

The model consists of the OCV represented by U_{ocv}, one resistor R_o and one RC pair in parallel. The initial resistance is used to capture the ohmic resistance of the electrolyte, the cathode and anode, while the RC pair represents the electrochemical polarization effect of the battery. The ECM can be written in the form of a differential equation as shown below.

$$\frac{D(U_{th})}{dt} = -\frac{U_{th}}{R_1 C_1} + \frac{I_L}{C_1} \tag{2-5}$$

$$U_L = U_{ocv} - U_{th} - I_L R_o \tag{2-6}$$

where R_1 is the Thevenin resistor, C_1 is the Thevenin capacitor and U_{th} is the voltage drop across the RC pair.

In addition to the electrochemical polarization, concentration polarization is often present in the battery. To model this effect, another *RC* pair is often added to the Thevenin model. This model is therefore able to capture the electrochemical and concentration polarization and the diagram is shown below.

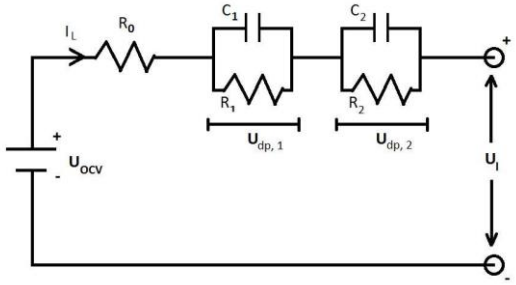

Figure 2-3: The equivalent circuit diagram for the Dual Polarization Model.

The battery model can once again be expressed using the following three equations.

$$\frac{D(U_{DP1})}{dt} = -\frac{U_{DP1}}{R_1 C_1} + \frac{I_L}{C_1} \tag{2-7}$$

$$\frac{D(U_{DP2})}{dt} = -\frac{U_{DP2}}{R_2 C_2} + \frac{I_L}{C_2} \tag{2-8}$$

$$U_L = U_{ocv} - U_{DP1} - U_{DP2} - I_L R_o \tag{2-9}$$

If the above models do not meet the accuracy requirements of a particular application, additional *RC* pairs can be added. These additional *RC* pairs do not represent physical elements within the battery, but rather are utilized for improving the model predictive capability. It should be noted that the *RC* elements in the ECM can be obtained by fitting the model with experimental data. Therefore, the developed model is only valid for the operating conditions during which the parameters were estimated. This means that simulating the voltage dynamics of the battery under a different operating temperature can yield inaccurate results.

2.2.2 Electrochemical Models

Electrochemical models are fundamental battery models that attempt to describe the chemical processes that can occur within the battery. These models are governed by a set of equations that relate their electrical and physical properties together. In many cases, the model consists of a set of PDEs that need to be solved simultaneously. Therefore, although a complex model can provide a higher degree of accuracy, it will also incur a higher computational cost. In addition, the physical parameters of the model are subjected to change due to aging of the battery over time. The first

electro-chemical modeling approach to porous electrodes was introduced by Newman and Tiedemann in 1975 [39], where the electrode was modeled as a group of microscopic spherical particles. It should be noted that the proposed research will only consider ECM and behavioral models due to computational limitations.

2.2.3 Behavioral Models

Behavioral models describe the battery dynamics by using empirical equations and are often utilized when computational cost is an issue. The empirical equations are often carefully selected to mimic the voltage or temperature response of the battery under operation. Similar to ECM, behavioral models require experimental data for obtaining the model parameters.

Three different behavioral models were proposed by Plett. 2004 [40]. First, a zero-state hysteresis model has been developed to take into account the hysteresis effect, which is often present in Li-ion batteries. It is a characteristic of a battery system, where the battery voltage profile changes depending on the current direction. To resolve this issue, Plett added a constant parameter to the *Rint* model, that takes into account the battery hysteresis. The zero-state hysteresis model is shown below:

$$U_{L,k} = U_{ocv}(SOC_k) - s_k M(SOC_k) - R_0 I_{L,k} \tag{2-10}$$

$$s_k = \begin{matrix} 1 & I_{L,k} > \varepsilon \\ -1 & I_{L,k} < -\varepsilon \\ s_{k-1} & |I_{L,k}| \leq \varepsilon \end{matrix} \tag{2-11}$$

where the variable s_k is used to represent the sign of the current, and ε is small, positive number. The term $M(SOC_k)$ is used to quantify the cell hysteresis and is calculated by taking the difference between the charge and discharge curve, dividing this value by two and subtracting the internal resistance $R_o I_{L,k}$ loss.

Although the above model is simple to implement, it is not able to adequately capture all the hysteresis effect since the battery hysteresis voltage is a function of battery SOC. Therefore, to account for this issue, Plett proposed estimating the voltage hysteresis as an additional battery state in the model.

$$\frac{dh(SOC,t)}{dz} = \gamma\, sgn\left(S\dot{O}C\right)\left[M\left(SOC,S\dot{O}C\right) - h_{hys}(SOC,t)\right] \tag{2-12}$$

Where $M\left(SOC,S\dot{O}C\right)$ is the maximum polarization due to hysteresis, $sgn\left(S\dot{O}C\right)$ is used to differentiate between charging and discharging and γ is used to describe the decay of the hysteresis voltage. The above model can be written in discrete state-space form and is shown below.

$$\begin{bmatrix} h_{hys,k+1} \\ SOC_{k+1} \end{bmatrix} = \begin{bmatrix} F(I_{L,k}) & 0 \\ 0 & 1 \end{bmatrix} \begin{bmatrix} h_{hys,k} \\ SOC_k \end{bmatrix} + \begin{bmatrix} 0 & 1 - F(I_{L,k}) \\ \frac{\eta \Delta t}{C_n} & 0 \end{bmatrix} \begin{bmatrix} I_{L,k} \\ M\left(SOC,S\dot{O}C\right) \end{bmatrix} \tag{2-13}$$

$$F\left(I_{L,k}\right) = \exp\left(\frac{\eta I_{L,k}\gamma}{C_n}\right) \tag{2-14}$$

By solving the state space equation, the SOC and voltage hysteresis states can be obtained at each time step. The terminal voltage can then be updated using the above equations. Once again, the parameters of these models can be obtained by conducting a well-designed identification experiment.

2.3 State-of-Health

Over the lifetime of the battery, its capacity is known to slowly decrease while the battery's internal resistance is found to increase, resulting in a reduction in the battery's power capability [41]–[43]. This degradation can occur as a result of the battery being cycled multiple times or simply due to storage. Although degradation can occur at both the positive and negative electrode of the battery, majority of the degradation occurs at the negative electrode. This section will provide a brief overview of some of the major sources of degradation that occurs at the negative electrode.

The most significant source of battery degradation comes from side reactions at the electrode/electrolyte interface, which forms a solid electrolyte interface (SEI) film [41], [44], [45]. The formation of the SEI layer is rapid during the first few cycles and then proceeds to grow slowly for the remainder of the battery life. This layer is essential for battery safety since it slows down the intercalation kinetics at the electrode/electrolyte interface [46]. However, the layer consumes lithium ions resulting in a loss of cyclable lithium and thus causing capacity fade. On the other hand, as the SEI layer grows, it inhibits the transport of lithium ions resulting in an increased

charge transfer resistance within the cell [41], [43], [47]. The rate of SEI formation is dependent on the operating conditions, where cycling the cell at high temperatures can accelerate the degradation process, thereby driving the exothermic parasitic reaction responsible for SEI growth.

In addition to the formation of the SEI layer, degradation in the battery can also result from lithium plating, where lithium metal is deposited onto the active material in the negative electrode. Deposition can occur if there is a high concentration of lithium ions and the potential at the negative electrode is low enough to incur deposition [44]. Operating conditions such as low temperatures, high current rates and over charging can lead to lithium plating [47]. Lithium plating consumes a significant amount of lithium ions thereby reducing the capacity of the battery. Finally, physical changes in the negative electrode can also lead to battery degradation. For example, loss of contact between the separator, graphite, binder and current collector can result in an increase in cell impedance [44]. Structural changes can also occur at the graphite electrode resulting in both capacity fade and power fade. The following section will examine the estimation of each of these two quantities in greater detail.

2.3.1 Capacity Estimation

To understand the capacity estimation procedure, consider two batteries of the same type but one with a higher capacity. If both batteries are charged or discharged for a certain number of ampere-hours, the voltage change will be higher for the battery with the lower capacity. Therefore, capacity can be estimated based on the relationship between the ampere-hours charged/discharged and the voltage difference before and after this process. Majority of the capacity estimation methods are based on this principle and they can be divided further into four different groups. The following section will explore these different methods and discuss the advantage and disadvantage of each.

The first group of methods involves determining the change in the OCV before and after charge/discharge. It is based on the OCV-SOC relationship that is specific to the battery chemistry [48], [49]. The advantage of this method is that the OCV-SOC relationship does not significantly vary over the lifetime of the battery. However, the proposed technique requires finding the resting potential at different SOC intervals, something that is difficult to accomplish if the commercial application contains no rest periods in between. The second group of methods operate on similar

principles except, instead of measuring the OCV, these technique uses the terminal voltage to estimate the voltage [50], [51]. The OCV is determined using a battery model, which in most cases is an ECM. Although this approach is advantageous for use in an electric vehicle (EV), where OCV measurements are difficult to obtain, its accuracy is limited by the battery model. In addition, the battery model is also subjected to aging and therefore, must be able to accurately adapt to the degradation process.

The other two methods of capacity estimation are based on using an electrical model, where capacity and SOC are parameters that need to be estimated. The first technique is called joint estimation and it involves simultaneously estimating SOC and capacity using an adaptive technique. Techniques such as the EKF [52], [53], unscented Kalman filter (UKF) [54] and the RLS algorithm [55], [56] have been utilized for this purpose. The main disadvantage with these techniques is that it involves carrying out large matrix calculations. To resolve this issue, the dual EKF has been proposed, where two filters are utilized instead of one. This approach is a significant improvement with regards to computational time, since the parameters (including capacity) can be estimated using one adaptive filter and the state variables, such as SOC, can be updated using another filter. Adaptive techniques such as dual EKF [57]–[59] and the dual sigma point Kalman filter (SPKF) [56] have been used for this purpose.

2.3.2 Resistance Estimation

Power fade is a term used to represent the decrease in the amount of power that a battery can provide for a specific application. The value can be used in conjunction with capacity fade to provide an overall estimate of the battery SOH, as shown in the equation below.

$$SOH = min\left(SOH_{Cap}, SOH_{Res}\right) \tag{2-15}$$

where SOH_{cap} represents the health based on capacity fade and SOH_{res} represents the health based on power fade. Capacity fade is significant for vehicle applications since it determines the range of the EV or PHEV. Power fade on the other hand is essential for stationary applications, where the battery needs to meet the power demands of the energy grid. For the purposes of this thesis, online estimation of capacity fade at the cell level will be carried out using the technique proposed by Einhorn et al. [60]. The approach determines the capacity based on two SOC points and by using the charge transferred between these two points. However, more research is still required in

accurately quantifying power fade at the cell level. Therefore, the main focus of this work will be on estimating resistance for each individual battery within the pack.

The resistance estimation techniques proposed in literature generally fall into one of two groups. In the first group, the authors used impedance spectroscopy in order to find the battery resistance [63], [64]. There is an additional cost associated with this technique since it requires using special circuits for active signal generation. Other authors have proposed passive impendence spectroscopy methods where current fluctuations from the batteries normal operation are used as the excitation signals [65]. This approach cannot always be applied since periodic current fluctuations at a certain frequency range must be always present.

Majority of the work in this field has been carried out in the second group of methods, which involve using electrical models. Battery resistance is a parameter in these models and is estimated using the voltage and current measurements. The most commonly used estimation technique is the Kalman filter, where battery resistance is estimated online. Other techniques for determining resistance include a linear adaptive filter [66], a sliding mode observer (SMO) [67] and an observer based on the Lyapunov-stability criteria [68]. Implementation of these techniques on an embedded platform can be problematic due to the computational cost of these algorithms. Therefore, development of algorithms that provide accurate resistance estimates, while requiring a smaller amount of computational resources, will be an important contribution of this research.

2.4 State-of-Charge

A variety of techniques have been proposed in literature in the area of SOC estimation and this section will provide a brief overview of these methods. For a more in-depth analysis of SOC estimation techniques, refer to the following review papers [69]–[72].

2.4.1 Conventional Algorithms

One of the simplest SOC estimation methods is based on the notion that one can count the coulombs entering and leaving the battery. The equation for calculating the SOC is

$$SOC = SOC_0 - \frac{1}{C_n} \int \frac{I_L}{3600}\, dt \qquad (2\text{-}16)$$

where I_L is the current measured in coulombs/second, and C_n is the maximum battery capacity. There are however, two major limitations with this method. First, the method requires knowledge of the initial SOC and maximum capacity, which, in many instances, might be unknown [30]. Second, depending on the precision of the current shunt that is used, the current measurements might contain a high degree of noise. This can lead to a gradual drift in the actual current measurements, which will result in a larger and larger SOC error over time.

SOC estimation can also be carried out using knowledge of the battery's OCV since there is a predictable relationship between this value and the SOC [31]. The method involves utilizing an ECM to estimate the OCV and inferring the SOC based on the OCV value. One of the simplest models in determining the OCV assumes only a resistance R_0 and is shown below:

$$U_{L,k} = U_{ocv}(SOC_k) - R_0 I_{L,k} \tag{2-17}$$

where $U_{L,k}$ is the measurement voltage at each time step. Although the method is easy to implement, it can be problematic for lithium iron phosphate (LFP) cells since they have an OCV curve that is relatively flat.

2.4.2 Adaptive Filter Algorithms

Most adaptive filtering algorithm in this area contain the following key steps. The battery is first modeled using an empirical or electrochemical model, where the terminal voltage of the battery is predicted. This voltage, which is dependent on the battery states, is then compared with the measured value and the states are updated based on the new measurement. In addition, these algorithms account for both process and measurement noise and can use this uncertainty in determining optimal state estimates. One significant advantage of using adaptive filtering methods is that not only does it provide optimal estimate of the states, it can also be used to correctly quantify the degree of uncertainty in the estimates [33], [73], [74].

The most commonly used filtering approach is the EKF. The EKF is an extension of the Kalman filter approach, where a first order Taylor series expansion is carried out to linearize a non-linear model. Plett in 2006 [73] introduced the EKF for estimating SOC in Li-ion batteries. Since then a number of approaches have expanded on this work to account for temperature variations, cell degradation, measurement noise and other disturbances [57], [75]–[77]. Mehrdad et al. [78]

applied the dual EKF to provide new insights into the battery dynamics for cells with different geometries. Xiong et al. [76] proposed an EKF algorithm, where model parameters were updated based on a larger time scale than SOC estimates. And Sepasi et al. [75] applied a fuzzy method for estimating the initial SOC and used this value in the EKF algorithm.

Although the EKF provides reliable results, it does require an appropriate initial guess for the process and measurement covariance matrix. The covariance elements are also assumed to be constant through the process. In order to account for changes in process and measurement covariance matrices as the cell is cycled, an adaptive extended Kalman filter (AEKF) is often applied [77], [79], [80]. Although the algorithm is shown to be able to improve the SOC estimation error to below 3%, it can be computationally expensive since the covariance matrices need to be updated on each iteration [77]. Building on this work, a variety of different filters have been proposed for SOC estimation including UKF [81]–[83], SPKF [59], [84], and particle filter (PF) [7], [85], [86].

2.4.3 Learning Algorithm

While adaptive filters and non-linear observers require internal knowledge of the battery dynamics, learning algorithms such as artificial neural networks (ANN) have the ability to learn based on a large amount of training data. This gives them a significant advantage since prior knowledge of the battery intricacies is not required. However, they are normally trained based on a large data set, which can be problematic in a BMS with limited storage space.

Neural networks models consist of three layers: the input layer, one of more hidden layers, and an output layer. For applications in batteries, the inputs are usually composed of the terminal voltage, applied current and temperature. The inputs are passed into the hidden layer, and the output is calculated based on a non-linear function of the sum of the inputs. The weights for each factor is determined using the large data set. The output for Li-ion batteries is normally the battery SOC. Figure 2-4 provides a schematic of the different layers with neural networks.

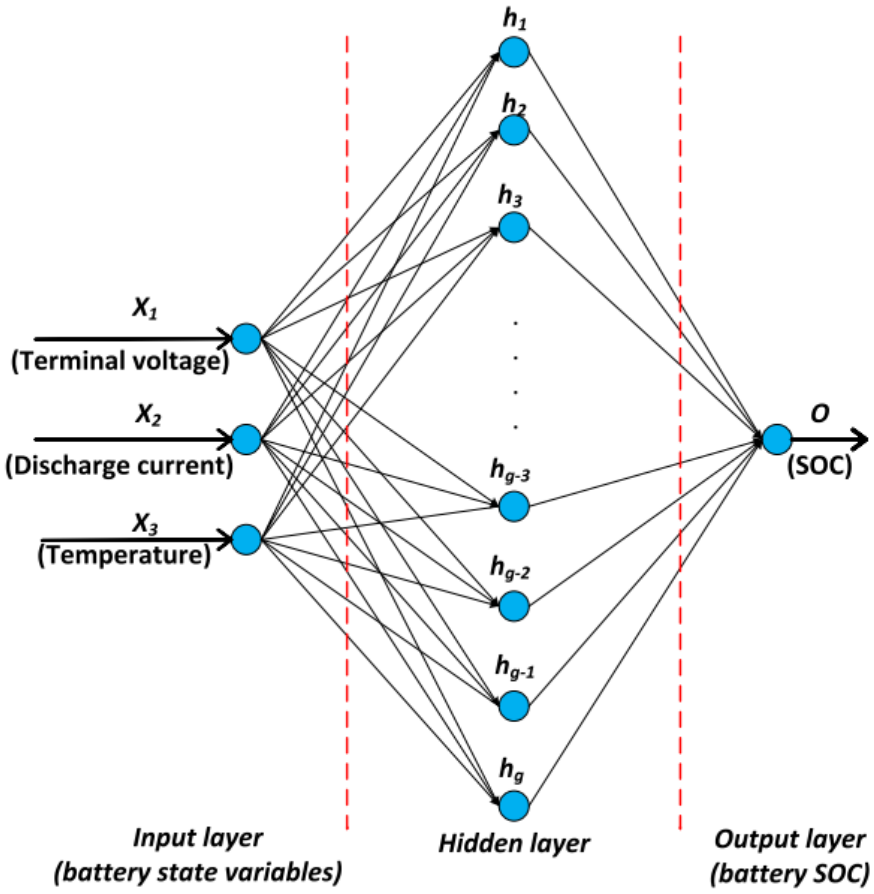

Figure 2-4: Structure of neural network models with input, hidden and output layer.

A number of neural network approaches have been proposed in literature for estimating the battery SOC. Chaoui et al. [14] proposed using dynamically driven recurrent neural networks to simultaneously estimate the SOC and SOH of the battery. The work has been extended to input time-delayed neural networks (ITDNN) by Chaoui et al. [15], where once again both SOC and SOH are estimated. The model has been shown to account for non-linearity within the system, including hysteresis effects and battery degradation. Chenghui et al., [87] used ANN for SOC determination, where the battery discharging current, accumulated ampere hours, battery terminal *V*, time-average terminal voltage and twice time-average voltage were used as inputs and the SOC was used as an output.

In addition, neural networks can often be coupled to adaptive techniques in order to improve their predictive capabilities. He et al. [88] incorporated unscented Kalman filter in the overall algorithm to reduce the errors in the neural network. The work by Chen et al. [89] integrated radical

basis function (RBF) neural network to adaptively estimate the upper bound on the system uncertainty. The value is then used in a robust sliding-mode observer in order to determine the SOC.

Another type of learning algorithm that is frequently used for SOC estimation is fuzzy logic. Once again this is a powerful tool for SOC estimation when a large data-set is available and enough computational power is accessible. The estimates are determined by incorporating a certain degree of uncertainty when dealing with noisy data. Burgos et al. [13] developed a new fuzzy model for modeling the discharge behavior of lead-acid (LA) batteries. An EKF approach is then used based on this fuzzy model for SOC estimation. And finally, Awadallah et al. [90] proposed an adaptive neuro-fuzzy inference systems (ANFIS) technique for considering the nonlinear characteristics of the battery at different operating conditions. The approach is combined with coulomb counting for determining the SOC with a high degree of accuracy.

Chapter 3: Comprehensive Cell Model for Lithium-Ion Battery Pack Simulation

The following chapter is based on the two submitted works: The first by M. Mathew, M. Mastali, J. Catton, E. Samadani, and M. Fowler published by the *Society of Automotive Engineers* (SAE) entitled: **"Efficient Electro-Thermal Model for Lithium Iron Phosphate Batteries"** and the second by M. Mathew, M. Mastali, J. Catton, E. Samadani, S. Janhunen, and M. Fowler submitted to *Batteries* entitled: "**Development of an Electro-Thermal Model for Electric Vehicles Using a Design of Experiments Approach"**

The author's specific contribution was in developing the comprehensive cell model, conducting thermal experiments, carrying out the simulations, preparing the results, graphs and manuscript. M. Mastali, J. Catton, E. Samadani, S. Janhunen and M. Fowler offered advice and guidance, while M. Mastali, J. Catton, E. Samadani offered additional assistance with the experimental set-up and provided advise throughout the research.

3.1 Introduction

Although popularity of electrified vehicles has increased significantly in the last few years, research is still required in improving the durability, performance and service life of lithium-ion (Li-ion) batteries. In addition, safe and reliable control of large battery packs demands a battery management system (BMS) that can accurately predict battery state-of-charge (SOC) and state-of-health (SOH). Improving algorithms on a BMS can be time-consuming, especially if new experiments need to be conducted on each model iteration. In many instances, experimental resources are not available for testing BMS products under various conditions. Therefore, the ability to carry out hardware-in-the-loop (HIL) and software-in-the-loop testing (SIL) is essential.

Development of a HIL and SIL framework requires a high-fidelity and computationally efficient battery model. These models can take a variety of different forms from multi-dimensional electro-chemical models to equivalent circuit models (ECM). Electro-chemical models attempt to describe the battery dynamics at the fundamental level using mass and energy balance equations [28], [91]–[94]. Electrochemical models can be extended to include thermal effects, where the batteries' thermal response is coupled with its electrochemical behavior [23], [95]. These models

are governed by a set of ordinary differential equations (ODEs) or partial differential equations (PDEs) and solutions to these systems often require numerical solutions. Therefore, computational time can be a challenge, especially when applied to a battery pack composed of hundreds of cells.

In applications where computational time is an important factor, ECM have been proposed [96], [97]. The voltage response under load is captured using a resistor and *n* number of resistor-capacitor (RC) pairs in series. The value of *n* is dependant on the application; a larger number of RC pairs will yield a more accurate prediction of the terminal voltage. In addition, the low computational cost of the model is advantageous since it allows for simulation of a realistic battery pack with cell-to-cell variability [98]. It should be noted that the ECM parameters change with temperature, SOC and SOH [99], [100]. Therefore, a comprehensive battery simulator should account for these variations when modeling battery dynamics.

The changes in voltage response at different operating temperatures can be adequately captured using coupled electro-thermal models. The temperature dependence on parameters has been modeled by Hue et al. [101] using linear spline functions. Lin et al. [102] applied lumped parameter models to cylindrical batteries, where the temperature at the core was predicted. Samadani et al. [103] developed an empirical model for heat generation for application in electric vehicles. Research by Damay et al. [25] explored the extension of these electro-thermal models to include an entropic heat generation term. Low temperature modeling of these batteries has also been carried out by Jaguemont et al. [104].

All of the models described above require a response surface for describing how the ECM parameters change as a function of temperature and SOC. A look-up table (LUT) or polynomial fit is normally used in developing this surface. However, these approaches require conducting a large number of experiments to fully characterize the surface. In addition, statistical analysis of these models is essential in providing valuable insights into the dynamics of the battery. In light of these gaps in literature, the focus of this paper is to develop a response surface for the ECM parameters using a design of experiments (DOE) approach. Although DOE approaches have been used for SOC estimation by Liu et al. [105] and for predicted heat generation by Ehsan et al. [106], no work currently exists in using this technique for characterizing the ECM parameter model. In addition, statistical analysis is carried out to develop a robust model; the model can help the user better understand the battery dynamics at different operating conditions. Production and

commercialization of BMS often entails developing an accurate battery model that can be used for HIL and SIL testing. However, investing in model characterization can be expensive since a large number of experiments usually have to be carried out. The goal of this work is to provide future researchers with the tools to quickly develop fast and efficient models, that can in turn be used for improving BMS algorithms.

3.2 Experimental Procedure

3.2.1 Thermal and Voltage Experiments

All experiments are carried out on a lithium iron phosphate (LFP) battery from A123 systems. The battery specifications are shown in Table 3-1 below.

Table 3-1: LFP pouch cell specifications

Parameter	A123 Battery
Cathode Material	$LiFePO_4$
Anode Material	Graphite
Dimension (mm)	7.25 x 160 x 227
Mass (g)	496
Rated Capacity (Ah)	20
Nominal Voltage (V)	3.3

The battery was charged and discharged for a given current profile using Bitrode FTV:300/50-20 unit. The cell cycler has an upper voltage limit of 20 V and maximum current limit of 300 A. The voltage and current measurements were sampled at a frequency of 1Hz using the VisualLCN software. The ambient temperature of the battery was maintained at a constant value using the Cincinnati Sub-Zero Micro Climate unit. The temperature measurements were recorded using the National Instruments (NI) 8-channel thermocouple module and once again, the sampling time was taken to be one second. The experimental set-up is shown in Figure 3-1 below.

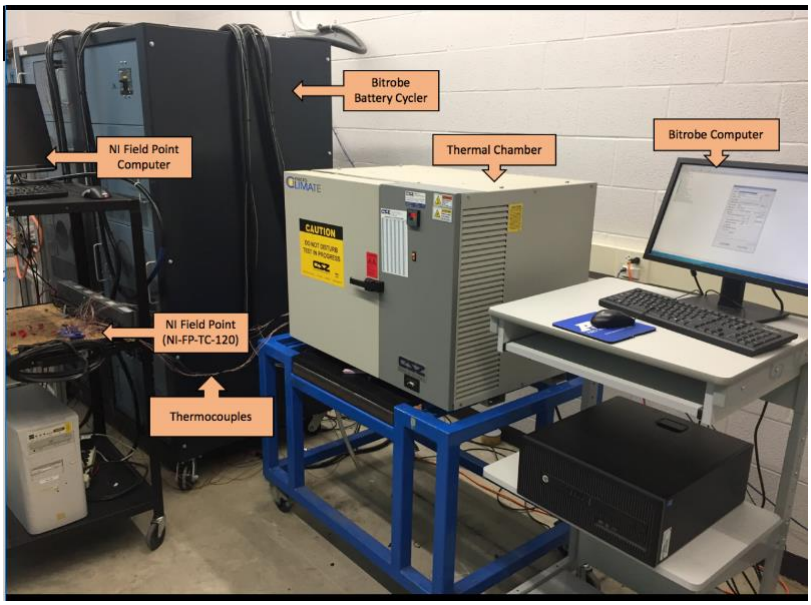

Figure 3-1: Experimental set-up for model development and voltage validation.

T-type thermocouples were placed on the surface of the battery to measure the surface temperatures at seven discrete points. It is also observed that the temperature gradient across the thickness of the cell is negligible; this finding has been shown to be true by Mastali et al. [107] for an LFP pouch cell. The thermocouple locations are shown in Figure 3-2. All thermocouples were connected to NI temperature measurement device, which is further connected to the computer using ethernet. An average of the seven thermocouple readings, shown in Figure 3-2, will be used as the experimental temperature value. Since the battery temperature is slightly higher close to the tabs, three thermocouples are located at the top portion of the cell, while the rest are distributed across the battery surface to provide a reasonable average battery temperature.

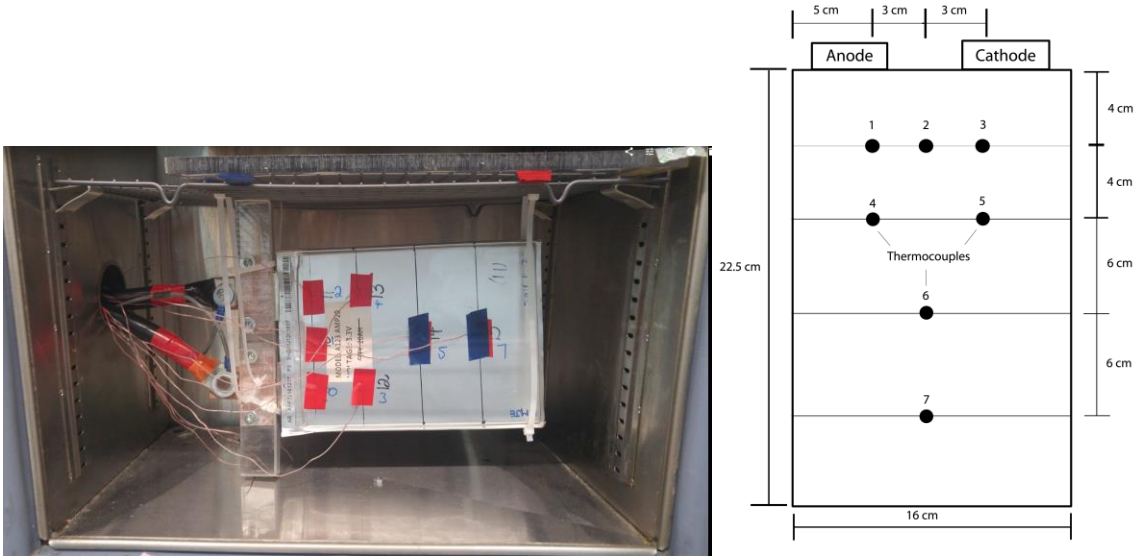

Figure 3-2: Thermocouple placement on the LFP cell inside the thermal chamber (left) and thermocouple placement measurements (right).

3.2.2 Open Circuit Voltage Characterization

In addition to the ECM parameters, the voltage response model requires knowledge of the battery's open circuit voltage (OCV). The OCV which is a function of the SOC of the battery, represents the battery potential when there is no current flowing. Estimation of the OCV at different SOC points is essential for developing the voltage response model.

The open circuit voltage was developed using the following testing protocol:

1. The cell was charged to full using a constant current of 1C and maintained at a constant voltage of 3.65 V until the current drops to C/25. This will be referred to as constant-current constant voltage (CCCV) protocol.
2. The battery was allowed to rest for one hour
3. The battery was then discharged to empty using a current of C/25
4. After another one hour of rest, the battery was charged to full using a C/25 current.

By averaging the charge and discharge curves, the U_{ocv} curve can be obtained.

3.2.3 Entropic Heat Generation Characterization

To complete the dU_{ocv}/dT curve for the cell at various SOCs, the following procedure was utilized:

1. The cell was first charged to full using a CCCV protocol
2. The cell was then rested for approximately 12 hours with the thermal chamber set to a constant temperature of 25°C. The long rest allows the battery voltage to reach its true U_{ocv} value.
3. The temperature of the chamber was changed to 5°C. The cell was rested for an additional three hours in order to provide the battery enough time to reach the ambient temperature.
4. The chamber was then increased by 10°C every three hours, with the process for recording the U_{ocv} being repeated for each temperature increase, until the temperature of the chamber reached 45°C.
5. To test the next SOC point, the chamber temperature is changed back to 25°C and the cell is discharged for 10% SOC at 1C rate; The above procedure is then repeated.

The diagram below shows the temperature profile that was applied at each SOC. A 1C discharge was carried out at the end of the temperature profile to bring the cell to a new SOC value.

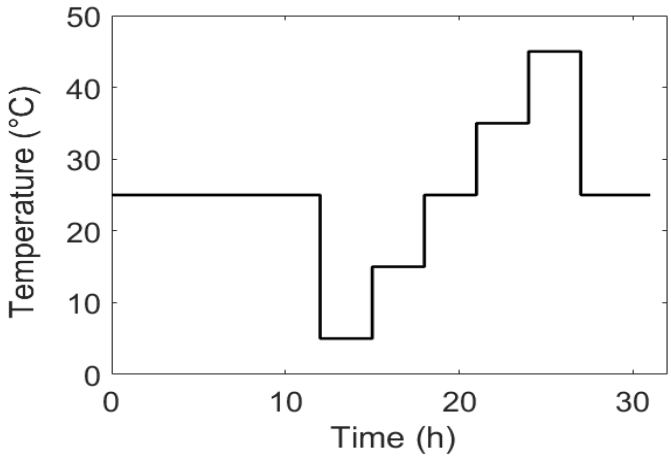

Figure 3-3: The temperature profile used for determining dU_{ocv}/dT term.

The value of U_{ocv} at a particular temperature is determined by averaging the terminal voltage of the battery in the last 30 minutes of rest.

3.2.4 Heat Transfer Coefficient Estimation

Estimating the heat transfer for the battery environment is an important part of developing a thermal model. The value of the heat transfer co-efficient can be determined by bringing the cell to a higher temperature, usually by charging or discharging the cell, and monitoring the decrease

in temperature when no current is supplied. These temperature curves are often referred to as cooling curves.

The cooling curves can be generated using the following protocol:

1. Charge the battery to full using CCCV protocol
2. Discharge until the voltage limit of 2.0 V is reached
3. Rest the battery for 1 hour, allowing the temperature to reach ambient. Record the temperature at a frequency of 1Hz
4. Repeat the above procedure at different C-rates.

The cooling curves that are generated can be utilized for determining the heat transfer coefficient for the experimental setup.

3.2.5 ECM Parameter Estimation

The resistance characteristics of the cell changes with temperature, SOH and SOC. Incorporating SOH is beyond the scope of this paper and therefore, will not be discussed here. However, the effect of SOC and temperature on the battery ECM parameters was determined using the hybrid pulse power characterization (HPPC) test described in [108]. The test consists of a 10 second discharge at 1C, a 40 second rest period and 10 second charge at ¾ C. It is summarized in Figure 3-4 below.

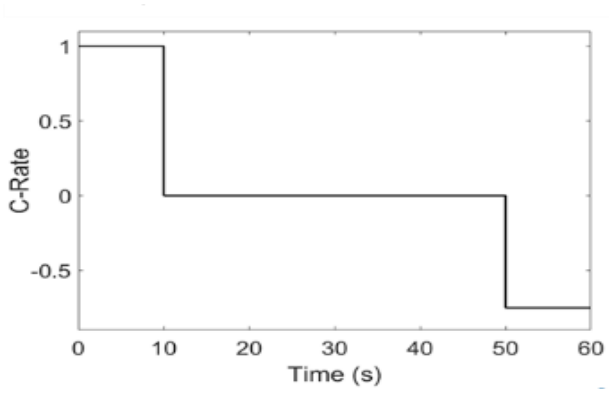

Figure 3-4: The HPPC test used for determining the battery ECM parameters.

The ECM parameters change with SOC and temperature; therefore, to identify these parameters, the HPPC test needs to be carried out at different temperature and SOC values. Since discharging to a new SOC point or temperature value requires an hour or two of rest,

characterization of these models can be time consuming. To resolve this issue, a design of experiments approach will be proposed in the next section, where HPPC runs will be carried out at select temperature and SOC points.

3.3 Algorithm Development

Development of a complete battery model requires four sub-models that need to be coupled together. These models include a heat generation model, a thermal model, a battery parameter model and a voltage response model. The diagram below shows the inputs and outputs of each of these models and how they are coupled with each other.

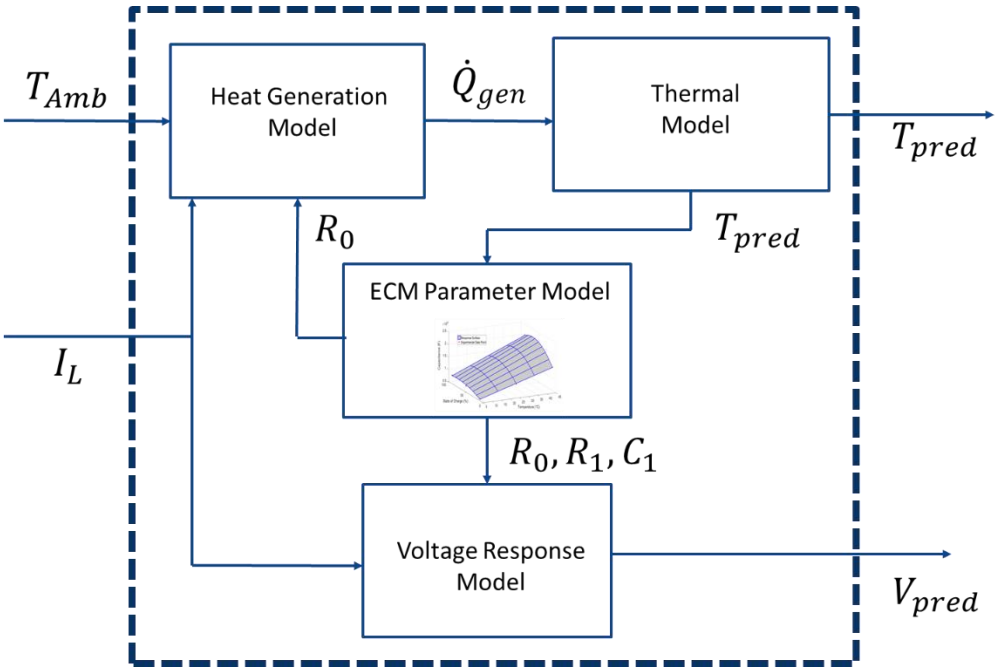

Figure 3-5: Overall comprehensive battery simulator with all four sub-models.

The full battery model takes inputs of ambient temperature and applied current and predicts the battery voltage and cell temperature. Simulation of battery voltage is essential for testing SOC or SOH algorithms on the BMS, while prediction of the cell temperature allows for better design of thermal pack management. Therefore, this paper will describe how each of these models can be developed and integrated together to build a battery simulator. Since the main contribution of this work is in the ECM parameter sub-model, this particular sub-model will be explored in greater detail.

3.3.1 Voltage Response Sub-Model

As previously mentioned, modeling of the battery's voltage response is often carried out using an ECM. An example of the model is shown in the diagram below.

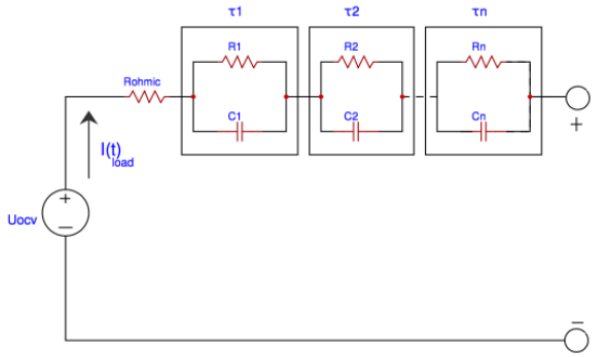

Figure 3-6: ECM with an OCV source, an ohmic resistance with n RC pairs in series.

There are three main components in the ECM: the OCV (U_{ocv}), a resistor and *n* number of resistor-capacitor pairs. The OCV represents the battery's thermodynamic potential at rest. It is based on the SOC of the battery. The battery SOC can be determined using the coulomb counting approach shown in Equation (3-1)

$$SOC = SOC_0 - \frac{1}{C_n}\int \frac{I}{3600}\,dt \tag{3-1}$$

The single resistor component is used to represent the battery's ohmic losses. This resistance is the sum of ohmic losses experienced at both electrodes as well as at the electrolyte. However, the battery also contains a time-dependent voltage loss due to polarization effects. This is usually modeled using a resistor-capacitor pair in series with the other components. The RC pair with the smaller time constant usually represents the activation polarization while the RC pair with the larger time constant presents the concentration polarization. Using additional RC pairs can improve the accuracy of the model at the expense of computational cost.

For the purposes of this paper, an ECM with only 1 RC pair was considered. The differential equations, introduced in Section 2.2.1, are shown below.

$$\frac{d(U_{th})}{dt} = -\frac{U_{th}}{R_1 C_1} + \frac{I_L}{C_1} \tag{3-2}$$

$$U_L = U_{ocv} - U_{th} - I_L R_o \tag{3-3}$$

It should be noted that current is positive when discharging and negative during charge. The differential equation shown above can be written in discrete form, for a time step *k*.

$$U_{th,l} = \exp\left[-\frac{\Delta t}{\tau}\right] U_{th,k-1} + \left(1 - \exp\left[-\frac{\Delta t}{\tau}\right]\right) R_1 I_{L,k-1} \qquad (3\text{-}4)$$

where $\tau = R_1/C_1$ represents the time constant of the exponential decay. While Equation (3-4) can be utilized for determining the Thevenin voltage drop across the RC pair at each time step, an expression is required for describing the OCV curve as a function of SOC. This can be accomplished by carrying out the characterization test described in Section 3.2.2. The results of the test are shown in Figure 3-7 below.

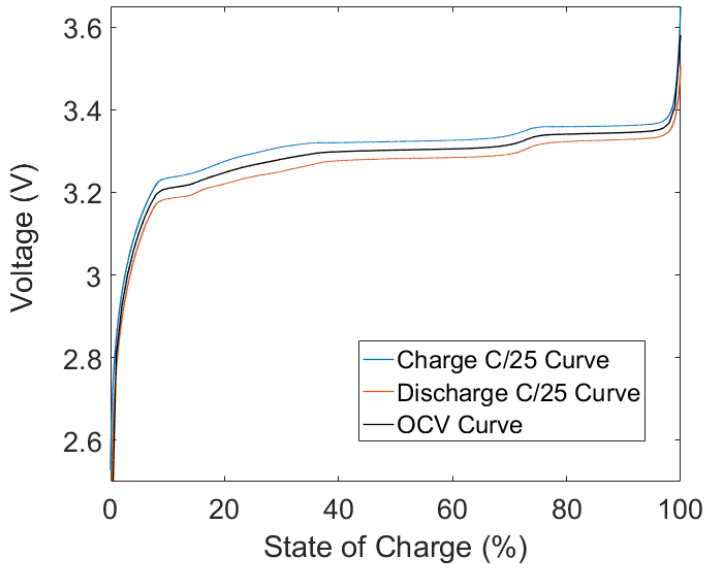

Figure 3-7: The OCV obtained by averaging the C/25 charge and discharge curves.

Examining the above figure, it is evident that the voltage response of the battery differs, depending on whether the battery is being charged or discharged. This difference can be attributed to the battery hysteresis, which depends on the battery's charging/discharging history. For the purposes of this paper, hysteresis will not be modeled in this work. It should be noted that the term hysteresis in this paper will only refer to thermodynamic hysteresis. That is to say, the terminal voltage of the battery is dependent on the direction of the current. For a more comprehensive understanding of this hysteresis term, please refer to Dreyer et al. [109].

Finally, it is important to note that the parameters shown in Equation (3-4) are dependent of the battery temperature, SOC and SOH. Since the parameters are a function of the battery temperature, the thermal model needs to be coupled with the ECM in order to generate accurate predictions.

3.3.2 ECM Parameter Sub-Model

As previously mentioned in Section 3.1, the temperature and SOC dependence on the model parameters is usually described using a two-dimensional LUT. This approach is time consuming, however, as the accuracy of the look-up table is dependent on the size of the grid. A large number of tests need to be carried out in order to accurately model the region between sampling points. This is especially true if an additional, third variable such as SOH is included in the modeling approach. Therefore, this work proposes a design of experiments approach in developing the empirical model, where experiments are only conducted at optimal points. Although the design in this work will only consider battery temperature and SOC, the proposed framework could be easily extended to include battery SOH in future works.

A commonly used design is 2^k, where k represents the number of factors that are being studied. This approach selects the experiments at the high and low levels for each factor. Although the technique only requires 2^k runs, it can only be used to model response surfaces that do not have curvature. In order to account for curvature, the corner points in the 2^k design can be supplemented with additional star points. Experimental design that incorporates addition star points is referred to as central composite designs (CCD). The star points used in this work will be at the center of each face in the factorial space. In other words, the α value for the star points will be set to ±1. The designed experiment is illustrated in Figure 3-8.

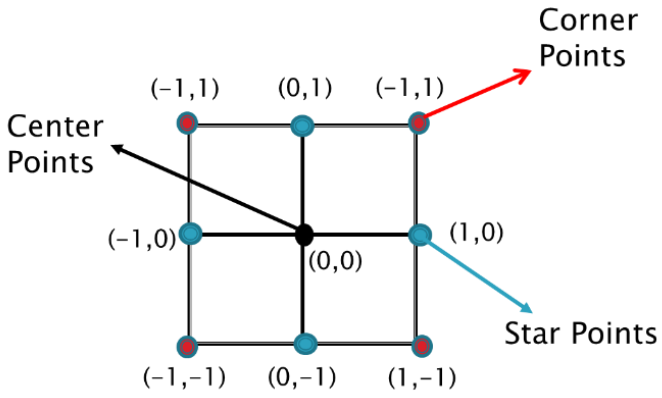

Figure 3-8: Face centered central composite design for ECM parameter surface.

In Figure 3-8, the levels of the two factors are shown in coded form. The values of -1 and +1 represents the min and max for each individual variable. Since it is difficult to get precise HPPC curves when the battery is close to empty or full, the maximum and minimum value of battery SOC will be taken as 90% and 10% respectively. The temperature range for this work will be between 45°C and 5°C. Using the operating range, the experimental conditions for the corner and star points can be determined (Table 3-2).

In addition to the star and corner points shown in the Figure 3-8, center points need to be carried out to get an estimate of the noise. In this work, five HPPC experiments were carried out at the middle temperature of 25°C and middle SOC of 50%. To ensure that the experiments are true replicates, the battery was brought to the same equilibrium point for each run. Sampling error can be obtained by finding the standard deviation of the estimated parameters, R_0, R_1, and C, obtained from the HPPC test. The equation for standard deviation is shown below:

$$s_{p.e}^2 = \frac{\left(X_{i,rep} - \bar{X}_{rep}\right)^2}{N_{rep} - 1} \tag{3-5}$$

where, $X_{i,rep}$ represents the obtained parameter value, $\bar{X}_{rep}$ is the average parameter value and N_{rep} is the total number of replicate runs. In literature, it is often common practice to use the mean squared error (MSE) for obtaining an estimate of the noise variance. This assumption is only valid however, if the model is assumed to fit the data perfectly and the residuals are found to contain only noise. Using replicate runs will allow for a more accurate estimation of the noise variance, which can then be used to determine if the parameters in the model are significant. Finally, based on the experimental procedure described in Section 3.2.5, the HPPC test was conducted at the following test points.

Table 3-2: Experimentally designed conditions for the HPPC test used in developing the ECM parameter surface

	Temperature (°C)	SOC (%)
Corner and Star Points	5	10
	5	50
	5	90
	25	10
	25	50
	25	90
	45	10
	45	50
	45	90
Replicate Run	25	50
	25	50
	25	50
	25	50
	25	50

Developing the ECM parameter model presents a two-level regression approach. First, a non-linear regression analysis needs to be carried out on the HPPC test to identify the circuit parameters at the different operating conditions shown in Table 3-2. Next, a second-order empirical model is used to describe how the ECM parameters change with temperature and SOC. The second-order empirical model is shown below:

$$Parameter = \beta_0 + \beta_1 \mathrm{T}_c + \beta_2 \mathrm{SOC} + \beta_3 \mathrm{T}_c^2 + \beta_4 \mathrm{SOC}^2 + \beta_5 (\mathrm{T}_c * \mathrm{SOC}) + \beta_6 (\mathrm{T}_c^2 * \mathrm{SOC}) + \beta_7 (\mathrm{SOC}^2 * \mathrm{T}_c) + \beta_8 (\mathrm{T}_c^2 * \mathrm{SOC}^2) \quad (3\text{-}6)$$

where T_c represents the surface temperature of the cell. The results from the empirical model are described in Section 3.4 and the developed model is incorporated into the comprehensive modeling frame-work.

3.3.3 Thermal Response Sub-Model

Prediction of the battery temperature requires carrying out an energy balance for the cell. Energy balance indicates that the change in the internal energy of the cell is equal to the heat generated within the cell minus the heat loss to the environment. This can be expressed using Equation (3-7)

$$m_c C_{sp} \frac{dT_c}{dt} = \dot{Q}_{gen} - h_\infty A_{cs}(T_c - T_\infty) \tag{3-7}$$

where m_c is the cell mass, C_{sp} is the specific heat, T_∞ is the ambient temperature and h_∞ is the overall heat transfer coefficient. The term on the left-hand side of Equation (3-7) represents the cell temperature increase, and two terms of the right-hand side represent the heat generation and bulk heat transfer to the environment respectively. It is assumed that heat conduction through the cord, which transfers the current from the cycler to the battery, is negligible. Also, radiation from the cell surface is assumed to be small and is incorporated within the overall heat transfer coefficient.

To apply Equation (3-7), an estimate of the overall heat transfer coefficient is required. For this purpose, the cell temperature profiles during the rest (no-load) periods was utilized. These rest periods occur after each charge/discharge cycle. At the end of rest, it was observed that the cell temperature approaches the ambient temperature. As the current is zero and no heat is generated during the rest period, Equation (3-7) can be simplified as:

$$\int_{T_0}^{T_f} \frac{dT_c}{-T_c + T_\infty} = \int_0^{t_{rest}} \left(\frac{h_\infty A_{cs}}{m_c C_{sp}}\right) dt \tag{3-8}$$

where T_f is the final temperature after the rest period, T_0 is the initial temperature, t_{rest} is the total time of rest and $\frac{h_\infty A_{cs}}{m_c C_p}$ is a constant that depends on the cell parameters. Assuming $\frac{h_\infty A_{cs}}{m_c C_p} = \propto$, the cell temperature during the rest period can be modeled as:

$$T_c = T_\infty + (T_o - T_\infty) e^{-\propto t_{rest}} \tag{3-9}$$

Figure 3-9 shows the fitted and the experimental cell temperature profiles for certain test conditions. It must also be noted that the estimated value of $\propto$ is sensitive to the fluctuations of air circulation patterns in the thermal chamber and may change as the conditions vary.

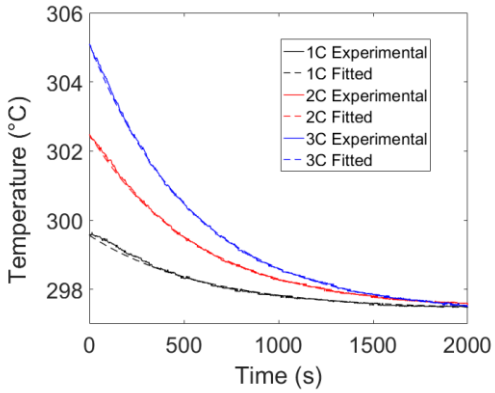

Figure 3-9: The experimental and fitted values for the cooling curves at 1C, 2C and 3C discharge.

Figure 3-9 shows that a good fit is obtained for the cooling curves at various C-rates and starting from different temperature values. Fitting the model results against the experimental data, the average value of $\propto$ was identified as 0.00174 s^{-1}.

3.3.4 Heat Generation Sub-Model

As the battery is cycled, heat generation occurs inside the battery due to two different sources as shown in the equation below [110]–[112].

$$\dot{Q}_{gen} = R_0 I_L^2 - I_L T_c \frac{dU_{OCV}}{dT_c} \tag{3-10}$$

where, U_{OCV} is the OCV, I_L is the applied current, T_c is the cell temperature and R_0 is the internal resistance of the cell, determined through the HPPC test.

The first term on right hand side of Equation 3-10 accounts for the entropic heat generation and is often referred to as the entropic heat. This term can be either positive or negative depending on what direction the current is flowing. The second term lumps together all the irreversible sources and the heat that is generated from resistive dissipation. Since the value of resistance can be obtained from the HPPC test, estimation of the heat generation within the cell only requires knowledge of the dU_{ocv}/dT_c. To obtain the value of this term at a particular SOC, a linear fit is applied to the scatter plot of U_{ocv} versus temperature at each SOC. For a more detailed analysis on how the entropic term can be obtained, please refer to [113]. Figure 3-10 shows the extracted dU_{ocv}/dT_c as a function of SOC for the battery cell under study.

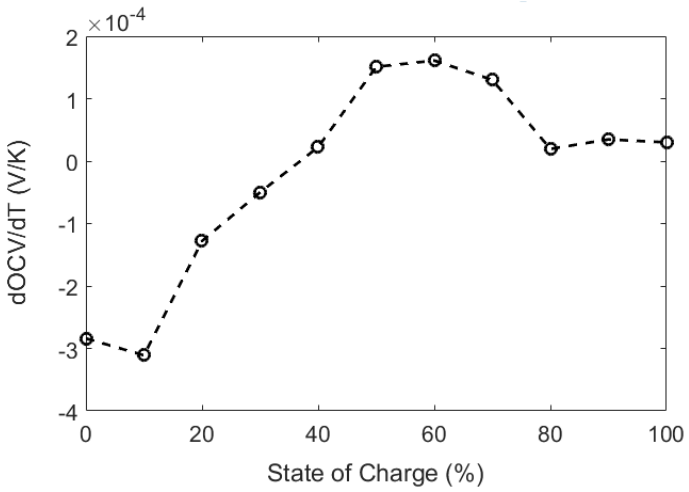

Figure 3-10: The measured dU_{OCV}/dT_c values as a function of SOC.

Examining Figure 3-10, it is evident that depending on the current direction and the SOC, the heat can flow in either directions.

3.4 Results and Discussion

The following section will first examine the ECM parameter results at different temperatures and SOCs. A statistical analysis will then be carried out in order to determine which parameters in the response surface are significant. Next the developed surface will be integrated into the electro-thermal comprehensive model and compared against the experimentally determined temperature and voltage response of the battery. Finally, the predictive capability of the proposed response surface is compared with currently existing approaches from literature.

3.4.1 ECM Parameter Results

The HPPC test was carried out at the experimental conditions shown in Table 3-2. The HPPC test is used to extract the battery resistance parameters at different operating conditions. The non-linear Thevenin model can be used in the identification procedure, where the parameter values are obtained by minimizing the mean sum of squared error.

$$\min\left(\sum_{i=1}^{N}\left(U_{L,i}-U_{exp,i}\right)^2\right) \tag{3-11}$$

where $U_{L,i}$ represents the model voltage, N is the total number of runs and U_{exp} is the experimental voltage. The parameter identification procedure was executed in MATLAB using the Levenberg-Maruardt non-linear least squares.

The estimated battery resistance parameters will then be used as dependent variables in the second regression model. Since the second-order model, shown in Equation (3-12), is linear in the parameters, linear regression approaches can be utilized. It should be noted that three different response surfaces will be generated in this work, one for each ECM parameter. The following equation can be used to find the parameters in the second-order model.

$$\hat{\beta} = (X^T X)^{-1} X^T y \tag{3-12}$$

where $\hat{\beta}$ represents the estimated parameters, X represents the design matrix based on the independent variables and y represents the response variable. In addition to the parameters, the standard error of each individual parameter can be obtained using the equation below.

$$S.E\ (\hat{\beta}) = \sqrt{(X^T X)^{-1}_{ii} * s^2_{p.e}} \tag{3-13}$$

where $s^2_{p.e}$ is the pooled error variance for each specific parameter, determined using center point runs. Using the proposed regression approach, the center point runs can be first analyzed to determine the standard error for each of the three response surfaces. The values are shown in Table 3-3 below.

Table 3-3: The sampling error for the ECM parameters surfaces.

	Sampling Error
Ohmic Resistance (Ohms)	1.88E-05
Thevenin Resistance (Ohms)	5.02E-04
Thevenin Capacitance (F)	2.18E+02

Examining Table 3-3, it is evident that although both the ohmic and Thevenin resistance values are in the same order of magnitude, the variance for estimating the Thevenin resistance is substantially higher than the ohmic resistance. Therefore, accurate analysis of how the ECM parameters change with temperature and SOC requires consideration of the sampling error. Failure to do so will result in incorrect conclusions about which effects are significant.

Once an estimate of the measurement error is obtained, the next step is to determine which parameter in the second order model is significant. A hypothesis test was conducted at a confidence level of 95% to determine if any of the model parameters can be removed. The p-value is shown in Table 3-4, where a value below 0.025 means that the estimated parameter is significant.

Table 3-4: Empirical model parameters for the change in R_0, R_1 and C_1 as a function of temperature and SOC.

Ohmic Resistance Response Surface			
	Parameter Estimate	Standard Error	P-value
Intercept	2.39E-03	1.88E-05	<0.0001
Temp	-2.06E-03	1.33E-05	<0.0001
SOC	-7.14E-05	1.33E-05	0.0058
$Temp^2$	1.43E-03	2.30E-05	<0.0001
SOC^2	-1.93E-05	2.30E-05	0.448
Temp*SOC	2.93E-04	9.38E-06	<0.0001
$Temp^2$*SOC	-2.48E-04	1.62E-05	0.0001
SOC^2*Temp	-1.58E-04	1.62E-05	0.0006
SOC^2*$Temp^2$	1.77E-04	2.81E-05	0.0032
Thevenin Resistance Response Surface			
	Parameter Estimate	Standard Error	P-value
Intercept	3.00E-03	5.02E-04	0.0039
Temp	-1.35E-03	3.55E-04	0.0191
SOC	-1.38E-03	3.55E-04	0.0175
$Temp^2$	2.63E-04	6.14E-04	0.4893
SOC^2	1.20E-03	6.14E-04	0.1222
Temp*SOC	1.18E-04	2.51E-04	0.6637
$Temp^2$*SOC	3.53E-04	4.34E-04	0.4620
SOC^2*Temp	-9.91E-05	4.34E-04	0.8305
SOC^2*$Temp^2$	-4.94E-04	7.53E-04	0.5475
Thevenin Capacitance Response Surface			
	Parameter Estimate	Standard Error	P-value
Intercept	1.41E+04	2.18E+02	<0.0001
Temp	6.27E+03	1.54E+02	<0.0001
SOC	2.16E+03	1.54E+02	0.0002
$Temp^2$	-2.88E+02	2.67E+02	0.3409
SOC^2	-2.22E+03	2.67E+02	0.0011
Temp*SOC	8.51E+02	1.09E+02	0.0015
$Temp^2$*SOC	7.99E+01	1.89E+02	0.6943
SOC^2*Temp	-1.04E+03	1.89E+02	0.0052
SOC^2*$Temp^2$	7.35E+02	3.27E+02	0.0879

Table 3-4 shows that for the ohmic resistance response surface, all the parameters except for SOC^2 were found to be significant. The results reveal that the temperature has a significant effect on the ohmic resistance and second order quadratic terms are required in order to adequately capture this trend. This significant temperature effect stems from the fact that the battery transport properties such as ionic diffusion in electrode particles are highly temperature dependent. There are also significant interaction effects between temperature and SOC, which translates to saying that the effect of SOC on the ohmic resistance is dependent on the temperature.

The parameters for the Thevenin resistance empirical model was found to only contain linear temperature and SOC terms. As temperature and SOC decrease, the Thevenin resistance is found to increase in a linear fashion. Finally, the capacitance is found to change with both temperature and SOC, where a decrease in temperature is found to decrease the Thevenin capacitance. The parameters that were found to be insignificant can be removed and the remaining parameters can be re-estimated. The final parameter values are summarized in Table 3-5 below.

Table 3-5: The final parameter values for the response surface of ohmic resistance, Thevenin resistance and Thevenin capacitance.

Ohmic Resistance		**Thevenin Resistance**		**Thevenin Capacitance**	
Intercept	8.39E-03	Intercept	6.76E-03	Intercept	3.75E+03
Temp	-3.35E-04	Temp	-7.07E-05	Temp	1.71E+02
SOC	-1.93E-05	SOC	-2.63E-05	SOC	7.60E+01
$Temp^2$	4.16E-06			SOC^2	-4.74E-01
Temp*SOC	2.24E-09			Temp*SOC	5.25E+00
$Temp^2$*SOC	1.04E-08			SOC^2*Temp	-4.19E-02
SOC^2*Temp	1.02E-08				
SOC^2*$Temp^2$	-2.40E-10				

The values obtained can be used to generate the response surface and the graphs are shown below.

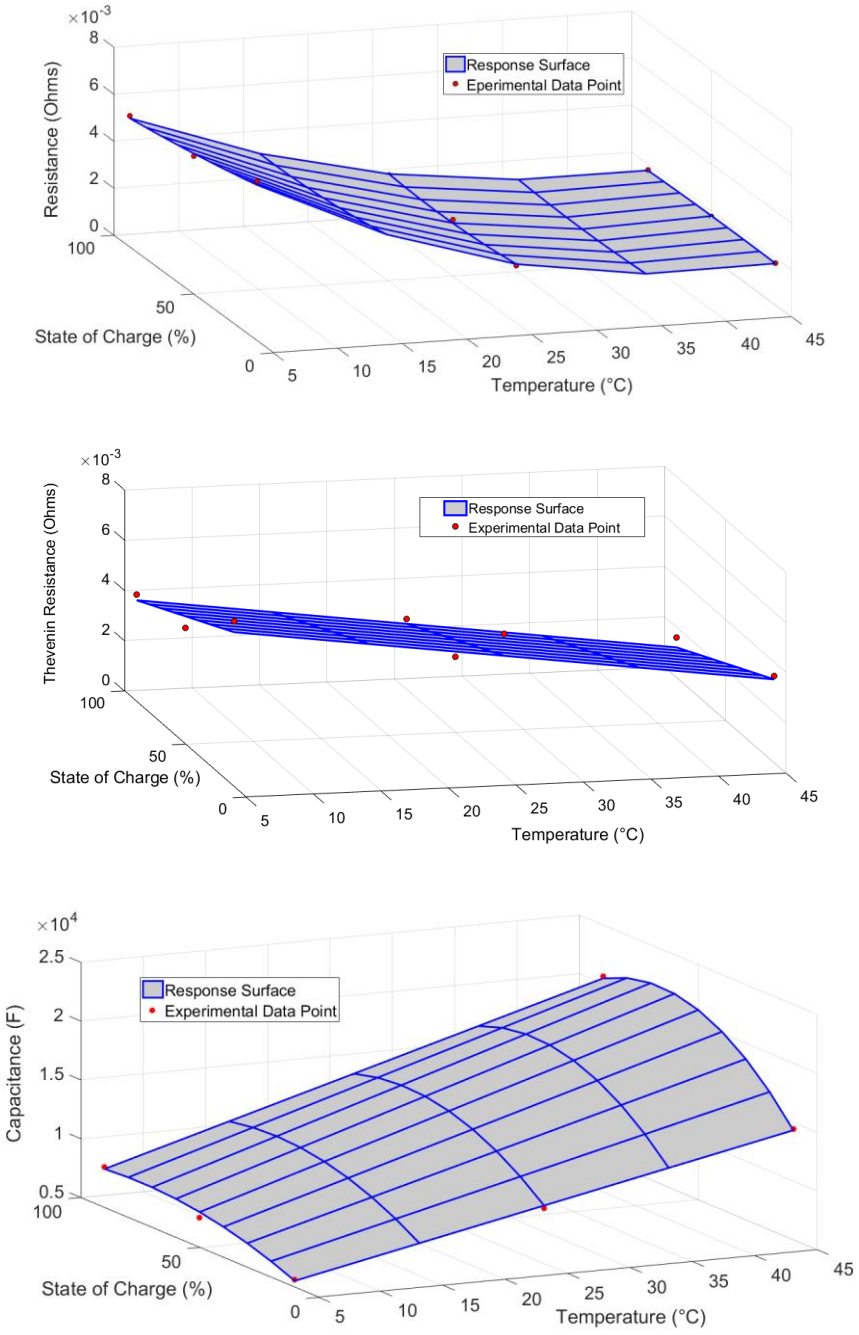

Figure 3-11: Response surface plots and experimental data for the ohmic resistance (A), Thevenin resistance (B), and Thevenin capacitance (C) parameters.

Figure 3-11 shows good agreement between the model output and the experimental data points. The ohmic resistance and Thevenin capacitance surfaces contain a good amount of curvature and therefore a second-order model is required for these parameters. The Thevenin resistance, on the other hand, only requires a linear model in temperature and SOC. Although it is possible that other

correlations are present for this parameter, they cannot be statistically identified due to the higher sampling variance that was present when estimating the Thevenin resistance. Therefore, the results reveal the importance of carrying out a thorough statistical analysis before any conclusions are made.

3.4.2 Temperature Validation Results

Once the ECM parameter sub-model is developed, it was incorporated into the overall battery modeling framework to estimate the temperature and voltage response. To validate the temperature, the Li-ion battery was charged to full and brought to empty using the US-06 drive cycle. The US-06 drive cycle is used to simulate aggressive highway and city driving and can be converted to a current profile using Autonomie software. A Malibu plug-in hybrid, with a 19.7 kWh battery pack consisting of seven 15s3p modules, was used to generate the profile. Although the battery pack was sized for AMP20 pouch batteries, it can be scaled to any size. The current profile for one US-06 cycle is shown in Figure 3-12.

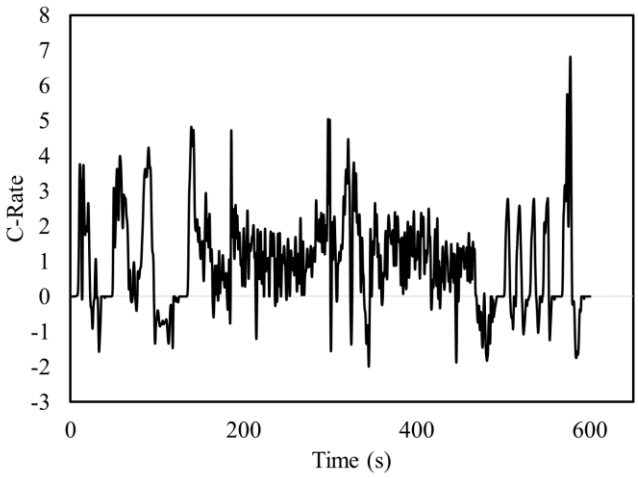

Figure 3-12: Current profile for a US-06 drive cycle simulated in Autonomie.

The validation test was carried out at ambient temperatures of 10°C, 25°C and 40°C and the temperature was monitored using the set-up described in Section 3.2. The temperature predicted by the model was compared to that obtained from the validation experiment, and the results are illustrated in Figure 3-13 below.

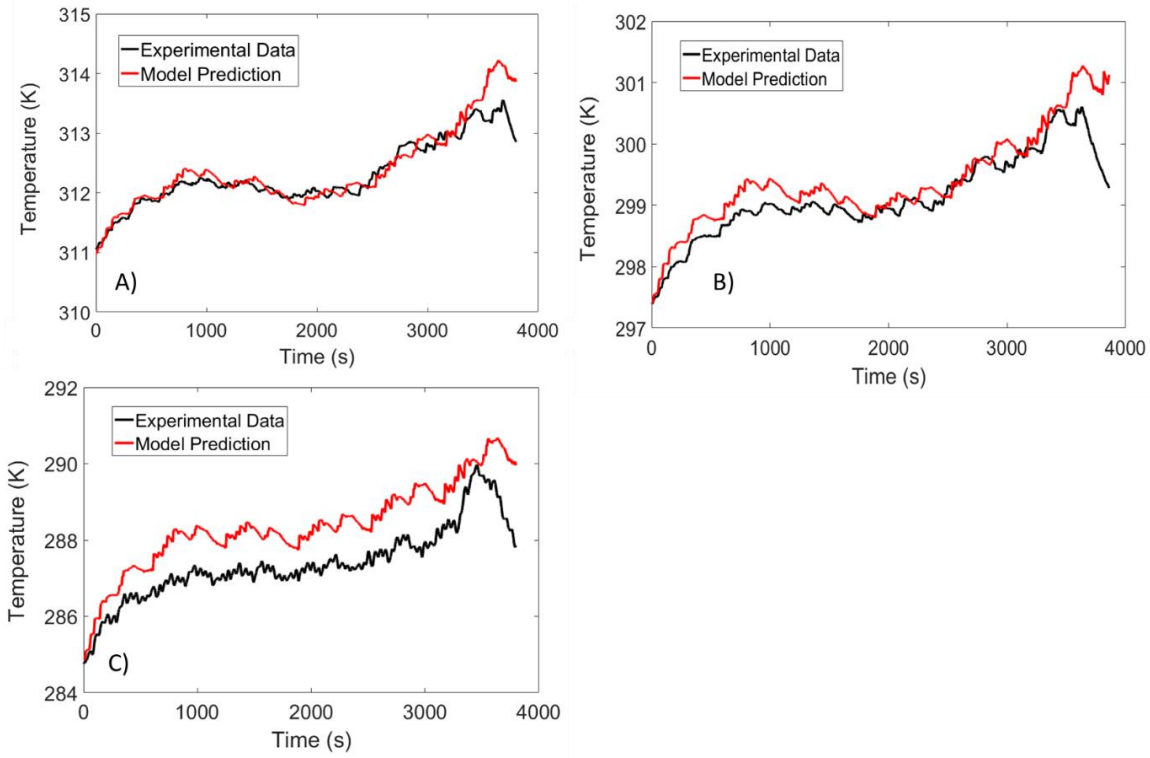

Figure 3-13: Temperature response of a LFP battery subject to a US-06 drive cycle at ambient temperatures of A) 40 °C B) 25 °C and C) 10 °C.

Figure 3-13 shows good agreement between the predicted temperature and the experimental data. The largest deviation between experimental and model data is detected at 10°C, where a root mean squared error (RMSE) of 1°C is observed. The RMSE is calculated for an SOC between 90% and 10% since the ECM parameter surface is identified within this range. The accuracy of the model is similar to predictive models that have been proposed in literature [102], [114]. It is also observed in Figure 3-13 that the battery temperature at the end of drive cycle suddenly decreases. This sudden drop in temperature is due to the entropic heat generation term that resembles an endothermic process at low SOC.

In addition to a drive cycle, the predictive capability of the comprehensive model was further validated by conducting a constant current 1C and 3C discharge experiment. Before discharging, the battery was allowed to rest for 1-hour to ensure it reached thermal equilibrium. The results are summarized in Figure 3-14 below.

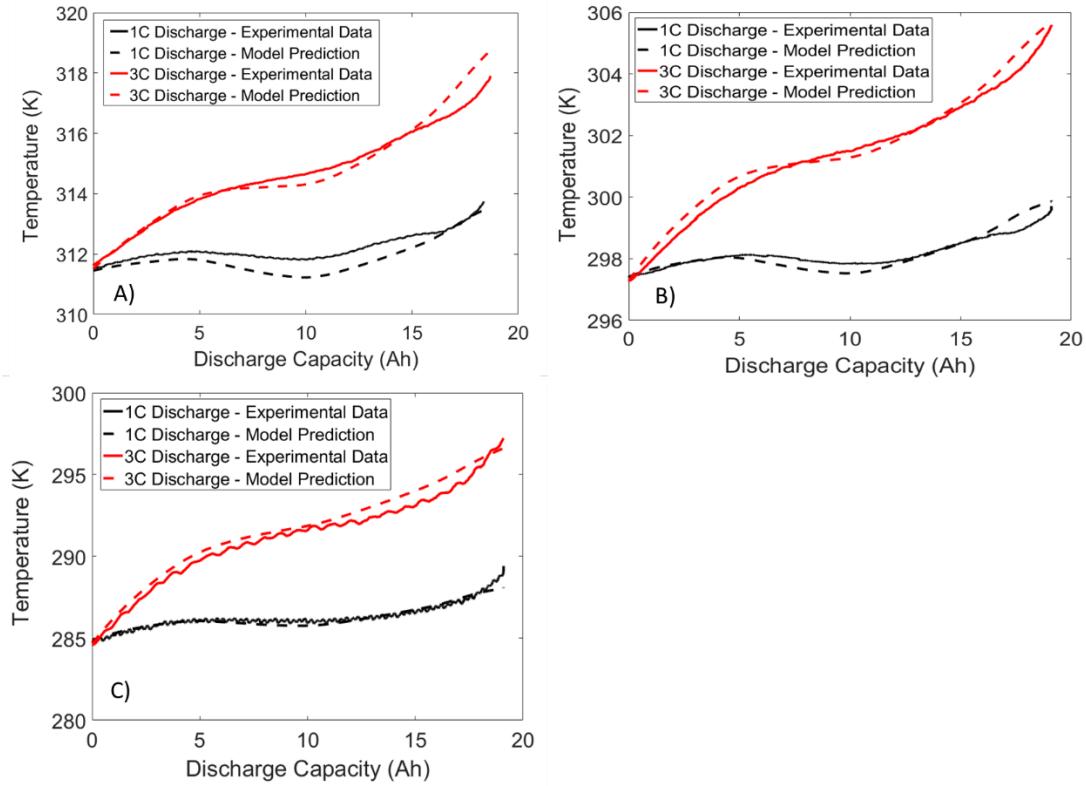

Figure 3-14: Temperature response of a LFP battery subjected to constant current 1C and 3C discharge at ambient temperatures of A) 40 °C B) 25 °C and C) 10 °C.

Examining both Figure 3-13 and Figure 3-14, it is apparent that the temperature response dips slightly at the mid SOC region. This dip is a result of the positive dU_{ocv}/dT values observed in Figure 3-10 at the middle SOC region, resulting lower heat generation and hence a smaller temperature rise. Therefore, the results demonstrate the importance of using the entropic heat generation term when an exact prediction of temperature is required. In addition, strong agreement is found between model and experiment at all temperatures and C-rates. Therefore, the results from these validation experiments suggest that the proposed framework can be utilized by future researchers to accurately predict the temperature response of the battery under dynamic load.

3.4.3 Voltage Validation Results

A comprehensive battery simulator should not only be able to predict the cell temperature but should also accurately capture the voltage drops across the battery terminal. The voltage profiles for the US-06 drive cycle and the 1C/3C discharge cycle are shown in Figure 3-15 and Figure 3-16 respectively.

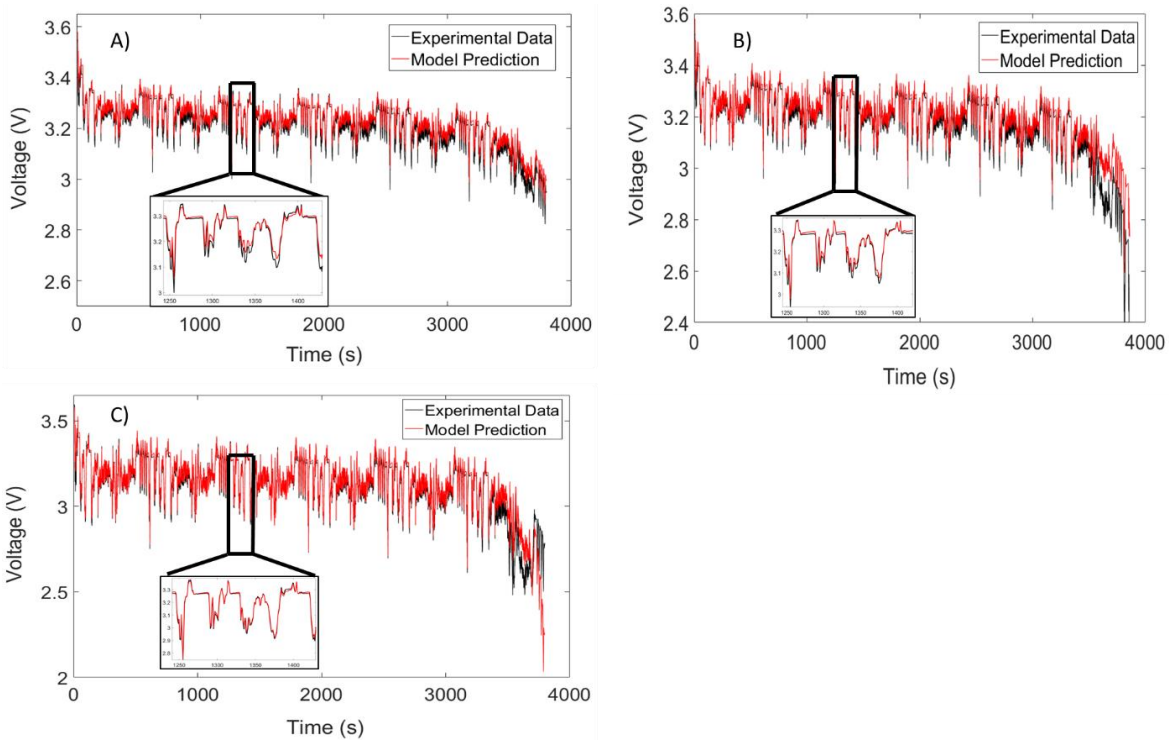

Figure 3-15: The predicted and simulated voltage profile at 1C and 2C/3C charge for temperatures of A) 10 °C, B) 25 °C and C) 40 °C.

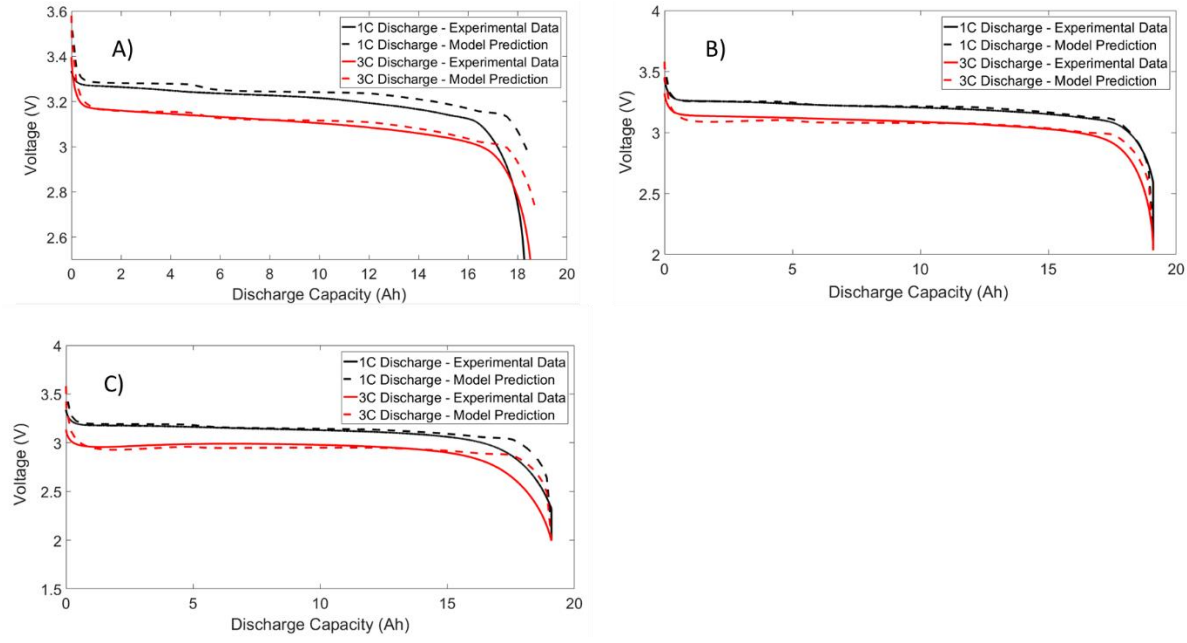

Figure 3-16: The predicted and simulated voltage profile at 1C and 2C/3C discharge for temperatures of A) 10 °C, B) 25 °C and C) 40 °C.

Inspection of the discharge curves (Figure 3-16) indicates excellent agreement between the model and experimental data for most voltage profiles. The model does deviate from the experiment data however, at a lower temperature of °10 C and towards the end of the cycle. One possible reason for this discrepancy could be that the capacity of the battery is not being modeled as a function of temperature. The drive cycle profiles reveal a similar trend, where the model deviates from experimental data at 10 °C. Future work can be carried out in determining whether this effect at cold temperatures can be captured by using additional RC pairs that are dependent on the battery temperature.

3.4.4 Comparison to Existing Approaches

The results reported in Section 3.4.3 show that the proposed model can sufficiently capture the temperature and voltage response of a LFP battery under dynamic loads. By using a design of experiments approach, an accurate battery model can be developed without running a lot of experiments. However, it is important to understand how accurate the ECM parameter surface is in comparison to existing techniques. Therefore, additional experiments were carried out at temperatures of 5 °C to 45 °C in intervals of 10°C and from 90% to 10% SOC in intervals of 10%.

As previously mentioned, there are two techniques that are frequently used to model the ECM parameter response surface. The first method uses a LUT, where sample points in-between are determined through linear interpolation. The second approach, referred in this work as Non-design of experiments (Non-DOE), uses all the data points to develop an empirical model. The approach proposed in this work uses a total of 14 runs, whereas the other two commonly used techniques require 50 runs in total. This can be time consuming since each run requires conducting an HPPC test every two hours. A large amount of time spent characterizing a battery can be expensive for a company. Although using the DOE technique can be economically beneficial to BMS manufacturers, it is important to quantify if there is any loss in accuracy by using this approach.

Using the additional 50 experiments, an LUT model and Non-DOE empirical model were developed and added to the existing battery simulation framework. The same validation profiles shown in Section 3.4.2 and 3.4.3 was run through the simulator and the RMSE for both temperature and voltage were determined. The equation for calculating the RMSE, for N samples is shown below.

$$RMSE = \sqrt{\frac{\sum_{i=1}^{N}(Y_{pred,i} - Y_{exp,i})^2}{N}} \quad (3\text{-}14)$$

where $Y_{i,pred}$ and $Y_{i,exp}$ can be used to represent the predicted and experimental voltage or temperature. Since system identification occurred within the 90% to 10% SOC region, only the RMSE values obtained within this interval will be reported in this work. The value of the root mean squared error for the temperature response of the simulator is shown in below.

Table 3-6: Root mean squared error for the temperature response for LUT and Non-DOE techniques in comparison to the face-center CCD approach.

Temperature RMSE (K)

	10 °C			25 °C			40 °C		
	LUT	Non-DOE	CCD	LUT	Non-DOE	CCD	LUT	Non-DOE	CCD
1C Discharge	0.17	0.17	0.18	0.17	0.17	0.19	0.34	0.40	0.44
3C Discharge	0.60	0.65	0.57	0.59	0.35	0.26	0.47	0.33	0.25
us 06	0.95	1.07	1.07	0.37	0.32	0.25	0.31	0.18	0.13
Average	**0.57**	**0.63**	**0.61**	**0.38**	**0.28**	**0.23**	**0.37**	**0.30**	**0.27**

First, examining the temperature errors from the proposed approach (CCD), the highest error is observed for the US-06 drive cycle at a temperature of 10 °C. This error value is consistent with electro-thermal models proposed by Damay et al. [25], Lin et al. [102] and Sun et al. [115], where maximum RMSE values around 1 K are observed. Therefore, the results from this table further confirm the fact that the electro-thermal model can adequately predict the temperature rise in the battery. This is true for both drive cycles as well as constant current discharges.

Next, it should be noted that similar RMSE values are observed in all three approaches. In some situations, the CCD design fares better, and in others, it fares worse. Therefore, by using the CCD approach, the same degree of accuracy can be obtained while significantly reducing the time required to identify the model. The same analysis can be carried out for the voltage response of the battery and the results are summarized in Table 3-7 below.

Table 3-7: Root mean squared error for the temperature response for LUT and Non-DOE techniques in comparison to the face-center (CCD) approach.

	Voltage RMSE (mV)								
	10 °C			25 °C			40 °C		
	LUT	Non-DOE	CCD	LUT	Non-DOE	CCD	LUT	Non-DOE	CCD
1C Discharge	35.7	31.9	29.3	9.1	10.3	11.5	30.0	35.1	38.5
3C Discharge	45.0	47.1	40.9	38.9	29.6	21.2	15.8	9.3	15.8
US-06	26.7	22.2	20.8	19.5	22.6	24.7	13.0	18.1	22.4
Average	**35.8**	**33.7**	**30.3**	**22.5**	**20.8**	**19.1**	**19.6**	**20.8**	**25.6**

The highest voltage RMSE errors, observed for 3C discharge, are similar in values to those obtained by Lin et al. [102], where the maximum RMSE value was found to be 45 mV. In addition, no difference is observed between the three approaches, leading to the conclusion that additional experiments will not yield more accurate results.

3.5 Conclusions

A comprehensive battery simulator has been developed in this work by considering four different sub-models. A Thevenin ECM was implemented for voltage predictions and an ECM parameter model was utilized for taking into account temperature and SOC dependencies. The ECM parameter model was developed using a DOE approach in order to reduce the number of experiments. The heat generation was determined by considering both irreversible and entropic terms and thermal effects were modeled upon estimation of the heat transfer coefficient. The main conclusions from this works are as follows:

1. The comprehensive battery model developed in this paper can accurately predict the temperature and voltage profiles of the battery under different operating conditions.
2. All three ECM parameters were highly dependent on temperature and SOC, although only a linear dependence was observed for the Thevenin resistance.
3. Replication runs are essential for accurately quantifying the sampling error and identifying which parameters in the model are significant.

4. Using a DOE approach provides the same degree of accuracy as existing techniques while significantly reducing the time required to develop the model.

The results from this chapter will help researchers develop robust real-time battery simulators and thereby advance applications of Li-ion batteries.

Chapter 4: Resistance Estimation Algorithm for Lithium-Ion Battery Packs

The following chapter is based on the paper by Manoj Mathew, Stefan Janhunen, Mahir Rashid, Frank Long, and Michael Fowler submitted to *Energies* entitled: "**Comparative Analysis of Lithium-Ion Battery Resistance Estimation Techniques for Battery Management Systems".**

The author's specific contribution was in developing resistance model and algorithms, conducting all experiments, carrying out the simulations, preparing the results, graphs and manuscript. Stefan Janhunen and Michael Fowler offered guidance on the research, while co-operative education undergraduate students Mahir Rashid and Frank Long helped in implementing the MATLAB code.

4.1 Introduction

The health of a battery changes over time due to the irreversible physical and chemical processes that occur within the cell. The process, known as battery degradation, results in a decrease in capacity and an increase in resistance. Therefore, depending on the type of application, the state-of-health (SOH) of the battery can be defined using either of these two metrics. The central focus of this work will be on developing algorithms for online estimation of the battery resistance.

The internal battery resistance is not a parameter that can be measured, but rather it needs to be inferred from noisy measurements. Inference of the battery resistance is further complicated by model error and computational limitations. Although a higher degree of accuracy can be obtained using a more complex model or algorithm, it often comes at the expense of computational efficiency. Therefore, implementation of a resistance algorithm requires careful consideration on the trade-off between simplicity and accuracy.

A number of approaches have been proposed in literature for estimation of the battery impedance. One commonly used technique is electrochemical impedance spectroscopy (EIS), where an AC excitation current is applied and the corresponding AC voltage response is recorded. Rodrigues et al. [116] used AC impedance to determine battery resistance and used these resistance estimates for determining state-of-charge (SOC). Momma et al. [117] examined the impedance effects at low battery temperatures using EIS. Waag et al. [118] explored the changes in battery

impedance characteristics over the lifetime of the battery, where SOC, temperature, cycling history and current draws are included in the analysis. Although EIS has proved to be a promising method for understanding the battery behavior offline, application of the technique in a battery management system (BMS) is challenging since it requires special circuits for generating the required signals.

Online estimation techniques of battery internal resistance generally fall into two distinct groups. In the first group, the battery is modeled using an using an electrochemical model, where the model parameters are estimated online [119], [120]. Inference of these parameters, especially the parameters associated with battery impedance can provide insights into the degradation of the battery pack. However, implementation of these complex models can be difficult in a BMS, where computational resources are limited.

The second, more frequently applied group of techniques involve modeling the battery using an equivalent circuit model (ECM) and estimating the circuit parameters online. Once again, the estimates of the circuit parameters are useful in determining the battery's SOH. Adaptive filtering methods can then be utilized to obtain optimal parameter estimates from noise data. These methods are frequently coupled with SOC estimation, where estimation of the model parameters in the ECM can be used as an estimate for the internal resistance. For example, Sun et al. [34] applied an adaptive extended Kalman filter (AEKF) for estimation of battery resistance in conjunction with SOC. Chiang et al. [121] developed an algorithm based on the Lyapunov-stability criteria to estimate the internal resistance and the open-circuit voltage (OCV). Wei et al. [122] have proposed a recursive least squares (RLS) approach for estimating resistance based on an ECM. Remmlinger et al. [35] used a specific excitation signal, found during normal operation of a hybrid electric vehicle, along with RLS algorithm to estimate battery resistance. Finally, Dai et al. [123] proposed a parameter estimation framework composed on two modules running on different time-scales. The EKF algorithm was applied for estimating the parameters associated with battery slow dynamics, while the RLS algorithm was used for modeling the faster battery dynamics.

Although the methods mentioned above provide reliable resistance estimates, they can become computationally expensive when implemented on a large battery pack, composed on hundreds of cells. One approach to deal with this issue has been proposed by Lievre et al. [124], where the resistance is estimated from the voltage drop across the battery, caused by large current variations

in the profile. However, Lievere et al. considered both the ohmic and diffusion resistance when calculating their SOH metric. This paper will explore the effectiveness of using only the ohmic resistance in determining whether a cell needs to be replaced. The algorithm implementation can be significantly simplified by only considering the ohmic resistance and not the other time dependent elements in the ECM. The proposed approach, referred to in this paper as direct resistance estimation (DRE), estimates the ohmic resistance only when the battery experiences sharp pulses in current. The resistance estimates from the DRE technique will then be compared to more advanced adaptive filtering methods such as the EKF and RLS. The goal of this paper is to determine under what conditions the DRE approach is sufficient and when a more advanced, computationally expensive algorithm is required. These findings will be beneficial for future researchers in trying to find a balance between algorithm complexity and accuracy.

4.2 Experimental Set-up and Procedure

4.2.1 Cell Selection and Degradation

The algorithms under consideration are tested on a battery pack composed of four lithium iron phosphate (LFP) cells. Two relatively fresh cells are used in the pack, combined with two cells with a significant amount of degradation. The addition of the two damaged cells allows one to test the robustness of the algorithms under different aging conditions.

Battery degradation that occurs during the charging and discharging cycles is referred to as cycling aging. Battery degradation can also happen when the battery is at rest, and this type of aging is known as calendar aging. In this paper, two LFP cells are brought to different SOH values through accelerated calendar aging, where the batteries are stored for extended periods of time at elevated temperatures. The capacity and resistance of each cell in the battery pack are reported in Table 4-1.

Table 4-1: Capacity and ohmic resistance of the four LFP cells used in this study

Cell Number	Cell Capacity (Ah)	Ohmic Resistance (Ohms) at 50% SOC
1	18.5	0.00299
2	11.7	0.00675
3	18.4	0.00292
4	16.1	0.00452

Cell 2 was degraded by fully discharging the cell to 0% SOC and then storing the battery at 50°C for 24 months. Cell 4, on the other hand, was degraded by fully charging the battery to 100% SOC and then storing the cell at 50°C for six months. In both cases, a thermal chamber was utilized to maintain the battery at a constant temperature. The lower storage time for cell 4 resulted in a higher capacity and lower resistance, when compared to cell 2. Examination of the resistance values in Table 4-1 shows that there is a large spread in the ohmic resistance of the different cells in the pack. The goal of this paper is to test the algorithms and determine which ones can accurately detect this difference and correctly pinpoint the problematic cells in the pack.

4.2.2 Cell Characterization

Although the cell parameters for a given battery model will be identified online, the open-circuit voltage (OCV) curve is obtained offline. The OCV curve for the battery is generated using the following procedure:

1. The battery is charged to full at 1C using constant-current/constant-voltage (CCCV) protocol.
2. The battery is discharged to empty at a rate of C/25.
3. The battery is charged to full at a rate of C/25.

The OCV curve can be obtained by taking the average of the charge and discharge curves. It should be noted that the effect of aging on the OCV curve is not considered for this study. This effect should be minimal, however, since only the ohmic resistance of the battery is being estimated.

4.2.3 Test Bench for Algorithm Validation

The test bench shown in Figure 4-1 was developed to validate the resistance estimation algorithms.

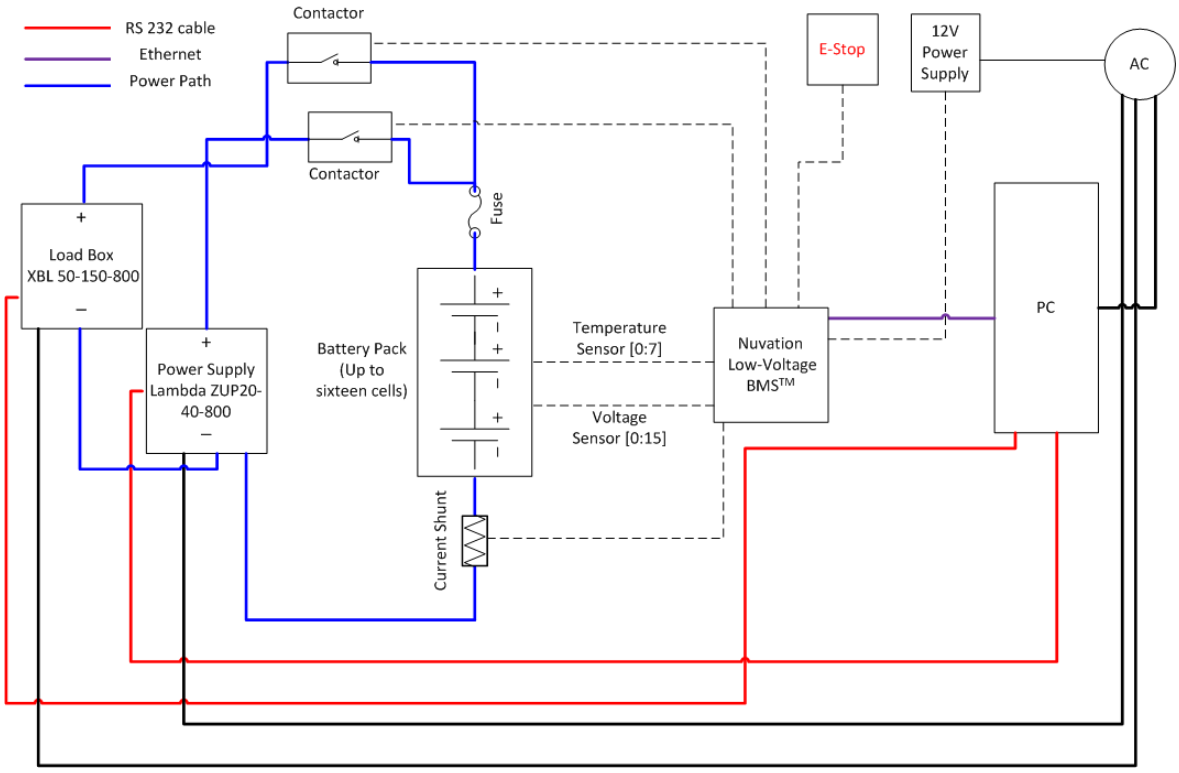

Figure 4-1: Test bench used in validating the resistance estimation algorithms.

Charging and discharging of the battery pack can be carried out using the XBL load box and Lambda Zup power supply. The power supply can deliver a maximum of 40 A with a voltage limit of 20 V whereas the loadbox has a maximum voltage and current of 150 A and 80 V respectively. Both the power supply and load box communicate remotely using a serial interface, and the commands are executed using Python. For safety purposes, two contactors are included in the circuit, one for the charge loop and one for the discharge loop. A Nuvation Low Voltage Battery Controller™ is utilized for temperature, current, and cell voltage measurements along with cell balancing, and pack safety. The experimental data obtained from the test bench can be used for testing the different resistance estimation algorithms.

4.2.4 Current Profile for Algorithm Validation

To simulate what a battery pack would experience in a PHEV or HEV application, the current profile used on the test bench was derived from three drive cycle profiles: The Urban Dynamometer Driving Schedule (UDDS), Highway Fuel Economy Test (HWFET) and US06. UDDS is a cycle that is used to represent driving in an urban environment, while HWFET represents driving conditions on the highway. US06 drive cycle, on the other hand, is used to

simulate aggressive driving with extensive periods of acceleration. The combination of these three profiles will provide an accurate representation of the type of current transients a battery might experience during regular operation in a vehicle.

Drive cycles are reported as speed over time and therefore, was converted into a current profile using Autonomie software. Using the software, a Malibu plug-in hybrid with a 19.7 kWh battery pack consisting of seven 15s3p modules is simulated. Although the battery pack was sized for an AMP20 pouch battery, it can be scaled to any size. Figure 4-2(A-C) below shows the different drive cycles that are utilized in this paper.

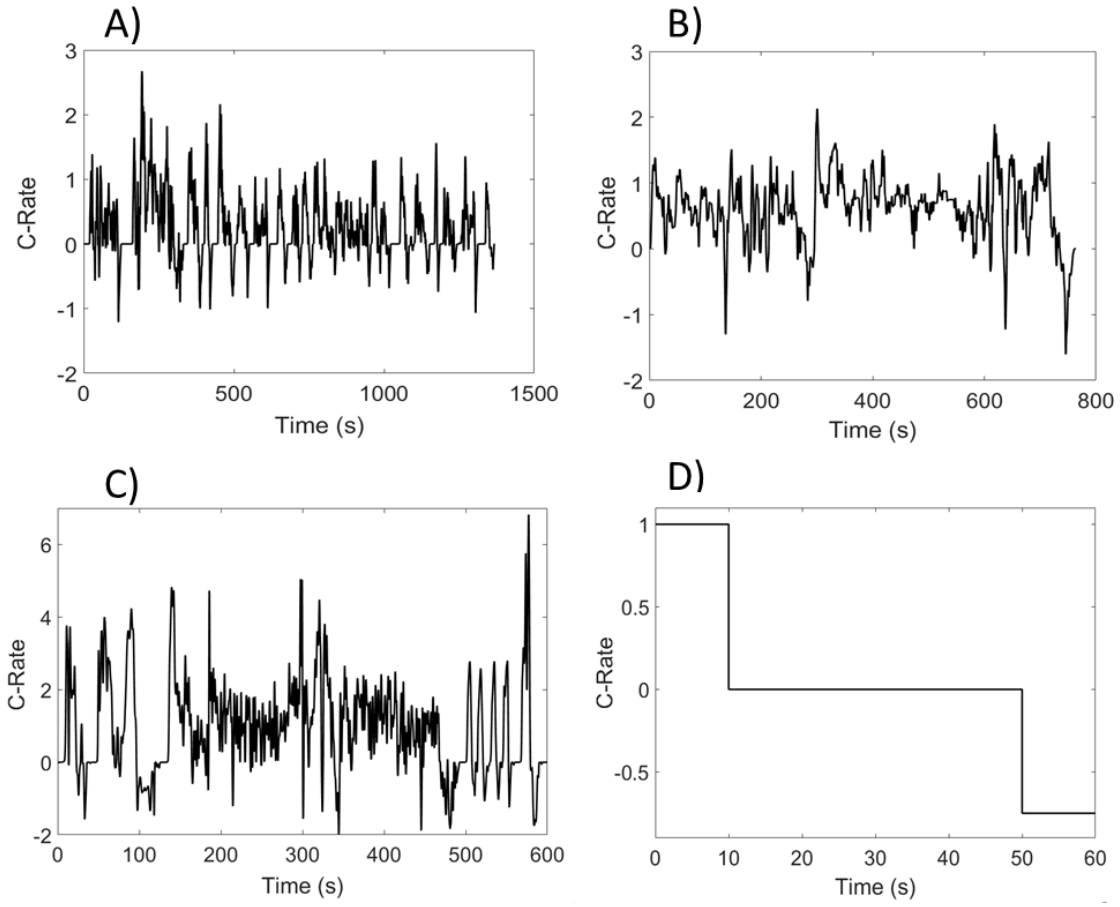

Figure 4-2: (A) Urban Dynamometer Driving Schedule (UDDS), (B) Highway Fuel Economy Test (C) US06 and (D) HPPC current profile used in validating the resistance estimation algorithms.

In addition to the drive cycles, a hybrid pulse power characterization (HPPC) test was carried out at the beginning of each test. The HPPC test is frequently used in identifying the resistance of the battery [108]. The test consists of a 10 second discharge at 1C, followed by a 40 second rest

period and 10 second charge at ¾ C. The test profile is shown in Figure 4-2 D. The ohmic resistance obtained from the HPPC test provides a baseline upon which all other online estimation algorithms can be compared.

4.3 Algorithm Development

Before describing the estimation algorithms, it is important to define what is meant by battery internal resistance. Although this was briefly described in Section 3.3.1, a more comprehensive explanation will be given in this section. Figure 4-3 better illustrates the different resistances that are present in a lithium-ion (Li-ion) cell.

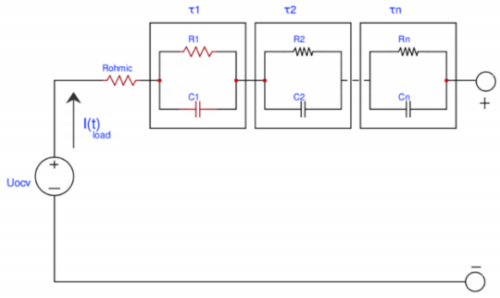

Figure 4-3: ECM commonly used in describing the voltage response of Li-ion batteries.

The battery impedance is the sum of a few different processes that occur within the battery. The first resistor in the above circuit, referred to as R_o, represents the sum of the ionic resistance of the electrolyte as well as the electric resistance of the current collector and the electrical tabs. It models the instantaneous voltage drop that occurs as soon as a current is applied. To capture the time-dependent voltage response, *n* number of resistor/capacitor (RC) pairs can be added to the circuit. The RC pair with a smaller time constant is often used to represent the resistance associated with the charge-transfer reaction as well as the double layer capacitance that occurs at the surface of the electrode. The RC pair with a larger time constant represents the diffusion phenomenal that occurs within the battery. Additional RC pairs are often included to increase the accuracy of the ECM.

Determination of SOH in this paper will be based on the pure ohmic resistance. Studies have shown that R_o is a strong indicator for the SOH of the battery [125]–[128]. Therefore, all three algorithms proposed in this paper will estimate the pure ohmic resistance of the battery. Comparison of the results from each technique will also provide insights into whether or not the ohmic resistance is sufficient for identifying a damaged cell at different operating conditions.

4.3.1 Direct Resistance Estimation

The proposed algorithm, referred to in this work as direct resistance estimation (DRE), utilizes a moving time window for continuously checking the current profile for rapid current transients. When a significant change in both current and voltage is detected by the BMS, Ohm's law can be used to estimate the resistance (Equation (4-1)).

$$R_{ohm} = \frac{(U_{L,t} - U_{L,t+\Delta t})}{(I_{L,t} - I_{L,t+\Delta t})} \tag{4-1}$$

where R_{ohm} is referred to as the instantaneous resistance, ΔU_L is the terminal voltage, $I_{L,t}$ is the applied current and Δt is the time step of the moving window. Current and voltage fluctuations below a minimum threshold, represented by ΔI_{min} and ΔU_{min} respectively, will not be considered in determining the resistance. In addition, the length of the moving window (Δt) should be kept as small as possible to estimate only the ohmic resistance. Utilization of a larger time window would produce values that contain activation and concentration polarization effects in addition to the ohmic component. The algorithm is summarized in Figure 4-4.

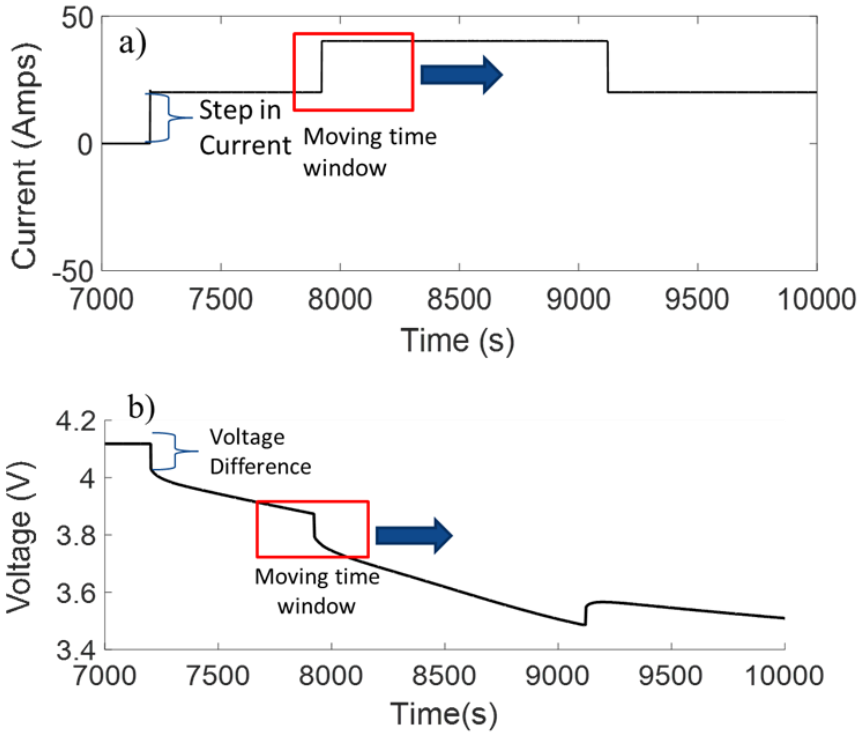

Figure 4-4: DRE approach using a moving window to detect pulses in current and voltage.

The estimates obtained using Ohm's law would contain a significant amount of noise due to measurement errors in the BMS sensors. Therefore, an exponentially weighted moving average (*EWMA*) filter will be utilized. The filter has been shown by Lievre et al. [124] to provide substantial noise reduction while being computationally efficient. One significant advantage of using this filter is that it requires only storage of the previous mean value. A smaller memory requirement is essential for implementation in a BMS, especially when considering a large battery pack composed of hundreds of cells.

The EWMA is a moving average filter where the past values are weighted by a tunable constant λ_{EWMA}. The constant represents the depth of memory, where using a large λ_{EWMA} value will produce more smoothing in the output. The equation of EWMA can be written as follows:

$$R_{filtered,k} = (1 - \lambda_{EWMA}) * R_{filtered,k-1} + (\lambda_{EWMA}) R_{ohm,k} \qquad (4\text{-}2)$$

where, $R_{filtered,k}$ represents the current filtered resistance estimate, $R_{filtered,k-1}$ is the previous value of the filtered resistance estimate and $R_{ohm,k}$ is the raw ohmic resistance.

There are two significant advantages in using the DRE method for estimating the battery resistance. First, the algorithm does not require an OCV curve or other chemistry specific battery parameters. Therefore, no initial battery characterization or training data is needed before the algorithm can be used in a BMS. The second advantage of this algorithm is that unlike the EKF and RLS approaches, it does not require complex matrix calculations. The lower computational cost is a significant advantage, especially when one is considering implementing the algorithm in an embedded system. No research currently exists in literature that discusses the accuracy of such a simple resistance estimation technique in comparison to some of the more well-established algorithms. Therefore, in light of the advantages listed above, it is valuable to analyze the relative performance of these algorithms.

4.3.2 Extended Kalman Filter

Kalman filters have been utilized in a number of different fields including control of complex dynamic systems, such as aircrafts, ships, satellites as well as robotics[129]. As advancements continue to be made in the field of Li-ion batteries, Kalman filters are a promising algorithm that can help estimate the internal states of the battery[130]. They have also been utilized for online estimation of battery parameters such as R_o and R_1 to provide insights into the health of the battery.

Therefore, the EKF algorithm will be one of the three algorithms that will be compared in this work.

As previously mentioned, resistance is an intrinsic property of the Li-ion battery that cannot be directly measured. Therefore, the EKF algorithm is used to estimate it based on measurable outputs. Before application of the algorithm, it is important to select a model for describing the battery voltage response in discrete-time. For this paper, the ECM shown in Figure 4-3 will be reduced to include only the ohmic resistance and one *RC* pair. This model is referred to as the Thevenin model, and the components of this model are shown in red in Figure 4-3.

Since the goal of this paper is to provide a comparison between different parameter estimation algorithms, only a brief discussion of the EKF will be given in this section. A more in-depth analysis of the filter equations will be presented in Chapter 6 of this work. In addition, a series of paper written by Plett [33], [73], [74], clearly demonstrate how these filters can be applied to Li-ion batteries. All the equations associated with the EKF implementation are summarized in Table 4-2 below.

Table 4-2: Summary of the EKF equations [74]

State-space models for parameter estimation:

$$\theta_{EKF,k+1} = \theta_{EKF,k} + r_{par,k} \tag{4-3}$$

$$y_{EKF,k} = g\left(x_k, u_k, \theta_{EKF,k}\right) + e_{EKF,k} \tag{4-4}$$

$$U_{L,k} = U_{OCV,k} - R_0 I_k - U_{th,k}$$

Definition:

$$C_k^{\theta} = \left.\frac{dg(\hat{x}_k^-, u_k, \theta)}{d\theta}\right|_{\theta = \hat{\theta}_{EKF,k}^-} \tag{4-5}$$

Computation:

For k = 1,2, … N

Time update:

$$\hat{\theta}_{EKF,k}^- = \hat{\theta}_{EKF,k-1}^+ \tag{4-6}$$

$$\Sigma_{\tilde{\theta},k}^- = \Sigma_{\tilde{\theta},k-1}^+ + \Sigma_r \tag{4-7}$$

Measurement update:	$L^{\theta}_{EKF,k} = \Sigma^{-}_{\tilde{\theta},k}(C^{\theta}_{k})^{T}[C^{\theta}_{k}\Sigma^{-}_{\tilde{\theta},k}\left(C^{\theta}_{k}\right)^{T} + \Sigma_{e}]^{-1}$	(4-8)
	$\hat{\theta}^{+}_{EKF,k} = \hat{\theta}^{-}_{EKF,k} + L^{\theta}_{EKF,k}[U_{L,k} - g\left(\hat{x}^{-}_{k}, u_{k}, \hat{\theta}^{-}_{EKF,k}\right)]$	(4-9)
	$\Sigma^{+}_{\tilde{\theta},k} = (I - L^{\theta}_{EKF,k}C^{\theta}_{k})\Sigma^{-}_{\tilde{\theta},k}$	(4-10)

Assuming that θ_{EKF} represents a vector containing the true values of the battery model parameters, the goal is to adapt $\hat{\theta}_{EKF}$ such that it converges to the true value. Equation (4-3) represents the state space model for the parameters, where the parameters are essential constant but can change gradually over time as the battery is operated during different conditions. The output equation, shown in Equation (4-4), represents the cell voltage output, which can be determined by solving the Thevenin equivalent circuit.

The EKF algorithm is composed of two distinct steps: the state/parameter update and the measurement update. The parameter update is based on the state-space equation, where the parameter estimates θ_{EKF} and the parameter error covariance matrix, Σ_{θ} are propagated in time one sampling interval using Equations (4-6) and (4-7). The measurement update is then used to incorporate additional knowledge acquired from the new measurement sample and updates the parameter value accordingly. The magnitude of the measurement update is based on the size of the Kalman gain, shown in Equation (4-9). If there is more confidence in the measurements than in the parameters, a large measurement update is carried out. Using this approach, the parameters can be continuously updated as new measurements are made available. It should be noted that initial guesses are required for both the process (Σ_{r}) and measurement (Σ_{e}) covariances as well as the parameter covariance $\left(\Sigma_{\tilde{\theta},k}\right)$. Therefore, development of an efficient filter requires tuning of these covariance matrices.

4.3.3 Recursive Least Squares

Online identification of the ohmic resistance can also be implemented using the RLS algorithm. The algorithm works by minimizing the difference between the estimated model voltage and the measured terminal voltage [34], [131]. Due to its recursive nature, an optimal forgetting factor is required to reduce the influence of old data and update the parameters as new data is made available. To apply the proposed RLS algorithm, an auto regressive exogenous (ARX) model is

required. For this paper, only the main model equations will be presented. For a more detailed analysis on the derivation of this model, please refer to He et al.

Equation (4-11) represents the ARX model, where φ_k is the input vector, $\theta_{RLS,k}$ is the parameters vector, $y_{RLS,k}$ is the estimated system output (i.e., terminal voltage $U_{L,k}$), and k is a non-negative integer which represents the sample interval. The value of the constants a_1, a_2, a_3 can be used to solve for the ECM parameters R_0, R_1, and C. Similar to the EKF, the new voltage measurements can be used to update the parameters, where the size of the update is dependent on the algorithm gain $L_{RLS,k}$. The update equation is shown below. The forgetting factor, λ_{RLS}, can be included when calculating the algorithm gain and was initially set to 0.999 in this work.

Table 4-3: Summary of the RLS equations [131]

Auto Regressive Exogenous (ARX) Model:

$$y_{RLS,k} = \theta_{RLS,k}\,\varphi_k + e_{RLS,k} \tag{4-11}$$

where $y_{RLS,k} = U_{L,k}$

Initialization:

$$\hat{\varphi}_k = [1 \;\; U_{L,k-1} \;\; I_{L,k} \;\; I_{L,k-1}] \tag{4-12}$$

$$\hat{\theta}_{RLS,k} = [\left(\left(1 - a_{1,k}\right) * U_{ocv,k}\right) \;\; a_{1,k} \;\; a_{2,k} \;\; a_{3,k}] \tag{4-13}$$

$$a_1 = -(T_s - 2R_1C_1)(T_s + 2R_1C_1)^{-1} \quad a_2 = -(R_0T_s + R_1T_s + 2R_0R_1C_1)\,(T_s + 2R_1C_1)^{-1} \quad a_3 - (R_0T_s + R_1T_s - 2R_0R_1C_1)(T_s + 2R_1C_1)^{-1} \tag{4-14}$$

Computation:

For k = 1,2, … compute

$$L_{RLS,k} = P_{k-1}\varphi_k^T\,[\lambda_{RLS} + \varphi_k^T P_{k-1}\varphi_k] \tag{4-15}$$

$$P_k = P_{k-1} - (L_{RLS.k}\,\varphi_k^T\,P_{k-1})\,\lambda_{RLS,k-1}^{-1} \tag{4-16}$$

$$\hat{\theta}_{RLS,k} = \hat{\theta}_{RLS,k-1} + L_{RLS,k}\,[U_{L,k} - \varphi_k\hat{\theta}_{RLS,k-1}] \tag{4-17}$$

4.4 Results and Discussion

4.4.1 Algorithm Validation at Different SOH Values

The Li-Ion battery pack was subjected to a current profile that would be typically experienced by an HEV or PHEV type application. The profile was developed by combining the UDDS/US06/HWFET drive cycles together. These three drive cycles were used to simulate both highway as well as urban driving conditions. In addition, an HPPC test was conducted before the start of each cycle. The input current profile along with the corresponding voltage response for the battery pack is shown in Figure 4-5.

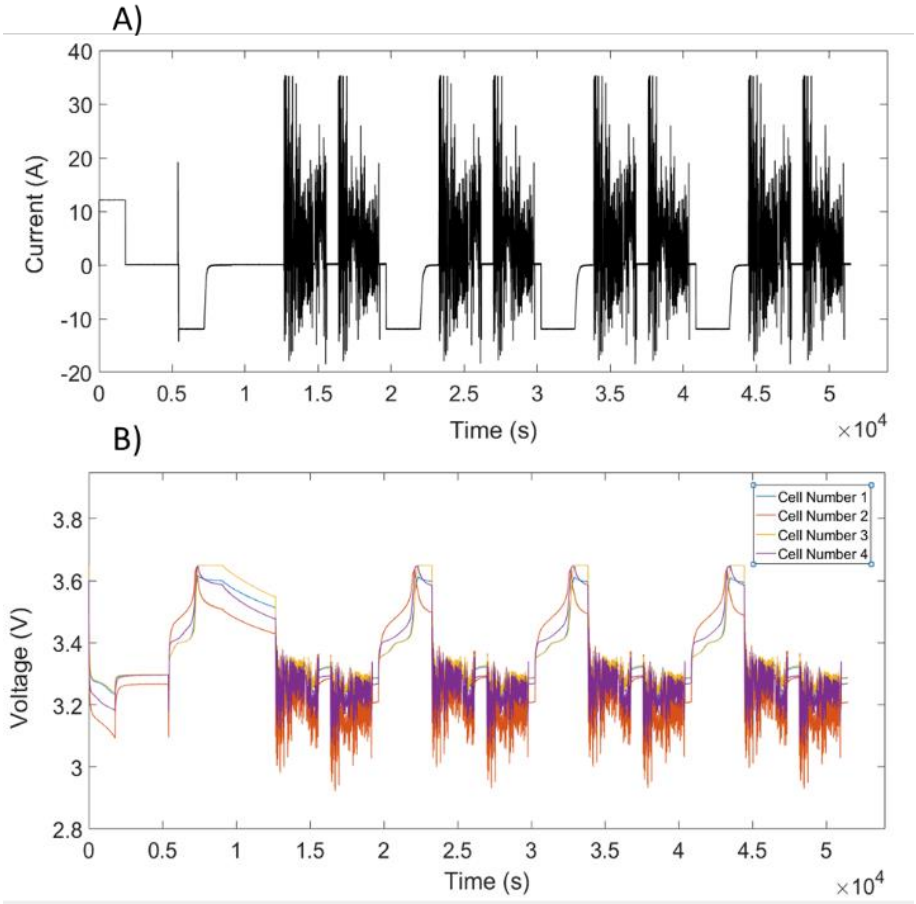

Figure 4-5: The validation current profile (A) and the corresponding voltage response (B) for the LFP battery pack at a constant temperature of 20°C.

Examining Figure 4-5 B), it is evident that the resistance of cell 2 is significantly greater than the other three cells based on the significant voltage drops. Cell 4 has the second largest resistance while cell 1 and 3 have the smallest. Given the substantial difference in the voltage response among

the cells, all three resistance estimation algorithms will be tested on this profile to determine whether they can accurately estimate the battery resistance.

The three estimation algorithms were developed in MATLAB and executed using the voltage and current data obtained from the test bench. The nominal resistance of each cell was set to 2500 µOhms to determine whether the algorithm could intelligently converge to the actual resistance of the individual battery. The results are shown in the Figure 4-6 below.

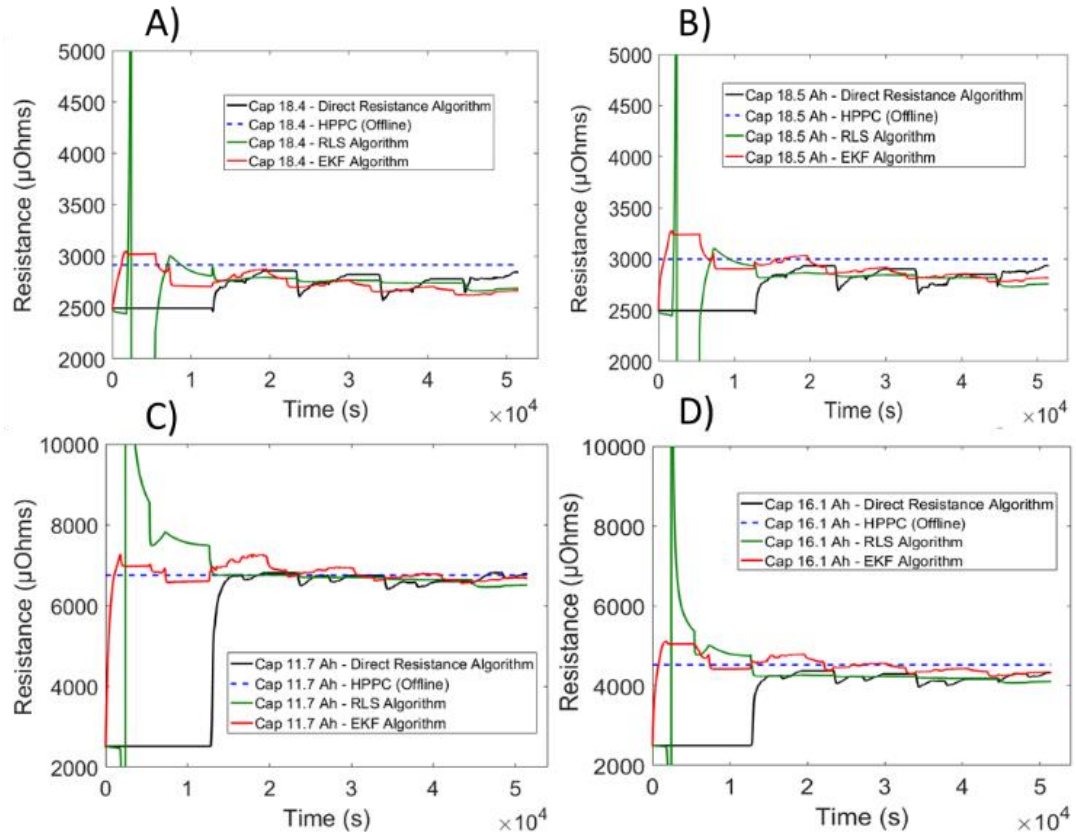

Figure 4-6: Resistance estimations from the HPPC test, EKF algorithm, RLS algorithm and DRE algorithm for cell one (A), two (C), three (B) and four (D) at a temperature of 20 °C.

The resistance obtained from the HPPC profile will be used as the reference when comparing the accuracy of the three resistance algorithms. Examining the results shown in Figure 4-6, it is evident that all three algorithms converge to the reference resistance value, given by the HPPC test. Although the initial guess for each algorithm was set to 2500 µOhms, the output estimates matched the battery's true resistance values after the first few cycles.

It should also be noted that the DRE approach can provide the same degree of accuracy when estimating the ohmic resistance, as the more advanced algorithms. Table 4-4 provides a comparison of the averaged percent error of all three approaches. It was assumed that each of the three algorithms have converged after 20,000 seconds and the percent error is averaged from this point to the end of the test. The percent error for the DRE algorithm is in the same range as the error for RLS and EKF. These results indicate that by using a more simplified and computationally efficient approach, the same degree of accuracy can be obtained in estimating battery resistance.

Table 4-4: Comparison of the average percent error from the DRA algorithm, RLS algorithm and EKF algorithm for a battery pack maintained at 20 °C.

	RLS Error (%)	EKF Error (%)	DRA Error (%)
Cell 1	6.21	5.11	5.04
Cell 2	1.66	1.39	1.58
Cell 3	6.10	7.68	5.15
Cell 4	7.43	2.91	6.87

It is also important to compare the convergence speed of the algorithm from its initial guess. The EKF can converge to the actual resistance value at a much faster rate than the other two methods. This is evident for all four cells in the battery pack. However, the disadvantage of using this approach is that it needs significant computational resources and requires careful tuning of the covariance matrices. The RLS method, on the other hand, requires less tuning but takes a longer time to converge to the correct resistance value. Finally, the DRE algorithm is not able to update the resistance during the initial part of the test, since this portion of the profile does not contain rapid changes in current. The algorithm does, however, quickly converge to the correct resistance value during the drive cycle portion of the profile. Therefore, although the direct resistance algorithm is simple, computationally inexpensive, and can accurately track battery SOH, it requires sufficient excitation in the input current to provide accurate results.

4.4.2 Algorithm Validation at Different Temperatures

In addition to battery degradation, temperature has a significant effect on the ohmic resistance of the battery. A decrease in temperature has been found to significantly increase the battery's internal resistance. Therefore, to test the robustness of the algorithms under different operating conditions, the same profile is shown in Figure 4-5 A was carried out at three additional temperatures of 10

°C, 30°C and 40 °C. The results are captured in Figure 4-7 for a fresh cell and Figure 4-8 for the cell with the highest amount of degradation.

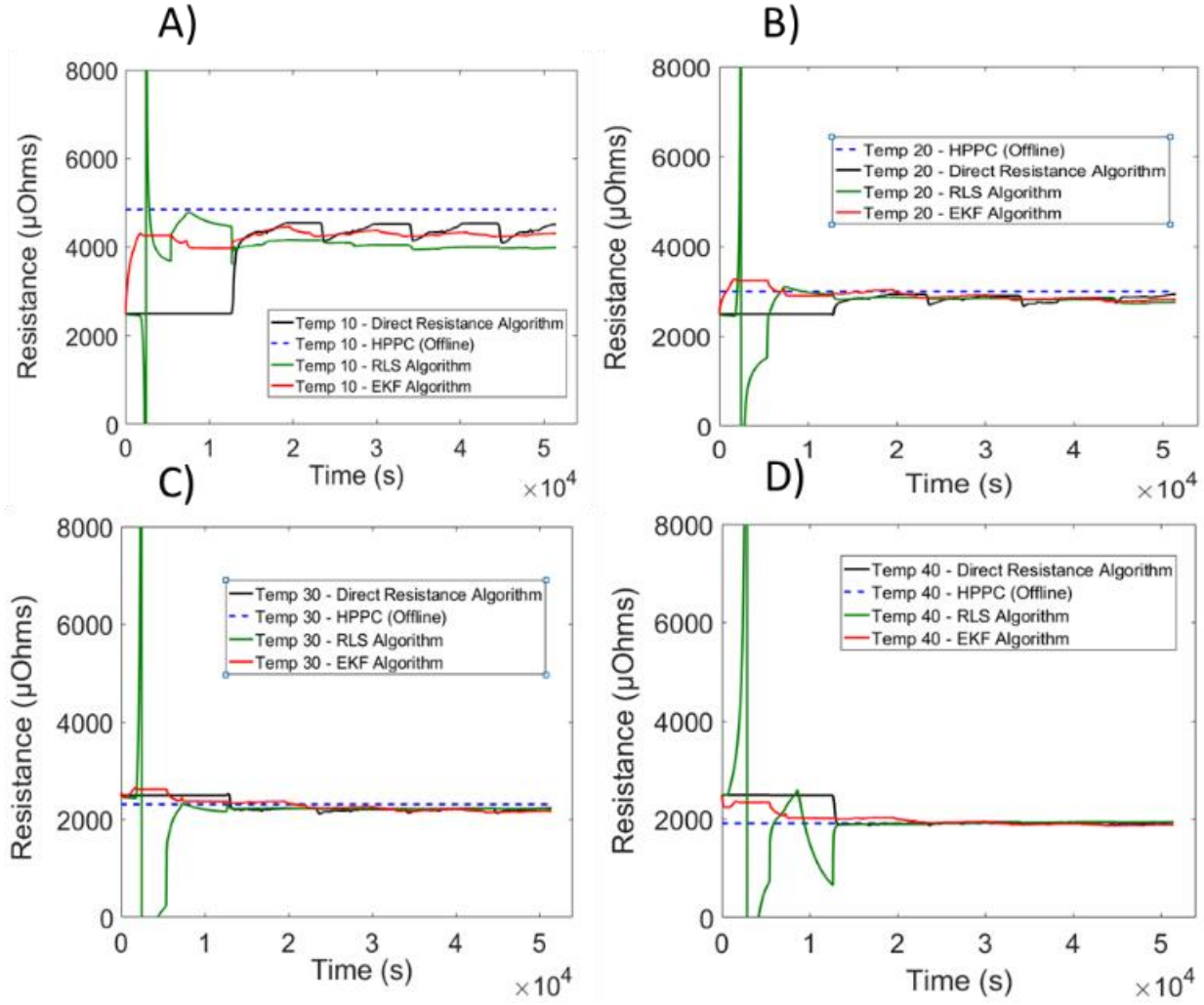

Figure 4-7: Resistance estimations from HPPC test, EKF algorithm, RLS algorithm and DRE algorithm for cell #1 (fresh cell) at temperatures of 10°C (A), 20°C (B), 30°C (C) and 40°C (D).

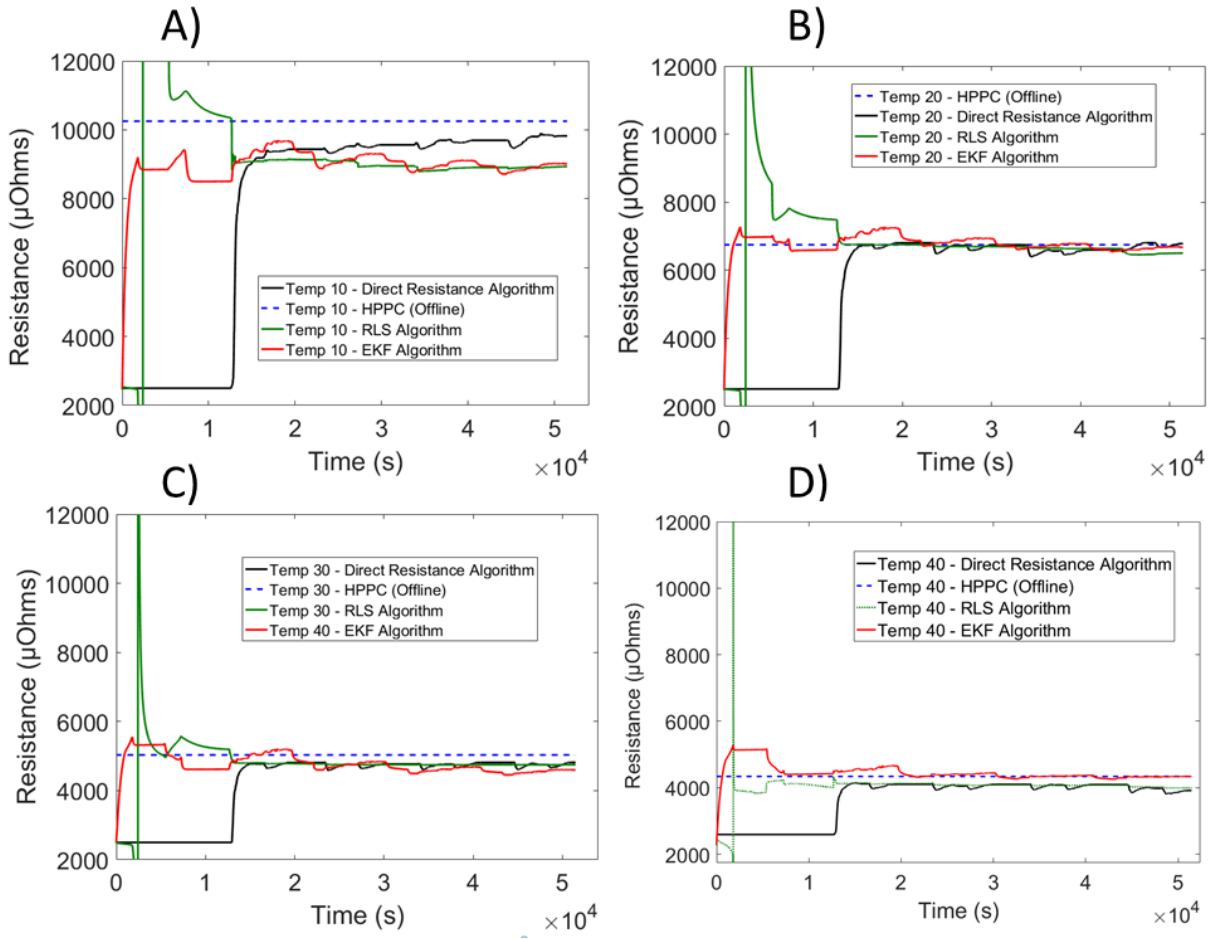

Figure 4-8: Resistance estimations from HPPC test, EKF algorithm, RLS algorithm and DRE algorithm for cell #2 (aged cell) at temperatures of 10°C (A), 20°C (B), 30°C (C) and 40°C (D).

Once again, there is strong agreement between the HPPC results and the output resistance estimates from all three algorithms. Given an initial guess of 2500 µOhms, all three algorithms were able to adapt to the actual battery resistance at different temperatures. This is true for both the fresh (Figure 4-7) and aged (Figure 4-8) cells. These trends are further confirmed when examining the mean percent error of the three different approaches (Table 4-5). The mean percent error is less than 10% at all temperature except for 10°C. Therefore, it can be concluded that the DRE algorithm, where only the ohmic resistance is estimated, can accurately track changes in resistance at different ambient temperatures.

Table 4-5: Comparison of the averaged percent error from DRA algorithm, RLS algorithm and EKF algorithm for fresh and aged cell at temperatures of 10 °C, 20 °C, 30 °C and 40 °C.

		RLS Error (%)	EKF Error (%)	DRE Error (%)
Fresh Cell	10 °C	16.95	11.51	9.06
	20 °C	6.21	5.11	5.04
	30 °C	3.90	4.48	4.80
	40 °C	0.73	1.38	0.87
Aged Cell	10 °C	12.63	11.89	6.32
	20 °C	1.66	1.39	1.58
	30 °C	5.56	7.76	5.60
	40 °C	6.22	0.81	7.05

It should be noted that the error at the lowest temperature of 10 °C is significantly higher than at any other temperature. Examining Figure 4-7 A. and Figure 4-8 A., it is evident that the resistance estimates from all three algorithms are smaller than the HPPC result. To better understand this trend, it is important to examine the conditions under which the HPPC test is carried out. For this particular test, the battery is initially at rest, and the temperature of the battery is in equilibrium with the ambient temperature. The online estimation techniques, however, are estimating the internal resistance of the battery under operation. Heat generated from the applied current could result in a higher battery internal temperature and therefore, a lower resistance estimate. This effect would be more prevalent at low temperature since resistance increases exponentially as the temperature is lowered [104].

Another observation from Figure 4-7 and Figure 4-8 A as well as Table 4-5 is that at low temperatures, there is a significant amount of variation in the resistance estimates. As the temperature increases, the resistance output becomes significantly smoother. One possible reason for this is that at lower temperatures, there can be differences in the battery internal resistance

depending on the battery SOC. Therefore, for SOH calculations, it is advisable to estimate the battery resistance at a higher temperature, where a more stable output is observed.

Finally, it is important to compare the computational complexity of each of these three algorithms. One approach is to express the required execution time in big O notation, which provides an upper bound to the running time of the algorithm. The EKF and RLS algorithms both have matrix calculations that are dependent on the number of states or parameters that will be estimated. Suppose that N represents the number of states/parameters to be determined. Then, it can be shown that the EKF has a computational complexity of $O(N^3)$ [132], whereas the RLS algorithm has a complexity of $O(N^2)$[133]. The DRE approach, however, has a lower complexity of $O(1)$. Therefore, in conclusion, the results from this study indicate that the DRE algorithm can provide accurate results, while requiring significantly less computational resources.

4.5 Conclusions

Three different approaches for estimating the internal resistance of the battery have been presented in this paper. The proposed DRE approach searches the current profile for sharp pulses in the current and voltage. An EWMA filter is then applied to obtain a smooth resistance output. The findings from this approach are compared with the results from more advanced estimation techniques such as the EKF and RLS techniques.

To test these three algorithms, a battery pack composed of four LFP cells connected in series were utilized. The pack was made of two new cells combined with two cells with a significant amount of degradation. The battery pack was then subjected to a carefully designed current profile.

The conclusions from this study are as follows:

1. All three algorithms were able to converge from an incorrect initial guess to the actual internal battery resistance, given by the HPPC test. This is true at different temperatures and different battery SOH.
2. The DRE technique can estimate the cell's ohmic resistance with the same amount of accuracy as the more advanced online estimation techniques. Therefore, utilization of this algorithm on a BMS can significantly reduce the computational cost. This can be extremely beneficial for a battery pack composed of hundreds of cells.

3. The DRE technique is only able to estimate the resistance when sufficient excitation is present in the current profile. Under operating conditions where the current does not change for long periods of time (i.e., constant current regions), the EKF or RLS approach should be used.
4. Comparison of the three techniques shows that the EKF has the fastest convergence to the true resistance value.
5. A more stable resistance output is obtained at a higher temperature for all three algorithms. These results seem to indicate that it might be advantageous to use resistance estimates at a higher temperature when evaluating SOH.

As previously mentioned, when considering the type of SOH estimation algorithm to use, it is important to consider the trade-off between simplicity and accuracy. The findings from this study will provide valuable knowledge on which algorithm is most the appropriate for a particular application.

Chapter 5: State-of-Health Estimation Algorithm for Lithium-Ion Battery Packs

The following chapter is based on the paper by Manoj Mathew, Stefan Janhunen, and Michael Fowler to be submitted to *Journal of Power Sources* (JPS) entitled: **"Determination of State-of-Health Using Direct Resistance Estimation with Filtering Based on Temperature and State-of-Charge".** Submission will occur after provisional patent is filed.

The author's specific contribution was in developing the SOH model and algorithms, conducting all experiments, carrying out the simulations, preparing the results, graphs and manuscript. Stefan Janhunen and Michael Fowler offered guidance on the research.

5.1 Introduction

Chapter 4 proposed an efficient algorithm for estimating battery resistance when there are constraints on computational resources. The next step is accurately converting these raw resistances estimate into a stable state-of-health (SOH) value. Before developing the algorithms, it is important to clearly define what is mean by SOH. Unfortunately, there is a great deal of ambiguity in literature on how the SOH of the battery is defined [70], [134], [135]. In general, a fresh battery is given an SOH rating of 100%, while a battery that has reached its end of life (EOL) has a SOH value of 0%. The limits at which the battery is said to have reached its EOL is left to the user. Therefore, the definition of SOH is normally tailored to a particular application for which the battery is being used. For example, in various stationary applications, the prediction of available power is essential for proper control of the battery pack and therefore the EOL for the battery is based on an increase in battery resistance[35], [136]. The EOL resistance, referred to as R_{EOL} for the rest of this work, is the maximum acceptable resistance in the battery. Based on this definition, the SOH rating will be defined as:

$$SOH_{Res} = \left(\frac{R_{EOL} - R_{SOH}}{R_{EOL} - R_{fresh}}\right) * 100 \qquad (5\text{-}1)$$

where SOH_{Res} represents the SOH value, R_{fresh} represents the resistance of a new battery and R_{SOH} is the current resistance of the battery. The EOL resistance, represented by R_{EOL}, can be based on

the power requirements for the application, where the EOL is defined as the point when the battery is no longer able to provide the necessary power.

For applications in electric vehicles (EV), the amount of available energy is important and thus capacity fade is the metric often used for calculation SOH [128], [61] . Given that an SOH rating of 0% represents a cell that has reached its EOL, the following equation can be used to quantify battery degradation on capacity.

$$SOH_{Cap} = \left(\frac{C_{EOL} - C_{SOH}}{C_{EOL} - C_{fresh}} \right) * 100 \quad (5\text{-}2)$$

where, SOH_{cap} represents the SOH value based on capacity, C_{SOH} is the current capacity of the battery, C_{fresh} is the battery capacity of a fresh cell and C_{EOL} is the capacity value at which battery is no longer usable. The EOL for an EV battery pack is normally defined as when the maximum capacity fades to 80% of its nominal maximum capacity [137]. One approach is to determine the overall battery SOH using the equation below:

$$SOH = min\left(SOH_{Cap}, SOH_{Res}\right) \quad (5\text{-}3)$$

Therefore, the depending on the application, either capacity or resistance can be the metric of choice for determining SOH. With regards to online capacity estimation, a number of approaches have been proposed in literature for determining $\mathrm{SOH_{cap}}$[61], [60], [138]. However, a number of practical considerations still needs to be addressed when estimating SOH_{res}. Therefore, the focus of this chapter will be on using resistance estimates to determine a stable SOH_{res} metric.

As the battery is cycled, side reactions occur at the electrode/electrolyte interface, forming the solid-electrolyte interface (SEI) layer [43], [47]. Formation and growth of this passive film increases the battery impedance over time. Therefore, resistance is a key metric that must be accurately estimated in order to monitor the battery SOH, especially in applications where available power is an important consideration.

As mentioned in Chapter 4, there are a large number of publications that explores various techniques for estimating the internal resistance of the battery [118], [139], [140] , [34], [122]. More research is required, however, in turning these resistances values into a stable SOH metric. A number of practical issues must be considered when determining SOH on the BMS.

1. Outliers can be present in the raw resistance estimates due to timing mismatch in voltage and current sensors. Removal of these outliers is essential in obtaining an accurate SOH value.
2. Noise in the resistance estimates, must be properly filtered before being used for SOH calculations.
3. The temperature and state-of-charge (SOC) dependence must be taken into account before determining SOH. Otherwise, the SOH value can change depending on the battery application.

The goal of Chapter 5 is to develop a robust SOH algorithm that properly addresses the three issues described above. The direct resistance estimation (DRE) approach, proposed in Chapter 4, will be to generate the resistance values. Unlike Chapter 4, where all the results were obtained in simulation, this proposed SOH algorithm will be implemented on Nuvation's BMS. In addition, the feasibility of using the DRE approach for frequency regulation type applications will be accessed.

5.2 Experimental

5.2.1 Experimental Set-up

Experimental data was obtained using the battery test station described in Section 4.2.3. In addition, three different battery chemistries were used in this study as summarized in Table 5-1 below.

Table 5-1: Manufacturer specifications for the batteries tested

Parameter	Value		
Cathode Chemistry	lithium cobalt oxide (LCO)	lithium iron phosphate (LFP)	lithium iron phosphate (LFP)
Type of Cell	Cylindrical	Cylindrical	Pouch
Nominal Capacity (Ah)	42.4	1.50	19.4

Rated Voltage Range (V)	2.75 – 4.20	2.00 – 3.65	2.00 – 3.65
Measured Initial Resistance (μOhms)	3230	85600	2550

The initial resistance was determined for all chemistries by applying a hybrid pulse power characterization (HPPC) test to a fresh battery and the values are summarized in Table 5-1. It should be noted that the resistance values listed in Table 5-1 refer to the ohmic resistance of the battery.

The operation of the test station involves selection of a current profile to be applied to the battery. The current profile was written as a text file and a Python script was used to communicate to the load box and power supply. The communication to the load box and power supply occurs at a frequency of 1 Hz, while the battery voltage, current and temperature were recorded from the BMS at a frequency of 2 Hz. The following section will explore the different current profiles that will be used to test the SOH algorithm.

5.2.2 Current Test Profile

The results from Chapter 4 revealed that accurate resistance estimates can be obtained using the DRE approach, given that there was sufficient current excitation. For example, applications where the current profile is in the form of a square wave is ideal since these profiles have significant changes in current and voltage. However, current profiles that are composed only of square waves are not typically seen in real world applications. To test the robustness of the algorithm under various applications, three carefully designed current profiles were utilized. The following section will provide a brief overview of each of these profiles. It should be noted that the applied current will be given in C-rates and therefore, can be easily scaled to different capacities.

5.2.2.1 Drive Cycle

The battery SOH is an important parameter that needs to be estimated in an electric or hybrid electric vehicle. Therefore, the algorithm was validated by running three commonly used drive cycles: Urban Dynamometer Driving Schedule (UDDS), Highway Fuel Economy Test (HWFET) and US06[141]. The current profiles are obtained using the same procedure as described in 4.2.4 and they are summarized once again in the figures below.

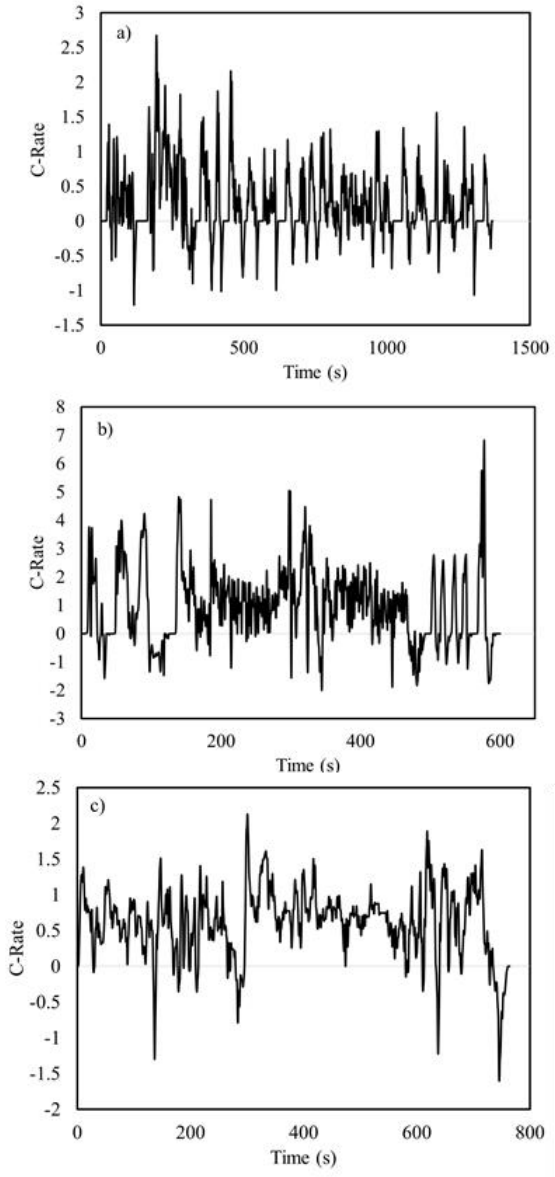

Figure 5-1: Current profile for the (a) UDDS drive cycle (b) US 06 drive cycle (c) HYFET drive cycle.

5.2.2.2 Frequency regulation profile

Depending on the type of application, the current transients experienced by the battery pack can be significantly different. For instance, the drive cycles described above contain rapid changes in current due to periods of braking and accelerating. Frequency regulation applications, on the other hand, do not always have the same degree of rapid current fluctuations. Therefore, in regards to grid storage applications, it is important to understand whether there is enough excitation in the current profile to accurately estimate resistance.

To simulate the typical current profile that a battery would experience in a frequency regulation setting, a sample regulation signal was taken from the PJM website. PJM is a regional transmission organization (RTO) in northeastern United States that "coordinates the movement of wholesale electricity" to 13 states in the US. A regulation signal that is frequently encountered in energy storage applications, referred to as a RegD signal [142], was used in this chapter. The data obtained from the PJM website is a normalized profile, which can be converted to a current profile for a particular battery configuration. The current profile that a battery would experience during a typical frequency regulation application is shown in Figure 5-2.

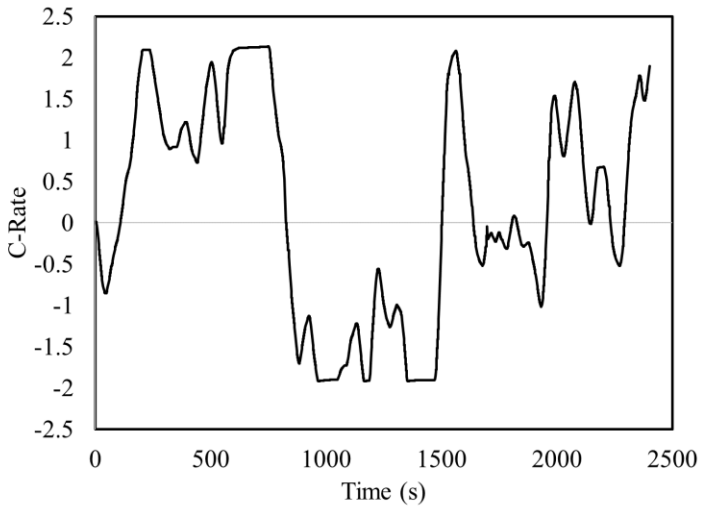

Figure 5-2: Current profile for the RegD frequency regulation cycle

Examining Figure 5-2, it is evident that the rate of change of the regulation signal is small, resulting in a gradual charging or discharging of the battery. Therefore, the Li-ion battery pack will be subjected to a frequency regulation type current profile to determine whether there is sufficient excitation in the profile for accurate resistance estimation.

5.2.2.3 Hybrid Pulse Power Characterization Test

The HPPC test is often used to parameterize various equivalent circuit models (ECM) such as the Rint and Thevenin models [108]. It consists of a 10 second discharge at 1C, followed by a 40 second rest period and 10 second charge at ¾ C. The current is summarized in Figure 5-3.

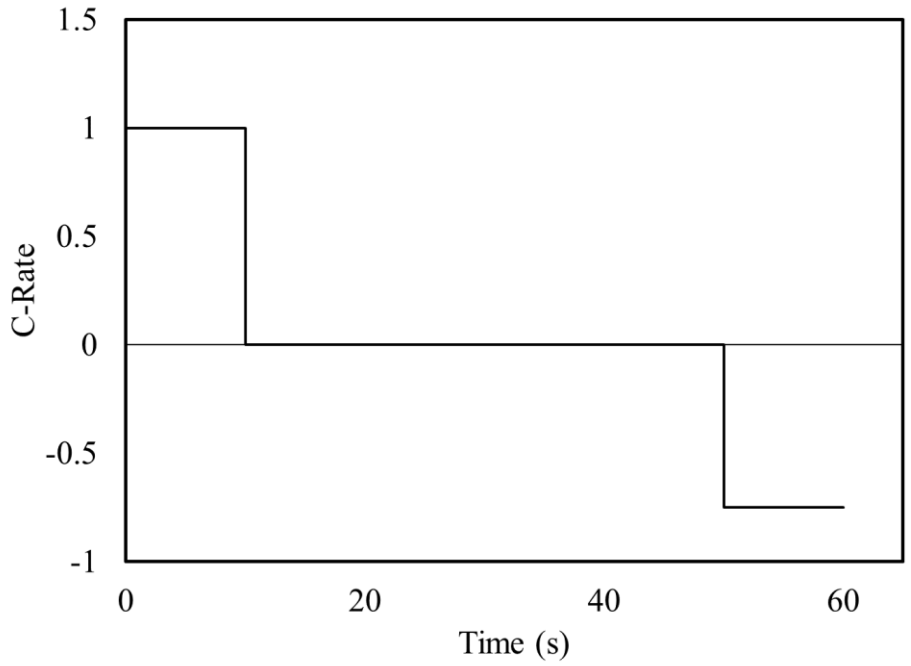

Figure 5-3: Current profile for the HPPC test.

The HPPC test will be incorporated in the testing current profile in order to obtain an accurate estimate of the ohmic resistance. The voltage drop as the current changes from zero A to 20 A discharge provides a sharp edge where the ohmic resistance can be estimated using Ohms law. As the battery ages, this test will be used to track the changes in the resistance and the value will be compared against the resistance estimates from the proposed algorithm.

5.3 Algorithm Development

The proposed SOH algorithm consists of three parts. First, the DRE technique will be used to generate resistance estimates online. Recall that the DRE algorithm examines the current profile for rapid changes in current and voltage and estimates the ohmic resistance when this change is observed. The ohmic resistance is updated based on Equation (5-4).

$$R_{ohm} = \frac{(U_{L,t} - U_{L,t+\Delta t})}{(I_{L,t} - I_{L,t+\Delta t})} \tag{5-4}$$

These estimates will then be filtered to remove outliers and noise. Finally, an efficient windowing approach will be utilized to remove the dependence of temperature and SOC on the resistance values. Since the DRE method was explored in the previous chapter, the following section will

only develop the outlier and noise removal algorithms along with the technique for eliminating temperature and SOC dependence on resistance.

5.3.1 Removal of Outliers and Measurement Noise in Resistance Estimates

Although the DRE technique is advantageous with respect to computational efficiency, the approach is sensitive to variations in sensor timing as well as measurement noise. To illustrate the issue of outliers, consider the following test. The DRE method was successfully implemented on Nuvation BMS and incorporated within the experimental setup described in Section 5.2.1. Lithium cobalt oxide (LCO) chemistry was used for this particular test, and the battery was subjected to a square wave current profile, where a discharge current of 40 A was applied for five seconds and brought to zero for the next five seconds. This profile was carried out for over 30,000 seconds and the BMS output resistance is summarized in Figure 5-4.

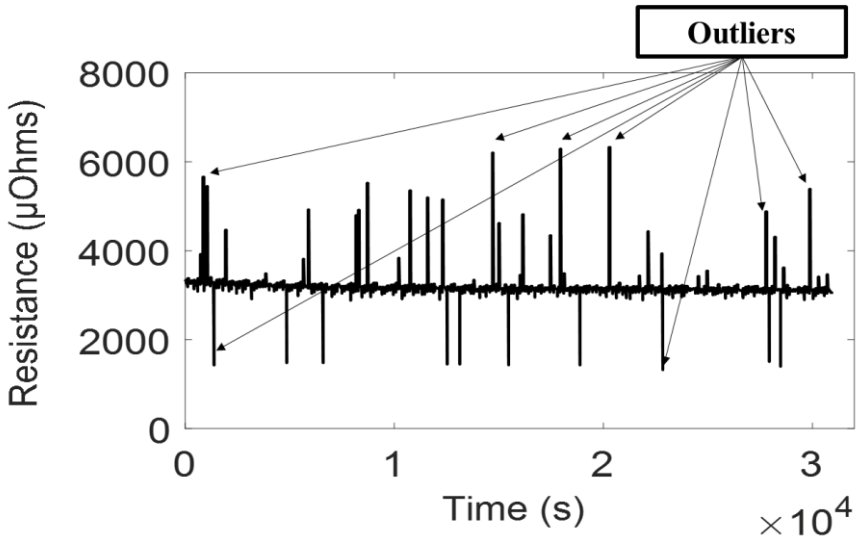

Figure 5-4: Outliers in the BMS resistance estimates for LCO, subjected to a square wave current profile.

Examining Figure 5-4, it is evident that numerous outliers are present in the BMS output since the nominal cell resistance of the battery is 3200 μOhms. To better understand the cause of these outliers, the following experiment was conducted: The LCO battery that was being discharged at 20 A was suddenly subjected to 20 A of charge. Voltage and current measurements were recorded for six seconds at a frequency of 10Hz (or 10 times per second), and the results are shown in Figure 5-5.

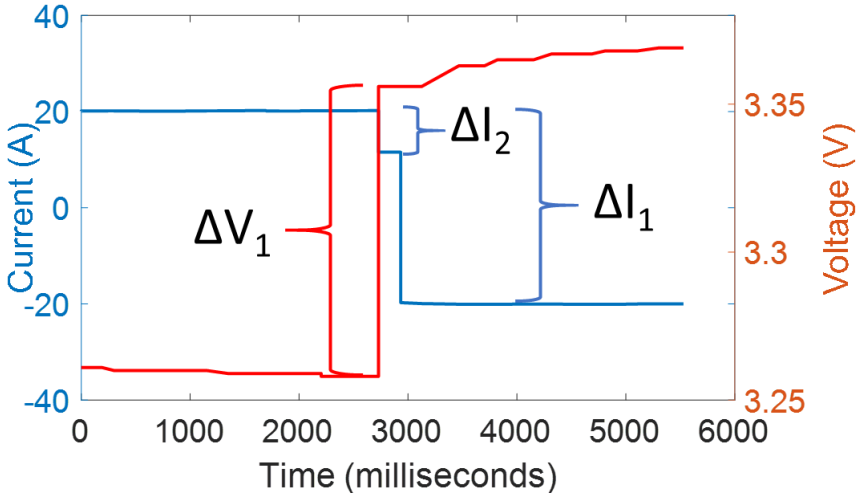

Figure 5-5: Voltage and current measurements as the current is switched from 20 A of discharge to 20 A of charge.

Examining Figure 5-5, it can be seen that as the battery goes from 20 A of discharge to 20 A of charge, an intermediate current value (represented by ΔI_2) is observed. This value is an artifact of the experimental setup and occurs due to a mismatch in the timing of the voltage and current sensors. Using ΔI_2 in Equation (5-4) would produce an erroneous resistance estimate. Although the outliers seen in Figure 5-5 are a result of the experimental setup used in this study, it is still important to address potential measurement issues for practical real-world application. The goal of this work is to develop a SOH algorithm that can be used in a wide range of conditions and is robust to measurement noise and outliers.

One approach to removing these outliers is to use a control chart approach, where resistance estimates that fall above or below a certain threshold limit are rejected. The upper and lower threshold limits can be determined using the following equation:

$$UL = \bar{X} + \sigma \text{ and } LL = \bar{X} - \sigma \tag{5-5}$$

where *UL* and *LL* represent the upper and lower limits respectively and σ represents the deviation from the mean. In a process control chart, the random variable is assumed to be Gaussian and the deviation is usually taken to be *3*Standard Deviation* at 99% confidence. In this chapter, the value of σ will be another configurable parameter that can be tuned for a particular battery chemistry or

application. This approach is illustrated in Figure 5-6 A), where the nominal resistance is used as the mean $\bar{X}$ and the σ is set to 500 µOhms.

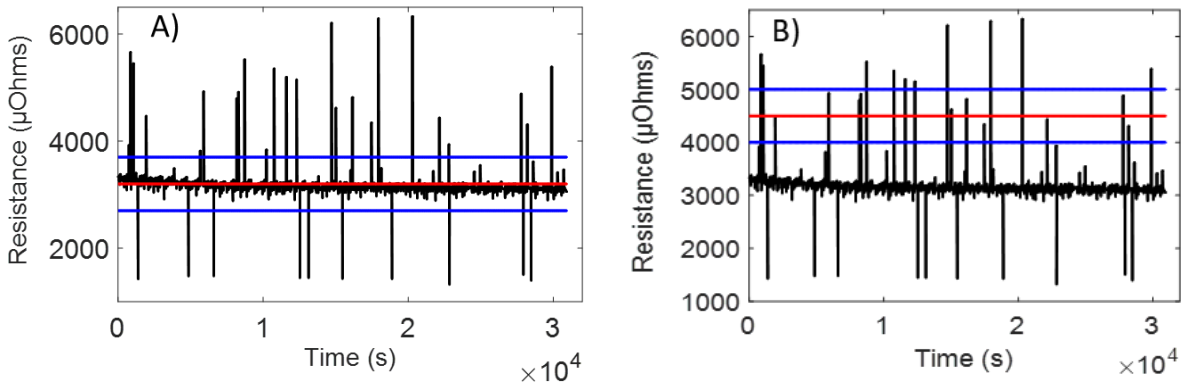

Figure 5-6: (A) Control chart approach using the correct mean value and a standard deviation (σ) of 500 µOhms (B) Control chart approach using an incorrect mean value of 4500 µOhms and a standard deviation (σ) of 500 µOhms.

There are two disadvantages in using the nominal resistance value as the mean in Equation (5-5). First, if the initial guess of the nominal resistance is incorrect, then all resistance values might end up being rejected. This is illustrated in Figure 5-6 B), where the actual resistance is around 3200 µOhms but the nominal resistance used in removing outliers was set to 4500 µOhms. Therefore, all the values below 4000 µOhms will be incorrectly rejected. Second, the internal resistance of Li-ion batteries is influenced by temperature and therefore it can increase or decrease depending on the operating conditions. Having fixed bounds on the estimates is not advantageous since the upper and lower limits would not be able to account for the temperature effect.

To resolve these issues, the following approach (Figure 5-7), is proposed for removing outliers and filtering measurement noise.

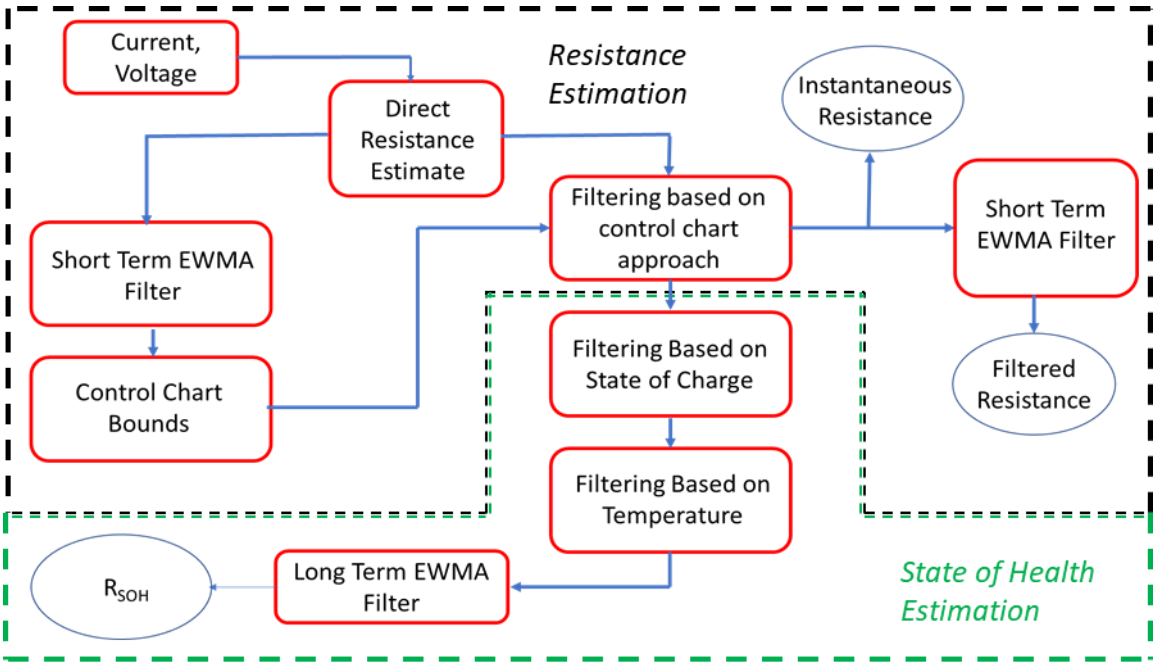

Figure 5-7: Flowchart of the proposed algorithm for removing outliers and filtering measurement noise.

Consider the left hand-side of the resistance estimation section (enclosed by black dashed line) shown in Figure 5-7. The algorithm starts by generating resistance estimates when a significant change in current and voltage is observed by the BMS. Then an exponentially weighted moving average (EWMA) filter, initially introduced in Section 4.3.1, is used for estimating the mean value $R_{CL,k}$, used in determining the upper and lower bounds.

$$R_{CL,k} = \left(1 - \lambda_{EWMA,CL}\right) * R_{CL,k-1} + \left(\lambda_{EWMA,CL}\right) R_{ohm,k} \qquad (5\text{-}6)$$

where, $R_{ohm,k}$ is the resistance obtained using Ohms law, R_{CL} is filtered resistance value used to determine the control chart limits and $\lambda_{EWMA,CL}$ is the forgetting factor. Recall that a larger $\lambda_{EWMA,CL}$ value means more smoothing of the output. Using this approach, the upper and lower limits of the control chart can then be defined as follows:

$$UL = R_{CL,k} + \sigma \text{ and } LL = R_{CL,k} - \sigma \qquad (5\text{-}7)$$

where UL represents the upper limit, LL represents the lower limit and σ is a factor that can be tuned for a particular application. If the user has a high degree of confidence in the resistance measurements, a smaller value of σ can be used.

Using this approach, the upper and lower limits of the control chart change with the operating conditions of the battery. The value of $R_{CL,k}$ is determined using ***all*** the resistance estimates, including resistance values that might be outliers. This allows the algorithm to adapt to changes in battery operating conditions as well as to correct for any errors in the initial guess.

Before moving on to SOH estimation, it is important to first define the two terms that will be used throughout the chapter for describing the algorithm results. The resistance estimates obtained after removal of outliers will be referred to as instantaneous resistance and is shown in Figure 5-7. Measurement noise will cause a significant amount of variability in the instantaneous resistance estimates and therefore, a second EWMA filter will be used to smooth out the resistance trend as shown below.

$$R_{filtered,k} = (1 - \lambda_{EWMA}) * R_{filtered,k-1} + (\lambda_{EWMA}) R_{inst,k} \qquad (5\text{-}8)$$

The output from this moving average will be referred to as filtered resistance and is illustrated in Figure 5-7. This value can be used to monitor the change in resistance as the surface temperature of the battery changes but it will not be used in SOH calculations.

5.3.2 Filtering based on temperature and state-of-charge

To develop an SOH algorithm, the resistance values need to be converted into a SOH metric between 100% and 0%. As previously mentioned, there is no clear consensus in literature on how the SOH of a battery should be defined. However, there are a few important variables that needs to be addressed before building an accurate SOH algorithm.

First, it should be noted that the resistance estimates are dependent on the temperature and battery SOC [118], [143]. Estimating the resistance at low temperature versus high temperature can give significantly different results, and comparison of these results to nominal resistance values can result in erroneous SOH predictions. Therefore, the operating condition of the battery needs to be accounted for in the SOH calculations. This work proposes a windowing approach to account for fluctuations in temperature and SOC as the battery is cycled. The complete SOH algorithm, is shown in Figure 5-7 (enclosed by a green dashed line).

After the removal of outliers using the adaptive control chart, the resistance values are passed through an SOC filter. The filter removes all estimates obtained when the SOC is below 20% or

above 80% because the resistance is usually higher in this SOC region. [144]. In addition, the resistance is passed through a temperature filter, where resistance values are selectively removed based on the operating temperature of the battery. The range of the temperature window was taken to be around 2°C in order to remove the effect of temperature on resistance. For example, if the temperature window is taken to be between 25 °C and 27 °C, only resistance estimates obtained when the battery surface temperature lies in this range is used for SOH calculations. This approach represents a simple and efficient way to remove temperature dependence on resistance and thereby produce an SOH metric that is stable under various battery conditions.

Finally, the EWMA filter will be employed to reduce variance in the resistance estimates. The value of the tunable constant $\lambda_{EWMA,\mathrm{LT}}$ is taken to be an order of magnitude higher when compared to the value used in determining the filtered resistance. The value of R_{SOH} obtained from this approach can be substituted into Equation (5-1) to determine the SOH value.

5.4 Results and Discussion

To ensure the algorithm is able to provide reliable resistance estimates, testing was carried out using the battery station discussed in Section 5.2.1. It should be noted that the resistance estimation block in Figure 5-7 was implemented on Nuvation BMS and the instantaneous and filtered resistance values reported in this work are obtained from the BMS output.

5.4.1 Internal Resistance Estimation

Validation of the proposed algorithm requires a current profile that is representative of current draws experienced by the battery pack in both automotive and stationary applications. Therefore, this test vector consists of the drive cycles, described in Section 5.2.2.1, along with two frequency regulation cycles and an HPPC test. The complete test is shown in Figure 5-8 below.

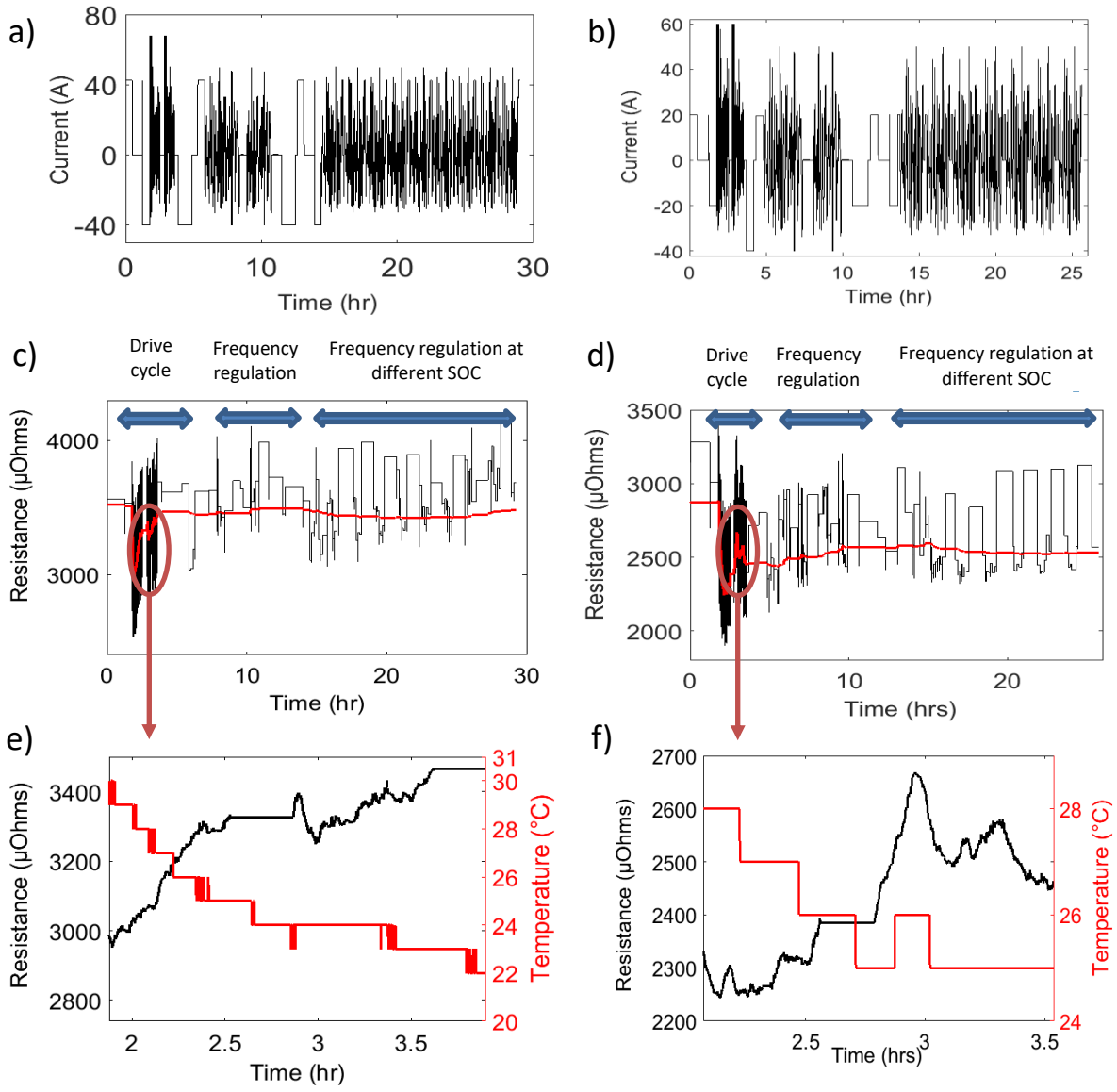

Figure 5-8: (a-b) The current profile applied to LFP and LCO battery chemistry for validation of the battery's internal resistance (c-d) The obtained instantaneous and filtered resistance values for LFP and LCO battery chemistry (e-f) Filtered resistance as the temperature of the battery changes for LFP and LCO.

The profile starts with three consecutive drive cycles including HWFET, UDDS and US06 cycles. The battery is then brought to 50% SOC and a frequency regulation type profile is applied. Next the battery is discharged to 50% and an HPPC test is conducted. Finally, another frequency regulation profile is used, where the battery is fully discharged from 100% SOC to 0% SOC.

The current profile shown in Figure 5-8 (a) was first applied to LCO chemistry and the temperature, current, voltage and resistance values were sampled at a frequency of 2 Hz. It should be noted that the maximum charge/discharge C-rate for the LCO cell was 1.5 C and therefore, the profile was scaled to meet this requirement. The time window, minimum current threshold and minimum voltage threshold for the DRE method were taken to be 1 s, 2 A and 0.007 V respectively. The deviation for the upper and lower limits in Equation (5-7), denoted by σ, was taken to be 500 μOhms and the results are shown in Figure 5-8 (c)

The black solid line in Figure 5-8 (c) represents the instantaneous resistance estimates obtained under different current profiles. Examining Figure 5-8 (c), it is clear that a significant number of resistance estimates can be obtained during the drive cycle portion of the profile. This number decreases, however, as the battery moves to the frequency regulation sections. This is to be expected as this section of the current profile contains only gradual changes in current and voltage. It is important to note that, although fewer resistance estimates were determined, there was still enough excitation in the frequency regulation profile to produce a stable resistance output.

The red dashed line in Figure 5-8 (c) is the filtered resistance estimates obtained after passing the resistance values through an EWMA filter with a $\lambda_{EWMA,ST}$ value of 0.01. Application of the filter was found to substantially reduce the variance that was present in the instantaneous resistance estimates. Figure 5-8 (c) also shows a large swing in the filtered resistance value when the drive cycle starts. To better understand this trend, Figure 5-8 (e) shows an enlarged portion of the above graph with temperature plotted on the right y-axis. It can be seen that the increase in resistance pertains to a decrease in the temperature of the battery. This result is encouraging as it confirms the ability of the algorithm to estimate the resistance of the battery under various operating conditions.

In order to check the validity of the proposed algorithm for different battery chemistries, the battery was switched from LCO to LFP. The cell parameters are shown in Table 5-1, and the same current profile applied to LCO was applied to the LFP cell (Figure 5-8 (b)). For this particular battery, the time window, minimum current threshold and minimum voltage threshold were set to 1 s, 3 A and 0.006 V respectively. Since the resistance values are similar in magnitude for the two cells, the same standard deviation was used for the control chart bounds. The LFP cell results are shown in Figure 5-8 (d).

Comparison of Figure 5-8 (c) and Figure 5-8 (d) shows that a similar trend is attained for both battery chemistries. The algorithm is able to adequately remove outliers and filter out measurement noise for the LFP battery. In addition, Figure 5-8 (e) illustrates that the filtered resistance value is able to adapt to changes in temperature. Therefore, the proposed algorithm can be used to estimate the resistance of different Li-ion batteries, without the need for a chemistry specific OCV curve or individual battery model parameters.

The number of times the resistance was estimated, for a particular section of the current profile, can be determined and is summarized in Table 5-2. The drive cycle section is composed of three individual drive cycles (US 06, UDDS and HWFET) while the frequency regulation section has two different profiles. Profile 1 in Table 5-2 refers to the RegD type frequency regulation profile while Profile 2 is the small part of the RegD profile carried out from 100% to 0% SOC.

Table 5-2: Number of resistance estimates obtained for LFP and LCO battery under different current profiles

		Time (hr)	LFP Resistance Estimates per hour	LCO Resistance Estimates per hour
Drive	**US 06**	0.333	4218	4314
	UDDS	0.761	1495	1640
	HWFET	0.424	1970	1668
Frequency	**Profile 1**	5.095	16	15
	Profile 2	11.834	9	10

The results from Table 5-2 show that the drive cycles provide a significantly larger number of resistance estimates in comparison to the frequency regulation cycles. In regards to each specific drive cycle, the US06 profile provides the most resistance estimates. This is not surprising as examination of the US06 profile indicates that it is a highly aggressive drive cycle, where the current changes rapidly in a matter of seconds. The frequency regulation cycles, on the other hand,

produces a significantly lower number of estimates since the current gradually changes over time. For example, LFP pouch cell estimates the resistance 16 and 9 times per hour for profile 1 and 2 respectively. Although the estimates are generated at a much lower rate, it should be noted that the resistance of a battery changes in a matter of weeks if not months. Therefore, continuous cycling of the battery for days will provide sufficient estimates for accurate SOH estimation.

Another important factor that needs to be considered when evaluating the effectiveness of the algorithm is the influence of an incorrect initial guess. To ensure that the algorithm converges to a correct resistance value, an incorrect resistance value was assumed. The current profile shown in Figure 5-8 (a-b) was applied and the results are summarized in below.

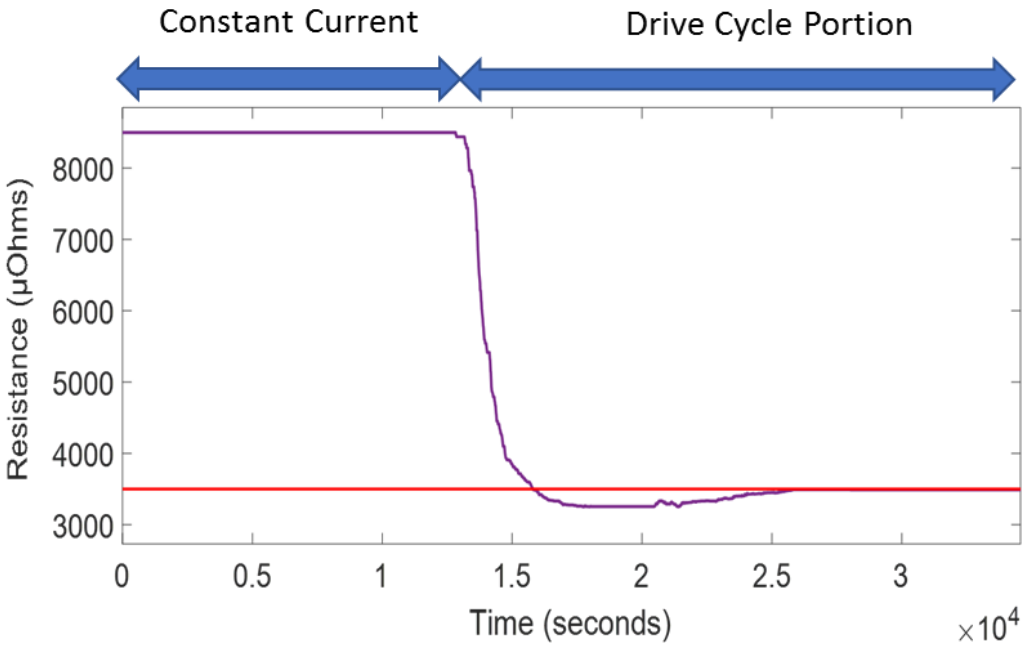

Figure 5-9: Estimation of the internal resistance of the battery when an incorrect resistance value of 8500 µOhms is initially assumed.

From Figure 5-9, it is evident that the internal resistance of the battery, based on the filtered resistance estimates, quickly converges to the correct value after less than an hour of operation. During the first few minutes, the resistance remained at 8500 µOhms as the algorithm was not able to converge to the correct value due to the lack of resistance estimates. Examining the current profile in Figure 5-9, the beginning portion of the profile consists a of constant current section that would not present enough variation in voltage and current to obtain any resistance estimate. The

resistance starts to converge once the drive cycle profile begins since this particular section consists of rapid changes in current and voltage.

Finally, the algorithm was used to estimate the resistance of 320 cells in a high voltage battery stack. Cylindrical LFP cells, summarized in Table 5-1, were used in this study. A constant current charge/discharge cycle was applied to the cells for one day and the final filtered resistance value was recorded at the end of the test. Resistance estimates were made by the algorithm during the switching portions of the test. The filtered resistance values for the 320 cells are summarized in the histogram below.

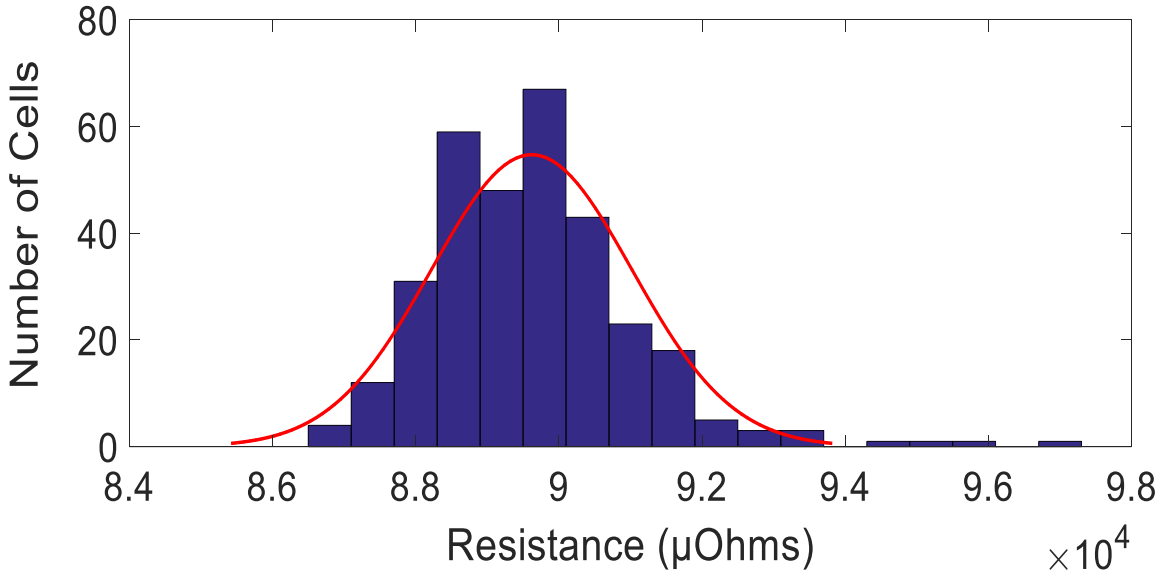

Figure 5-10: The histogram of the filtered resistance measurements of 320 cells from the high voltage battery pack.

Figure 5-10 shows a distribution of cells that have been aged over time. Since the nominal resistance of a fresh LFP cell is 86500 μOhms in this case, it is evident that the majority of cells have increased in resistance due to cycling. It also appears that there are a few cells above 94000 μOhms. These cells will limit the power capability of the battery pack and therefore might require replacement. The results from this study indicate that the algorithm can be used to identify cells that deviate from the average and these cells can be considered for replacement in the battery pack.

In summary, the results so far have shown that the proposed resistance estimation algorithm is robust in the presence of outliers, under different temperature and incorrect initial guesses. In addition, it is simple and efficient enough to be implemented on a BMS that may be required to manage hundreds of cells.

5.4.2 State-of-Health Estimation

The goal of SOH estimation is to accurately track the degradation of the Li-ion battery until it reaches a point where it can no longer be used effectively. In this paper, internal resistance estimates will be used to provide an estimate of how much the battery has aged over time. Since resistance is correlated with the battery operating temperature and SOC, the algorithm will examine the effects of filtering out these two variables.

The current profile shown in Figure 5-8 (a-b) was applied continuously for a total of 27 days. The LCO cell was used for this particular test and the voltage, current, temperature and resistance readings were sampled at a frequency of 2 Hz by the BMS. The full testing profile for validation of the algorithm is shown in Figure 5-11 (a).

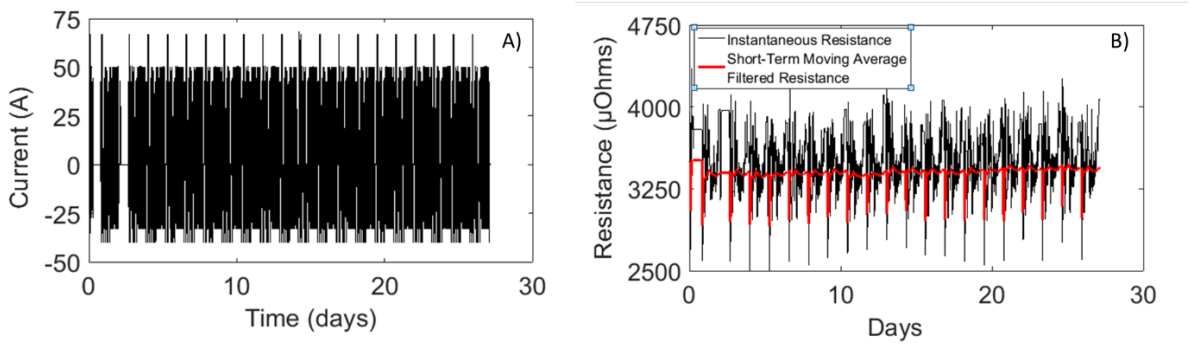

Figure 5-11: (a) The long-duration current profile used in testing the lithium cobalt oxide battery (b) The instantaneous and filtered battery resistance values obtained for the current profile

The resistance algorithm was used to calculate the instantaneous and filtered resistance estimates over a period of 27 days. The resistance estimates are summarized in Figure 5-11 (b). Once again, the sharp drop and rise in the filtered resistance is due to changes in the surface temperature of the battery as it moves from one current profile to a less demanding profile. It should be noted that the trend that was detected in Figure 5-8 (c-d) is also present in Figure 5-11 (b) after a full 27 days of cycling. Since the filtered resistance estimates vary with temperature

and SOC, using this value for calculation of SOH will not yield accurate results. To produce a stable metric for tracking battery SOH, the resistance measurements were filtered based on the battery operating temperature and SOC. Only resistance estimates obtained when the battery was between 20% to 80% SOC will be used. In addition, only resistance values estimated when the battery temperature fell in the range of 25 °C to 27°C were considered.

Once again, the EWMA filter was used to smooth out the noise, only this time, a $\lambda_{EWMA,LT}$ value of 0.001 was used. The SOH was calculated using Equation (5-1), where the resistance of a fresh cell was taken to be 3230 µOhms and the R_{EOL} was taken to be 6600 µOhms. The value of R_{SOH} and battery SOH is presented in Figure 5-11 A and B.

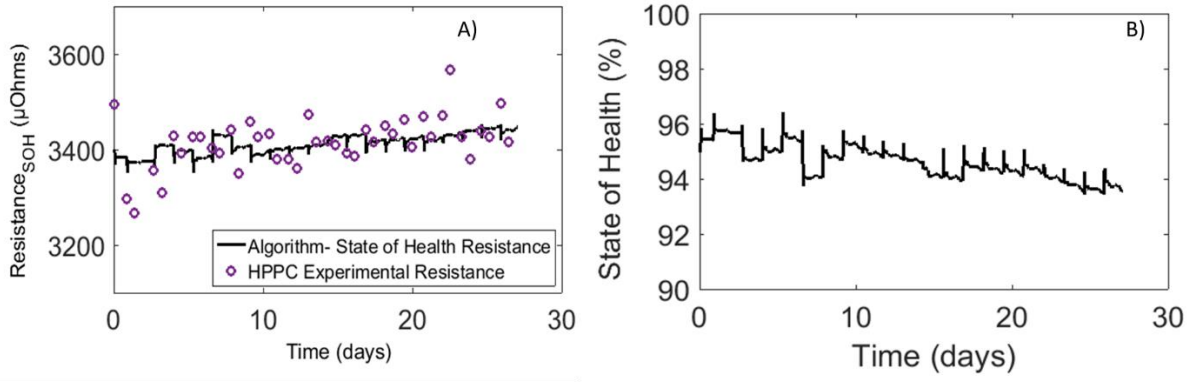

Figure 5-12: (A) resistance used in calculating SOH for the LCO battery (B) The battery SOH rating over 27 days.

Figure 5-12 B shows that the SOH resistance values are stable when temperature and SOC effects are removed. The HPPC experiments, described in Section 2.2.1 can be used to provide an estimate of the experimental battery resistance, and is depicted as purple dots in Figure 5-11 B. Comparison of resistance results from the algorithm to the experimental HPPC values gives a mean error of 1.1% and a maximum error of 3.8%. Therefore, it can be concluded that the algorithm is able to accurately estimate the resistance of the battery over an extended period of time.

5.5 Conclusions

This paper proposes a SOH estimation approach. Any outliers present in the resistance estimates were removed using an adaptive control chart technique. This method was found to give accurate resistance estimates under different operating conditions and showed quick convergence to the nominal resistance when an incorrect initial guess was used. Since a simple resistance model is

assumed, the computational cost of this method is significantly less when compared to adaptive filtering algorithms that are frequently cited in literature. Therefore, it can be easily scaled to operate on a large battery pack without demanding large amounts of memory or computational resources.

To obtain an SOH metric, the internal resistance was filtered using temperature and SOC, and the resulting values were passed through a long term EWMA filter. The results show a very stable resistance estimate with an average error of 1.1 % when compared to HPPC data over 27 days. Stable resistance values are essential for robust SOH estimation, specifically one that does not dependent on temperature or battery SOC. In addition, the algorithm was used to estimate the distribution of resistances in a large pack of 320 cells illustrating how the algorithm proposed in this work can be utilized to successfully track the degradation of individual cells in a large Li-Ion battery pack.

Chapter 6: State-of-Charge Estimation Algorithm for Lithium-Ion Battery Packs

6.1 Introduction

Accurate estimation of state-of-charge (SOC) is one of the most challenging areas in battery research. A number of factors, such as control strategies, balancing algorithms and safety constraints are dependent on the SOC value. Therefore, determination of this battery state is critical in developing a robust battery management system (BMS). The difficulty in SOC estimation arises from the fact that unlike a gasoline tank, where the fuel level can be measured, the charge remaining in the battery needs to be estimated. The estimation of SOC for a battery pack is complicated by measurement noise, model inaccuracies, battery degradation, and cell-to-cell variability. Although a high-fidelity model can be developed, there might be computational limitations in how complex the model can be. Therefore, accurately estimating SOC while maintaining a computationally efficient algorithm will be the central focus of this work.

As explored in literature review, a number of approaches have been proposed for SOC estimation at the cell level, from various adaptive filters to artificial neural networks and fuzzy logic algorithms. These approaches however, estimate the SOC for one individual cell in the battery pack. The cells in the battery pack rarely have similar characteristics; that is to say, the resistance and capacity values tend to differ within cells. This inconsistency means that the SOC for an individual cell in the battery pack can be significantly different from that of its neighbors. Therefore, estimation of SOC at the pack level is essential for safe and reliable control of the battery pack.

Although a large number of publications address the development of cell-level SOC estimation algorithms, limited research currently exists for SOC estimation at the pack level. The publications that do exist can be grouped into one of four categories.

1. The first group of approaches extends a single cell SOC algorithm and executes them on each cell in the battery pack. Chen et al. [145] proposes carrying out the extended Kalman filter (EKF) algorithm to calculate the SOC of each individual cell. The minimum and maximum SOC of the pack is then used to calculate the pack's SOC. Although this

approach can ensure accurate performance, implementation of the algorithm for each individual cell can become computationally expensive. This is especially true when more advanced filtering approaches are used, such as the particle filter (PF) and the sigma-point Kalman filter (SPKF). Therefore, application of these algorithms on a BMS is often infeasible.

2. The second group of methods utilize screening or filtering techniques to create a battery pack with cells having limited cell-to-cell variability. Research conducted by Kim et al. [146] shows that by selecting cells with similar electrochemical characteristics, a battery pack can be developed with cells of similar resistance and capacity. Estimation of SOC for this pack can be accomplished by using a lumped ECM model. Likewise, Xiong et al. [147] used filtering based on resistance and capacity to assemble battery modules with similar SOC values. However, there are two main limitations to the techniques described above. First, if the cells age at different rates, the uniform battery pack can become non-uniform over time. Second, BMS manufacturers may not have control over the assembly of the battery pack. The algorithm should be able to adapt to different pack topologies and chemistries.
3. Another common method is to determine the 'average SOC' first and then use the deviations between the averaged cell and the individual cell to determine the SOC for each cell. As an example, Plett [148] proposed a bar-delta filtering approach to estimate the SOC and SOH values of each cell in the battery pack. The work was extended by Dai et al. [149] who incorporated a dual time scale for estimating the average SOC and individual cell deviations. Although these approaches are advantageous in that they provide an estimate of the SOC for each individual cell, they can also be computationally expensive as it requires hundreds of delta filters running on the BMS.
4. The final approach, and one that is gaining traction recently, is pack level SOC estimation based on a select few cells. Hua et al. [150] proposed an approach for calculating pack SOC by determining the weakest cell in the pack and then using a nonlinear predictive filter on this cell to estimate SOC. Although this approach produced reliable results, it can only be applied to a pack with passive balance control. Zhong et al. [151], proposed an approach for an unbalanced pack, where the SOCs of two cells were related to the overall

pack SOC. However, this approach does not model the change in battery model parameters as the pack ages.

There are two gaps in pack SOC estimation literature that will be addressed with this work. First, the papers that have proposed an algorithm for an unbalanced pack, do not consider changes in cell model parameters. Whereas, the developed algorithms in literature that do take into account changes in model parameters, are not always applied to a battery pack that is unbalanced. A more in-depth analysis is required to understand how these algorithms behave for an unbalanced pack. Therefore, this research will develop a comprehensive pack-level SOC algorithm that will track the SOC of an unbalanced pack, while simultaneously estimating the model parameters online to ensure performance does not degrade over time.

The second contribution of this work is the development of an algorithm that behaves logically to the battery users. Since the EKF is a stochastic technique, the tracking behavior of SOC can behave erratically in certain situations. For example, when the battery is at rest, the EKF SOC estimate can appear to increase or decrease. This type of behavior is said to be "illogical" and can cause energy storage system (ESS) users to lose confidence in the accuracy of their BMS product. There is currently no work in literature that accounts for this effect. Therefore, this research proposes a novel adaptive coulomb counting component at the top level to ensure that the algorithm behaves logically.

6.2 Experimental Approach

6.2.1 Battery Test Stations

Two different test benches were constructed to carry out SOC estimation tests. The first test bench is the same one described in the experimental sections of Chapter 4 and 5 and is depicted in Figure 6-1 below. Since the test bench has been described in detail in previous chapters, only a brief description will be given in this section. The test bench can be used to provide a charging current up to 40 A and a discharging current up to 60 A. Since the capacity of all batteries used in this study fall between 15 Ah to 40 Ah, the given test bench can be utilized for validation of the proposed SOC estimation algorithm. The voltage, temperature and current will be sampled at a frequency of 1Hz and the current profile will be inputted into the load box and power supply at the same frequency. The above battery test station can only test a pack below 20V due to the voltage

limit on the power supply. Therefore, for testing of packs above 20V, a second test bench was constructed and is shown in Figure 6-2.

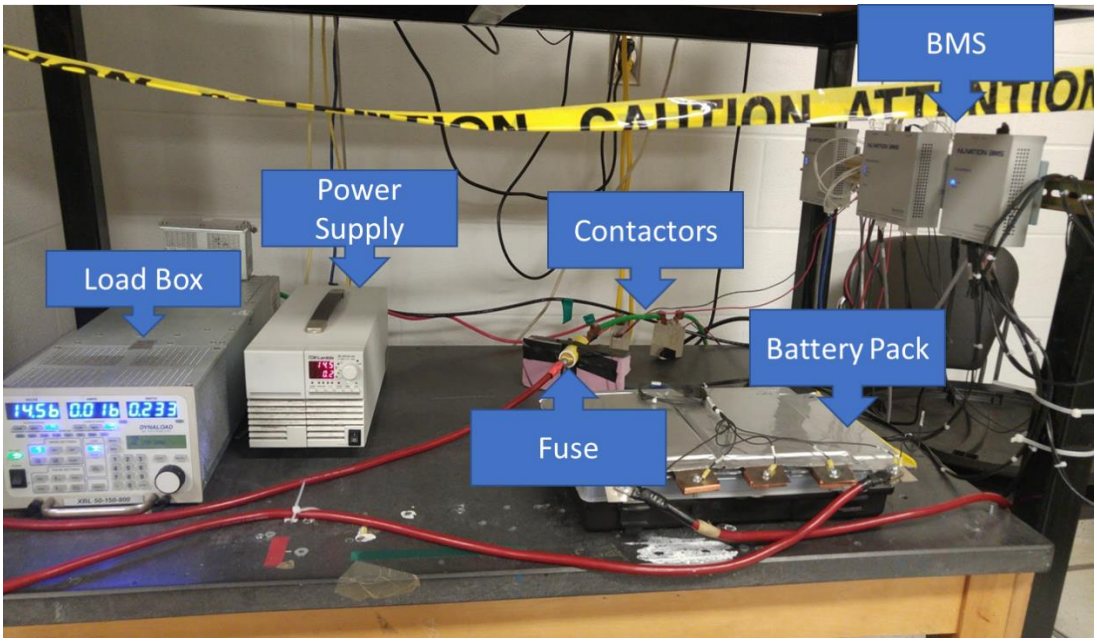

Figure 6-1: The first battery test station with an upper voltage and current limit of 20 V and 60 A respectively.

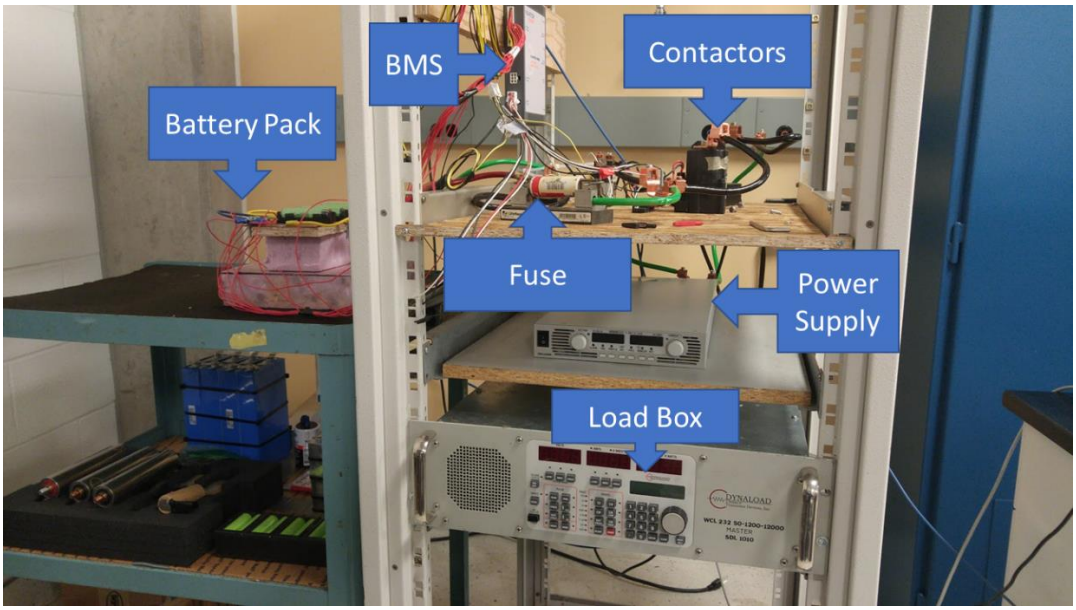

Figure 6-2: The battery test station with an upper voltage and current limit of 50 V and 12 A respectively.

The second test bench was constructed in a similar manner as the first. This battery test station will be used to test battery packs that have higher voltages but lower currents. For example, some of the future works on SOH/SOC estimation will be carried out using 12 18650 Li-Ion cells connected together in series. It should be noted that the test bench has an upper current limit of 12 A and therefore, the pouch cells cannot be tested using this set-up.

6.2.2 SOC Validation Benchmark

The challenge with algorithm validation is that the obtained results need to be compared to an accurate benchmark before any conclusions can be drawn regarding its accuracy. In this work, the "actual" SOC value will be obtained from coulomb counting. This might seem counter-intuitive since the goal of the research project is to improve on existing methods, such as coulomb counting. As previously stated, the two main drawbacks to coulomb counting is that 1) accumulation of an offset error can occur if the battery is not calibrated and 2) an initial SOC is required. To account for these errors, the following steps were taken. First, the initial SOC was obtained before the start of any test by charging the battery to full capacity. Second, to account for offset drift, the final SOC value after completion of the test was obtained. Using the initial and final SOCs, the offset drift was calculated and this value was incorporated into calculating percent error. By using this approach, an accurate SOC benchmark was established for evaluating algorithm performance under various operating conditions. All SOC estimates obtained using this approach will be referred to as *actual SOC estimates* for the rest of this section.

6.2.3 SOC Algorithm Validation Current Profiles

Testing algorithm accuracy requires careful selection of appropriate validation tests. Conducting battery experiments that stress the limits of the algorithm are essential in understanding the conditions where the proposed technique works and where it doesn't. To this end, five different current profiles were generated, each meant to test a particular aspect of SOC estimation. The following section will provide more details about the generated current profile, and the rationale for using it. It should be noted that the RegD profile, initially described in Section 5.2.2.2, is used for many of the validation tests.

6.2.3.1 SOC Current Drift - Validation Profile

This particular current profile was generated to determine the algorithm performance when a 25-mA offset in current is introduced. The current profile is shown in Figure 6-3.

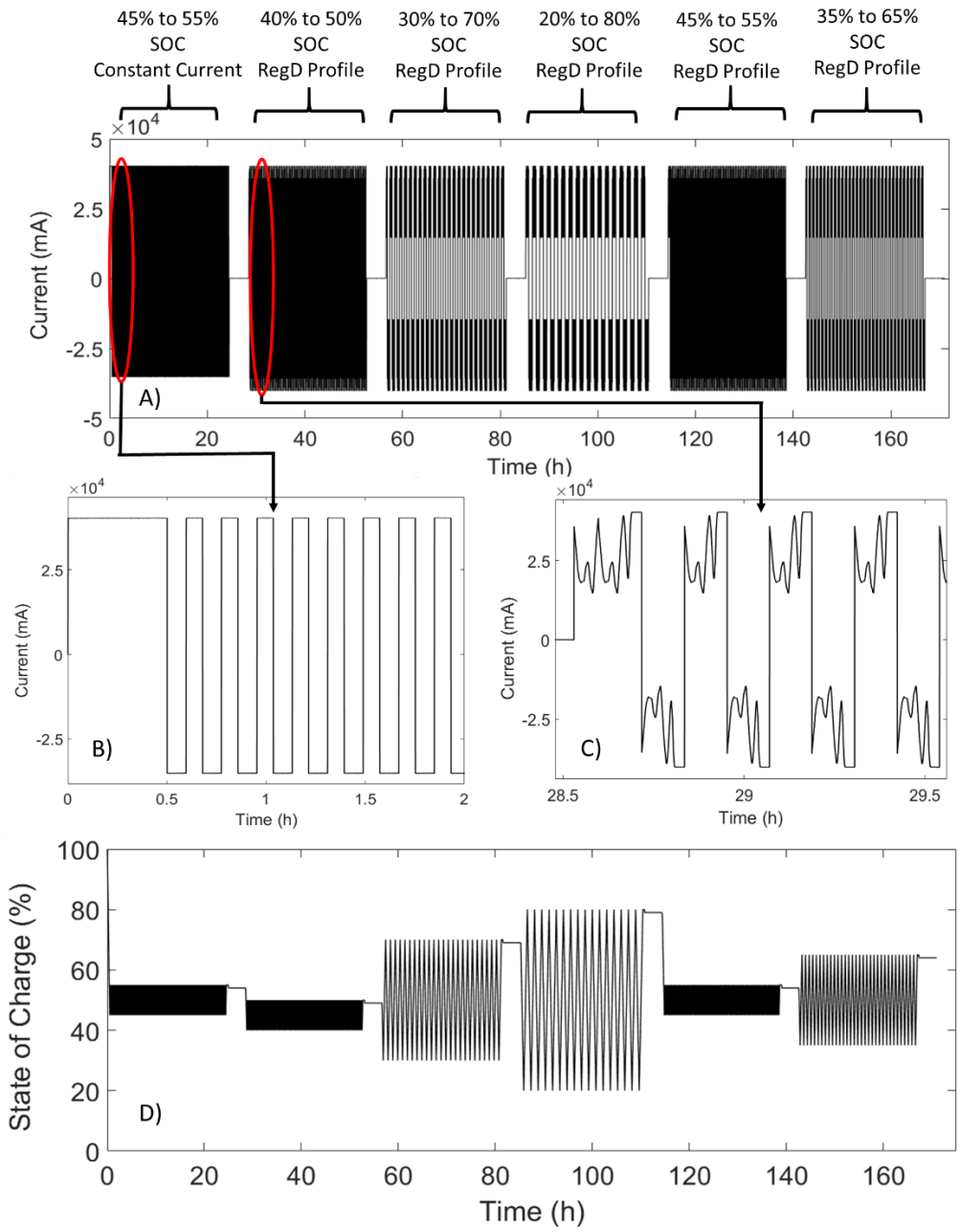

Figure 6-3: (A) The current profile used in evaluating algorithm performance when an offset error is present in the current measurements and (D) the corresponding SOC profile of the battery pack.

The validation test consists of the following steps:

1. The test begins with a constant-current constant-voltage (CCCV) charge to full and a three-hour rest to ensure that the battery has reached equilibrium.
2. Next, the battery is cycled for 24 hours at a constant current of 2C, between an SOC of 45% and 55%. This particular current profile is shown in Figure 6-3 B).
3. The battery is then allowed to rest for 2 hours and cycled once again between an SOC of 40% to 50%, only this time, a RegD profile was utilized (Figure 6-3 C).
4. After another 2-hour rest period, the battery is cycled between SOC regions of 30% to 70%, 20% to 80%, 45% to 55% and 35% to 65%, with subsequent 2-hour rests in between each SOC region. The final SOC profile for this test is shown in Figure 6-3 D).

The battery was exposed to various SOC swings and different current profiles to ensure that algorithm performance is not dependant on the battery SOC or current magnitude. The ultimate goal of this validation profile is to determine if the proposed algorithm can adequately remove offset errors present in the current measurements.

6.2.3.2 SOC Logical Behavior - Validation Profile

Before describing the validation profile, it is important to clearly define what is meant by SOC illogical behavior and why it is important to resolve this issue. A battery is said to behave illogically if one or more of the following events occur:

1. The battery is at rest but the SOC is increasing or decreasing
2. The battery is charging but the SOC is decreasing
3. The battery is discharging but the SOC is increasing
4. The SOC jumps rapidly between SOC points instead of smoothly transitioning between them. For example, the SOC changes from 20 % to10 % and back to 15 %.

A direct consequence of this type of illogical behavior is a loss in confidence of the SOC accuracy. A battery user that notices the SOC changing when the battery is at rest might question the reliability of the SOC algorithm. In addition, since the SOC represents the amount of energy remaining in the pack, random fluctuations in this value can lead to incorrect decisions at the system level. Therefore, developing an algorithm that can produce reliable SOC estimates, is essential.

The behavior described above is often observed for an LFP battery that is at rest between 40% and 60% SOC. The small gradient of the OCV-SOC curve, coupled with the hysteresis effect present in LFP cells, can lead to illogical behavior. Therefore, a current profile will be generated to evaluate algorithm performance under these operating conditions. The corresponding SOC profile is illustrated in Figure 6-4.

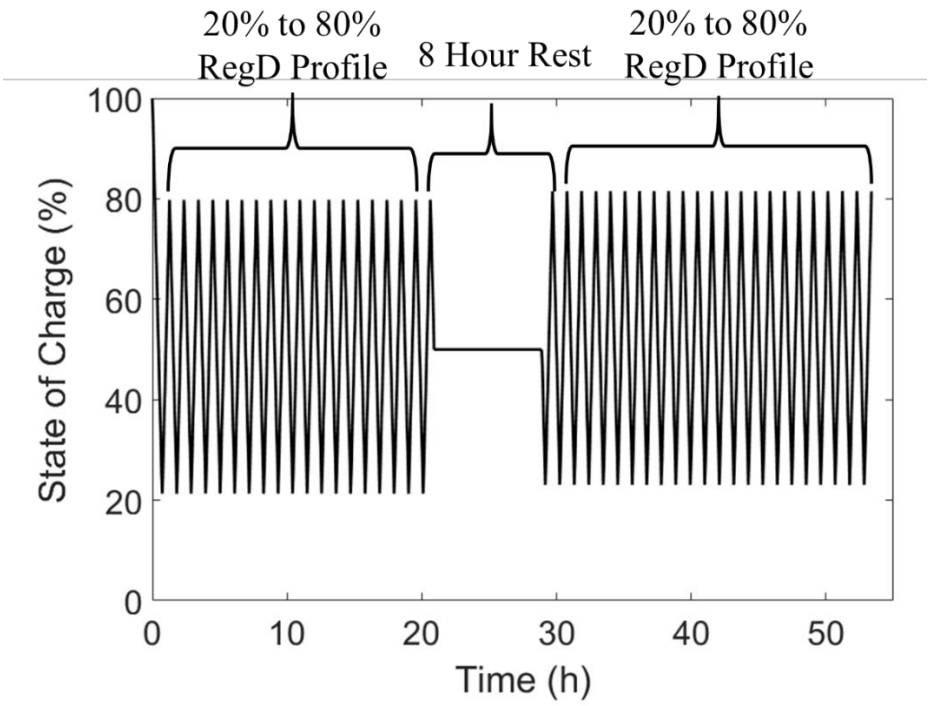

Figure 6-4: SOC profile for testing whether the algorithm SOC estimates behave logically.

The following current profile was used for testing whether or not the algorithm produces well-behaved SOC values.

1. The battery pack is initially charged to full and the battery is cycled between 20% and 80% SOC for 21 hours using the RegD current profile.
2. The applied current is then removed when the battery is at 50% SOC, and the battery pack is allowed to rest for 8 hours.
3. The current is re-applied and the battery pack is once again cycled between 20% and 80%.

The purpose of this test is to determine whether the algorithm behaves logically in the rest period, where accurate SOC estimation is extremely difficult.

6.2.3.3 *SOC End-Point Error - Validation Profile*

A large number of BMS decisions occur when the battery is almost full or close to empty. Therefore, accuracy at the upper and lower SOC regions is more important than accuracy in the middle SOC region. To test the performance of the algorithm at the upper and lower SOC regions, the following current profile was implemented.

1. First the battery is brought to full so that an initial estimate of SOC can be obtained.
2. The cell is then discharged to 50% SOC using a constant current of 1C.
3. The RegD profile is used to cycle the battery for 24 hours between 45% and 55%.
4. After 24 hours of cycling, the battery is brought to empty (Figure 6-5 A) or full (Figure 6-5 B) using a constant current of 1C.

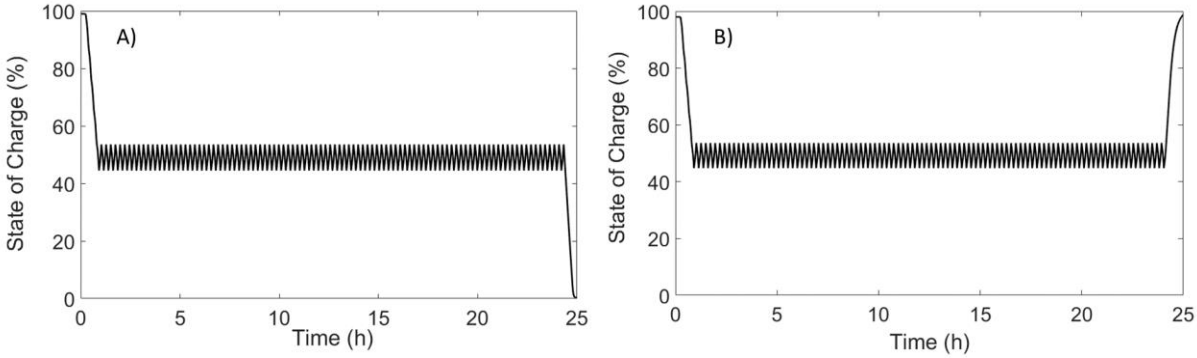

Figure 6-5: SOC profile for the end-point validation test, where the cell is brought to empty (A) or full (B) at the end of the test.

As previously mentioned, the largest SOC errors are observed in the flattest portions of the OCV curve. For LFP, this occurs between an SOC of 60% and 40%. Therefore, the goal of this test is to a). determine the worst case SOC error in this mid-SOC region and b). determine if the error is reduced as the battery is brought to empty or full. An SOC error of 10% may be acceptable for some BMS manufacturers at 50% but this same error at the lower and upper SOC regions will be much more problematic.

6.2.3.4 SOC Unbalanced Pack - Validation Profile

During the operation of a battery pack, individual cells within the pack can become unbalanced. This could occur for two reasons. First, if the battery pack does not have a balancing algorithm, the intrinsic variations within the batteries will led to some cells having a lower SOC than others. This can be problematic since the capacity of the battery is dependent on the weakest cell. In

situations where a balancing algorithm is present, the pack can still become unbalanced if the wrong cell is discharged. This can happen when balancing is based on the terminal voltage of the cell rather than its SOC. For example, consider two cells of the same SOC but different resistance. A larger resistance means the terminal voltage will be higher during charge, leading to the BMS discharging the cell when it should not. This can cause the battery pack to become unbalanced over time.

To test the algorithm performance for an unbalanced pack, the following two tests were carried out:

Test #1: Evaluate the performance of the algorithm when the battery pack is unbalanced and the BMS is not balancing.

1. All four cells within the pack are brought to an SOC of 50% using constant current discharge at 1C.
2. Two of the cells are discharged an additional 10% SOC.
3. The battery pack is then cycled from 95% SOC to 5% SOC for 24 hours.

The SOC profile for the *min* and *max* cell is shown in Figure 6-6. For the remainder of this paper, the *min* cell will refer to the cell that discharges to empty first, and the *max* will represent the cell that charges to full first.

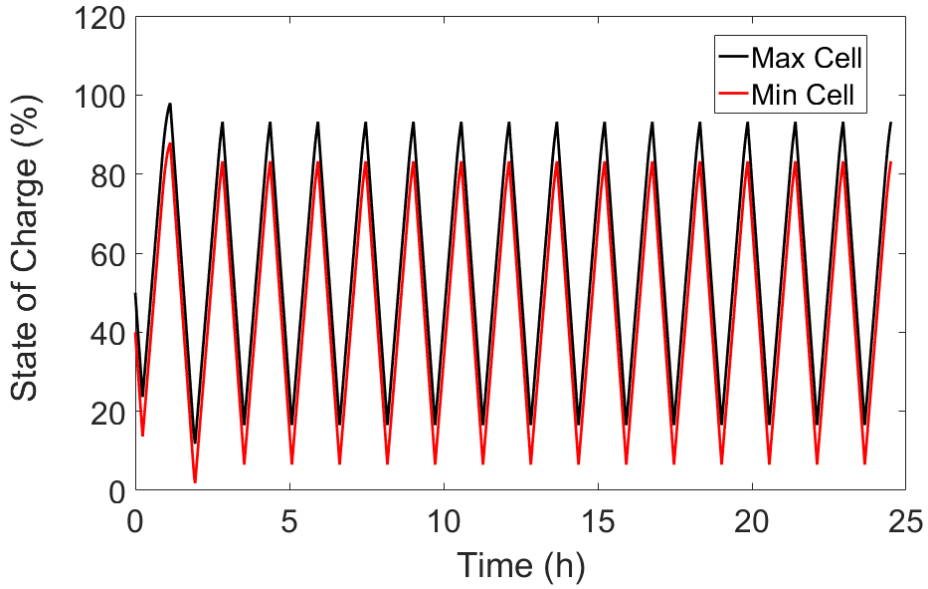

Figure 6-6: SOC profile for the *min* and *max* cell for an unbalanced pack.

The purpose of this test is twofold. First, the algorithm is tested to determine whether it can accurately determine the SOC of the *min* and *max* cell within the pack. Second, the goal is to evaluate the algorithm performance in predicting the pack SOC as the cell is brought to full and empty. The pack SOC should seamlessly transition from the *max* cell SOC when it is full to the *min* cell SOC when it is empty.

Test #2: Evaluate the performance of the algorithm when the battery pack is initially unbalanced but becomes balanced during battery cycling.

1. All four cells within the pack are brought to an SOC of 50% using constant current discharge at 1C
2. Two of the cells are discharged an additional 10% SOC.
3. The battery pack was then cycled for over two days following the SOC profile shown in Figure 6-7.

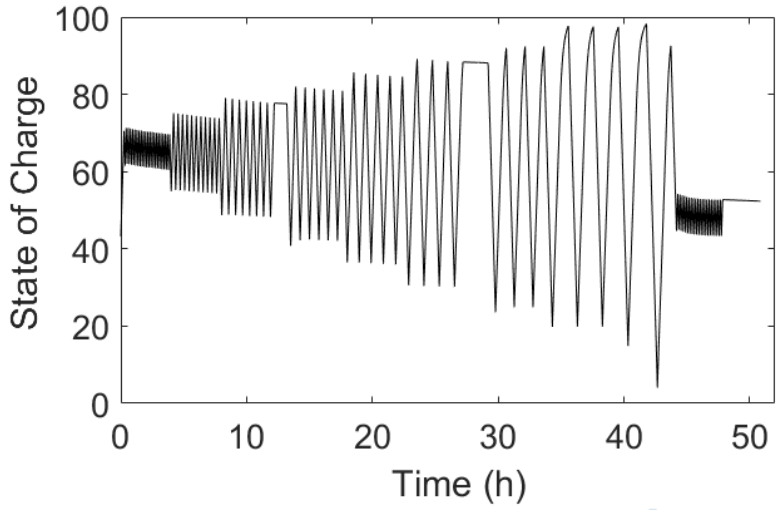

Figure 6-7: SOC profile for the battery pack that is initially unbalanced but becomes balanced as the battery is cycled.

The purpose of test #2 is to determine whether the algorithm can accurately track SOC while the battery pack transitions from being unbalanced to balanced.

6.3 Algorithm Development

The proposed SOC estimation algorithm will be composed of three distinct sub-algorithms: cell level SOC estimation, pack level SOC estimation, and adaptive coulomb counting. The input and output for each sub-component is illustrated in Figure 6-8.

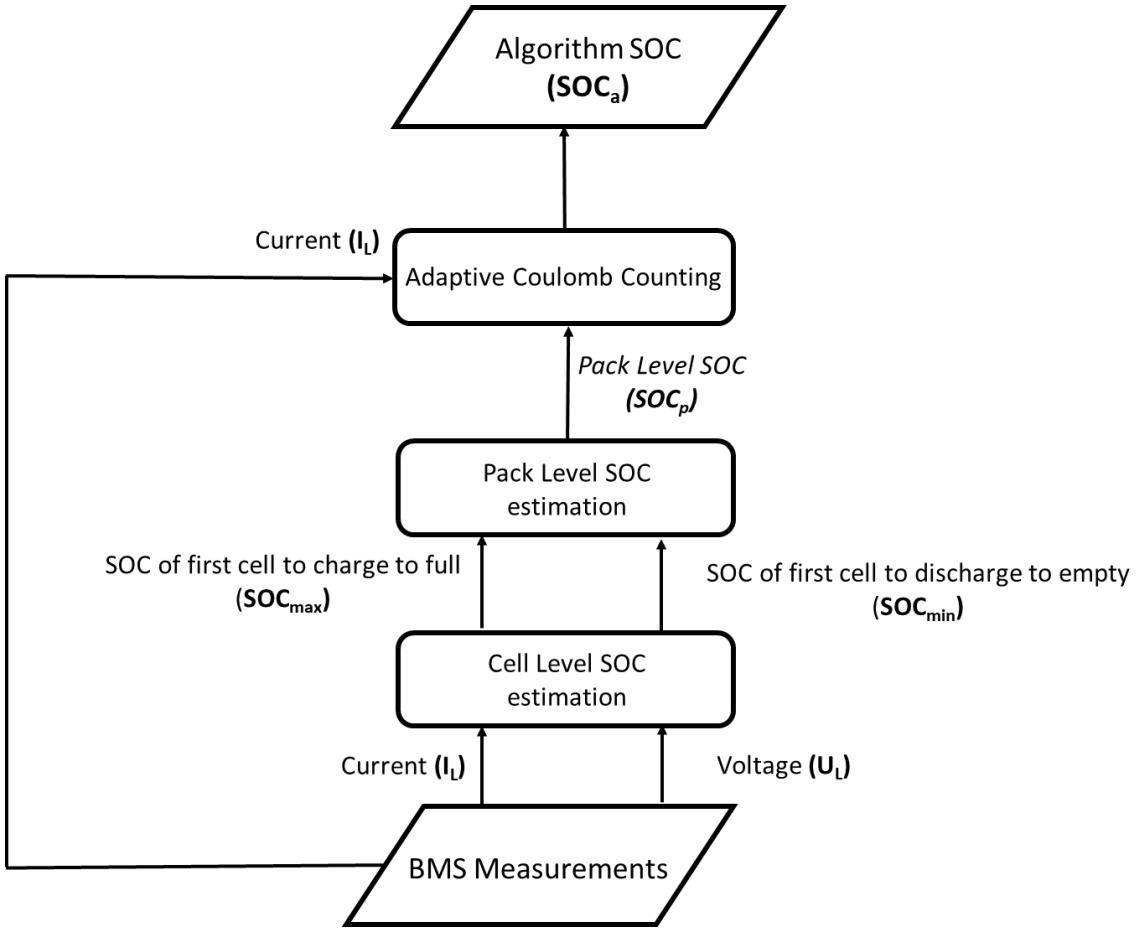

Figure 6-8: Overall SOC estimation algorithm for implementation in BMS.

It should be noted that there are minimal dependencies between the different modules, which permits one to make significant modification to a sub-algorithm without changing the other two components. In fact, SOC estimation at the cell level can be carried out using the wide array of techniques described in Section 2.4, without having to change the other two components. This allows for continuously iterative improvements in the future as more computational resources become available. The following section will develop the equations at each of the three levels and explain how each sub-algorithm relates to the overall SOC estimation framework.

6.3.1 Cell Level SOC Estimation

The SOC estimation step will be carried out in this work using an EKF, while the model parameters will be updated using the RLS approach. The battery states and model parameters for only two cells will be calculated in this work. By restricting the algorithm to a few select cells, the computational cost can be significantly reduced. Determination of these cells and the corresponding assumptions will be explored in greater detail in the pack level algorithm section. This section will develop the equations used for both estimating the SOC using EKF and updating the model parameters using RLS. The two algorithms and how they are coupled together are summarized Figure 6-9.

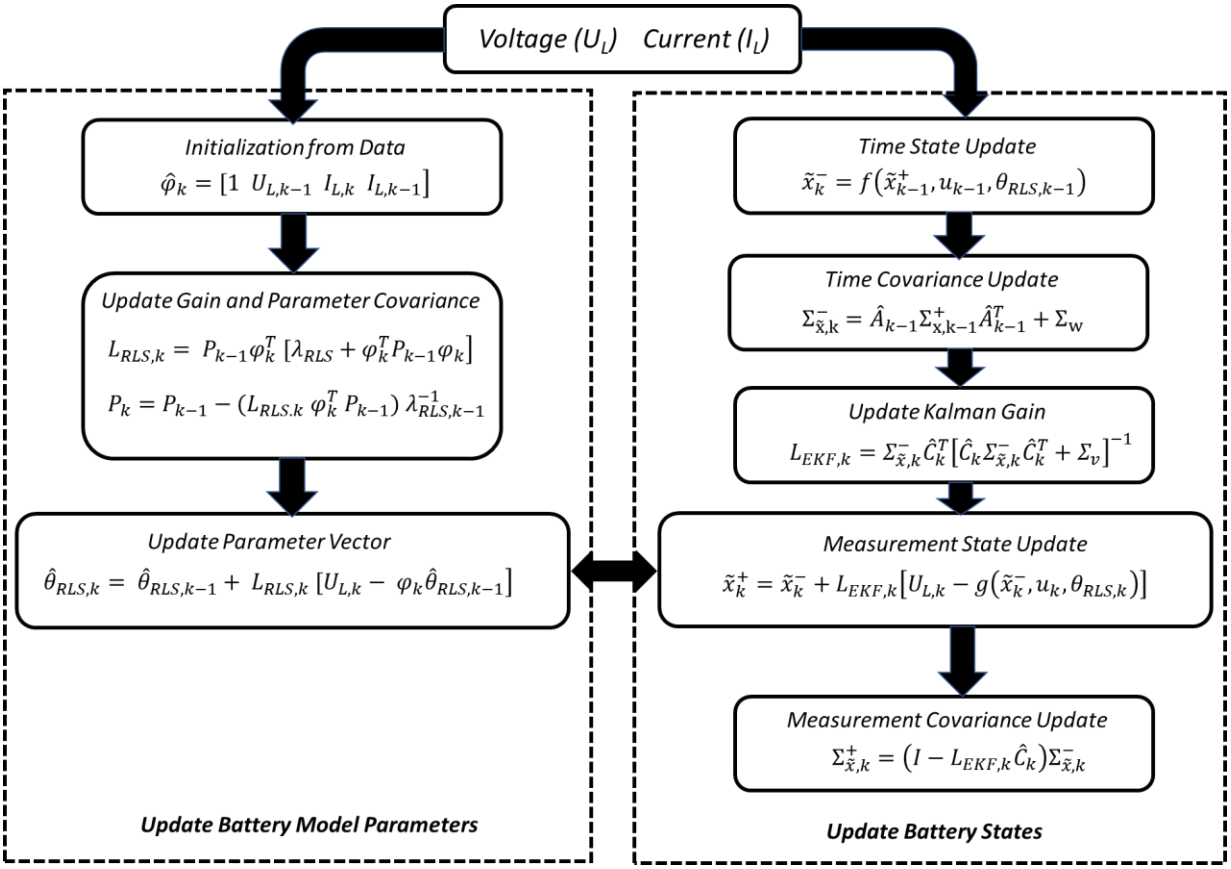

Figure 6-9: Cell-level SOC algorithm using EKF for state SOC estimation and RLS for model parameter estimation.

Before the RLS algorithm can be executed, the battery model needs to be written in the following form:

$$y_{RLS,k} = \theta_{RLS,k}\varphi_k + e_{RLS,k} \tag{6-1}$$

Where, $y_{RLS,k}$ represents the output terminal voltage to be estimated, $\theta_{RLS,k}$ is the parameter vector, φ_k is the exogenous inputs and $e_{RLS,k}$ is the measurement noise. To develop the model in the above form, the Thevenin battery model needs to be first written in the frequency domain as shown in Equation (6-2).

$$U_L(s) - U_{ocv}(s) = -I_L(s)\left(R_0 + \frac{R_1}{1 + R_1C_1s}\right) \tag{6-2}$$

Where, U_L is the battery terminal voltage, U_{ocv} is the battery open circuit voltage (OCV), I_L is the applied current and R_0, R_1 and C_1 are the battery parameters. It should be noted that s represents the Laplace domain and not the battery SOC. By defining $E_T = U_L - U_{ocv}$ and using a bilinear transformation ($s = 2z(-1)/T/(z+1)$), the following transfer function can be obtained in discrete time, with a sample time T_s.

$$\frac{E_T(z^{-1})}{I_L(z^{-1})} = -\frac{\frac{(R_0 + R_1 + 2R_0R_1C_1)}{1 + R_1C_1s} + \frac{(R_0 + R_1 - 2R_0R_1C_1)}{1 + R_1C_1s}z^{-1}}{1 + \frac{T_s - 2R_1C_1}{T_s + 2R_1C_1}z^{-1}} \tag{6-3}$$

The above equation can be written as:

$$E_{T,k} = a_1E_{T,k-1} + a_2I_{L,k} + a_3I_{L,k-1} \tag{6-4}$$

where a_1, a_2, a_3 are defined as follows:

$$a_1 = \frac{T_s - 2R_1C_1}{T_s + 2R_1C_1}, \quad a_2 = \frac{(R_0 + R_1 + 2R_0R_1C_1)}{1 + R_1C_1s}$$
$$a_3 = \frac{(R_0 + R_1 + 2R_0R_1C_1)}{1 + R_1C_1s} \tag{6-5}$$

Given $E_T = U_L - U_{ocv}$, an expression can be derived for the terminal voltage U_L.

$$U_{L,k} = (1 - a_1)U_{ocv,k-1} + a_1U_{L,k-1} + a_2I_{L,k} + a_3I_{L,k-1} \tag{6-6}$$

Equation (6-6) can be written as a autoregressive exogenous model (ARX) shown in Equation (6-1) where $y_{RLS,k} = U_{L,k}$ $\hat{\varphi}_k = [1 \;\; U_{L,k-1} \;\; I_{L,k} \;\; I_{L,k-1}]$ and $\hat{\theta}_{RLS,k} = [(1 - a_1)U_{ocv,k}\; a_1 \;\; a_2 \;\; a_3]$. Once the ARX model is developed, the RLS algorithm can be executed for determining the model parameter update. The RLS gain, $L_{RLS,k}$, represents the confidence in the parameter update and is calculated using Equation (6-7).

$$L_{RLS,k} = P_{k-1}\varphi_k^T [\lambda_{RLS} + \varphi_k^T P_{k-1}\varphi_k] \quad (6\text{-}7)$$

where $P_{k-1}$is the covariance matrix for the parameters at the last time step and λ_{RLS} is the forgetting factor. The covariance matrix can be continuously updated at each iteration using the following equation.

$$P_k = P_{k-1} - (L_{RLS,k}\, \varphi_k^T\, P_{k-1})\, \lambda_{RLS}^{-1} \quad (6\text{-}8)$$

Finally, the parameters can be updated using the new values of the *RLS* gain and covariance matrix as shown in the equation below.

$$\hat{\theta}_{RLS,k} = \hat{\theta}_{RLS,k-1} + L_{RLS,k} [U_{L,k} - \varphi_k \hat{\theta}_{RLS,k-1}] \quad (6\text{-}9)$$

The parameter values obtained from the RLS algorithm can be used as inputs in the EKF. It should be noted that the value of the OCV, shown in Equation (6-6), can be obtained using the EKF algorithm. The rest of this section will explore the derivation of the EKF filter equations.

To clearly illustrate the EKF algorithm, consider the following non-linear system:

$$x_{k+1} = f(x_k, u_k, \theta_{RLS,k}) + w_k \quad (6\text{-}10)$$

$$y_{EKF,k} = g(x_k, u_k, \theta_{RLS,k}) + v_k \quad (6\text{-}11)$$

To apply Kalman filter theory, the above non-linear model needs to be written in discrete state-space form shown below:

$$x_{k+1} = A_k x_k + B_k u_k + w_k \quad (6\text{-}12)$$

$$y_k = C_k x_k + D_k u_k + v_k \quad (6\text{-}13)$$

Due to the non-linearity of the model, the battery equations can only be written in state space form by carrying out a Taylor series expansion. Linearization of the battery model will yield the following $\hat{A}_k$ and $\hat{C}_k$ matrices.

$$\hat{A}_k = \left.\frac{\partial f(x_k, u_k, \theta_{RLS,k})}{\partial x_k}\right|_{x_k = \tilde{x}_k} \quad (6\text{-}14)$$

$$\hat{C}_k^{\theta} = \left.\frac{\partial g(x_k, u_k, \theta_{RLS,k})}{\partial x_k}\right|_{x_k = \tilde{x}_k} \quad (6\text{-}15)$$

After linearization of the model, the Kalman filter equations can be utilized. This filter consists of two distinct steps at each measurement interval. It will first update the state vector and the

covariance matrices of the states. The state vector is updated by incoporating the system inputs into the state space model, where the expected process noise is assumed to be normally distributed with a mean of zero and a variance of Σ_{w}.

$$\tilde{x}_k^- = f\left(\tilde{x}_{k-1}^+, u_{k-1}, \theta_{RLS,k-1}\right) \tag{6-16}$$

In addition, the covariance matrix is updated based on the $\hat{A}_{k-1}$ matrix shown above and the process covariance matrix Σ_{w}.

$$\Sigma_{\tilde{x},k}^- = \hat{A}_{k-1}\Sigma_{x,k-1}^+\hat{A}_{k-1}^T + \Sigma_w \tag{6-17}$$

After the time update step, the measured value is used to obtain a better estimate for the state. This correction step takes new information from the measurement and is often referred to as the measurement update. The term $U_{L,k} - g(\tilde{x}_k^-, u_k)$ in the equation below represents the difference between the measured voltage and the predicted voltage from the battery model and is referred to as the output error or "innovation". A large innovation will lead to a bigger update while a smaller innovation will result in a smaller update. This output error can be a result of measurement noise, incorrect state estimate or an incorrect model. The following equation can be used to update the battery states:

$$\tilde{x}_k^+ = \tilde{x}_k^- + L_{EKF,k}\left[U_{L,k} - g\left(\tilde{x}_k^-, u_k, \theta_{RLS,k}\right)\right] \tag{6-18}$$

The Kalman gain matrix can be calculated using the equation below.

$$L_{EKF,k} = \Sigma_{\tilde{x},k}^-\hat{C}_k^T\left[\hat{C}_k^\theta\Sigma_{\tilde{x},k}^-\hat{C}_k^T + \Sigma_v\right]^{-1} \tag{6-19}$$

Intuitively, we can think of the Kalman gain as a matrix of weights that determines how large an update is required at a given time step. From the above equation, it can be seen that the value of the Kalman gain is determined by the covariance matrix of the state and that of the measurement noise. If the value of the state has a large amount of uncertainty, then the Kalman gain and update will be high. The opposite is true when the state has a small degree of uncertainty. Similarly, we can conclude from the above equation that a large error in measurement noise will result in a small Kalman gain and hence, less importance is given to the measurement. Finally, the covariance matrix can be updated using the equation shown below.

$$\Sigma_{\tilde{x},k}^+ = \left(I - L_{EKF,k}\hat{C}_k^\theta\right)\Sigma_{\tilde{x},k}^- \tag{6-20}$$

It is important to note that the model parameters used in Equation (6-18) are from the RLS algorithm. Therefore, both algorithms are running in parallel, simultaneously updating both the battery model parameters as well as battery states.

6.3.2 Pack Level SOC Estimation

Most real-world applications require connecting multiple cells in series and parallel in order to meet customer demands. Therefore, SOC values needs to be determined at the pack level. To understand what is meant by pack level SOC, consider the schematic shown in Figure 6-10.

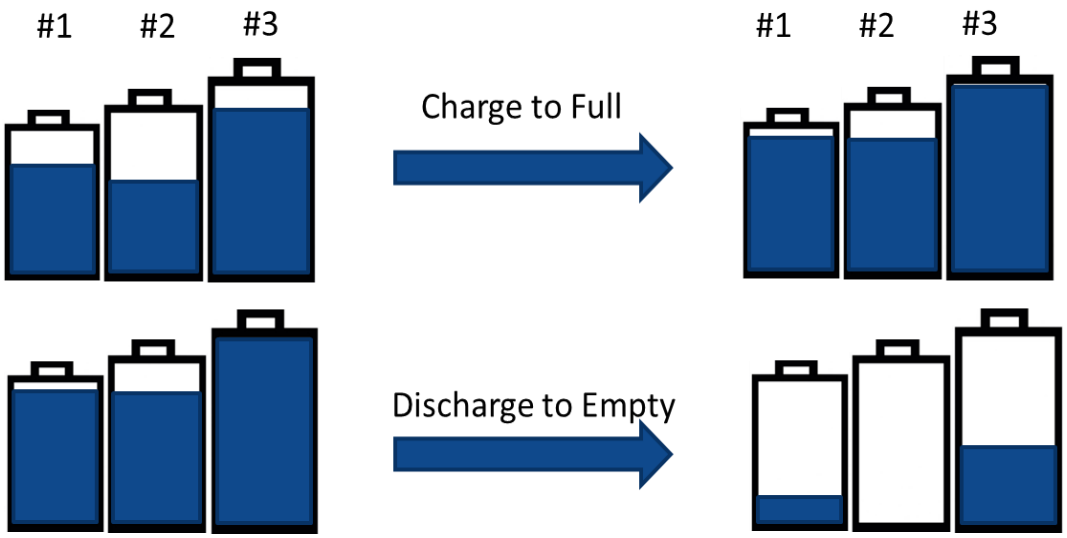

Figure 6-10: A schematic used to illustrate how the *min* and *max* cells within the pack determine the overall SOC.

Suppose there are three cells within the pack, each with slightly different capacity and at a different SOC. The capacity of the pack is limited by the first cell (in this case #3) to reach the upper voltage limit. In a similar way, when the pack is discharged, its capacity is based on the first cell (in this case #2) to hit the lower voltage limit. Therefore, the capacity of the pack can be defined as:

$$C_{p,n} = \min_{1 \le i \le N_{cell}} \left(SOC_i C_{n,i} \right) + \min_{1 \le j \le N_{cell}} \left(\left(1 - SOC_j \right) C_{n,j} \right) \qquad (6\text{-}21)$$

where N_{cell} is the number of cells within the pack. The SOC of a pack can then be given as a ratio of the minimum remaining capacity to the total capacity of the pack given in the above equation. Therefore, the pack SOC can be defined as:

$$SOC_p = \frac{Cap_{min\_r}}{Cap_{min\_r} + Cap_{min\_c}} \tag{6-22}$$

where Cap_{min_r} represents the remaining discharge capacity and Cap_{min_c} represents the remaining charge capacity. These two values can be determined using the first cell to charge to full and the first cell to discharge to empty. For this work, variables associated with the first cell to discharge to empty will be denoted with the subscript *min* and the first cell to charge to full will be denoted with the subscript *max.* Based on the capacity and SOC of these two cells, the following equation can be developed for pack SOC.

$$SOC_p = \frac{SOC_{min} * C_{min}}{SOC_{min} * C_{min} + (1 - SOC_{max}) * C_{max}} \tag{6-23}$$

The advantage of using the above equation is that if the pack is balanced, then the pack SOC automatically equals the SOC of the weakest cell. In situations where the pack is unbalanced, the pack SOC will gradually track between the SOC of the *min* and *max* cell. As a result, the proposed algorithm can not only account for changes in model parameters, but it can also be used for unbalanced battery packs.

Finally, careful consideration should be given to selecting of the *min* and *max* cell. In this work, the cell with the highest voltage will be as the *max* cell and the cell with the lowest voltage will be the *min* cell. This technique has been shown to work by Wang et at. [152] for a 14-cell battery pack at various operating conditions; hence, this approach will be incorporated into the overall SOC estimation framework.

6.3.3 Adaptive Coulomb Counting

Pack SOC estimates are continuously updated based on new measurement samples using the Kalman filter. The filter works by determining optimal battery states that minimize the deviation between measured and predicted terminal voltage. However, problems can arise if, in addition to noise in the system inputs and measurements, there are additional errors due to an inaccurate battery model. This can result in the illogical behavior described in Section 6.2.3.2.

These random fluctuations in SOC estimates are a direct consequence of inaccuracies in the battery model, leading to an incorrect prediction of the terminal voltage. Although this issue can be resolved using advanced electrochemical models, implementation of these algorithms on an embedded platform are limited due to constraints on computational resources. Therefore, to

overcome this issue, a novel adaptive coulomb counting approach is proposed that uses the pack-level SOC estimates to update the final SOC value reported to the user. The adaptive coulomb counting approach is shown in Figure 6-11.

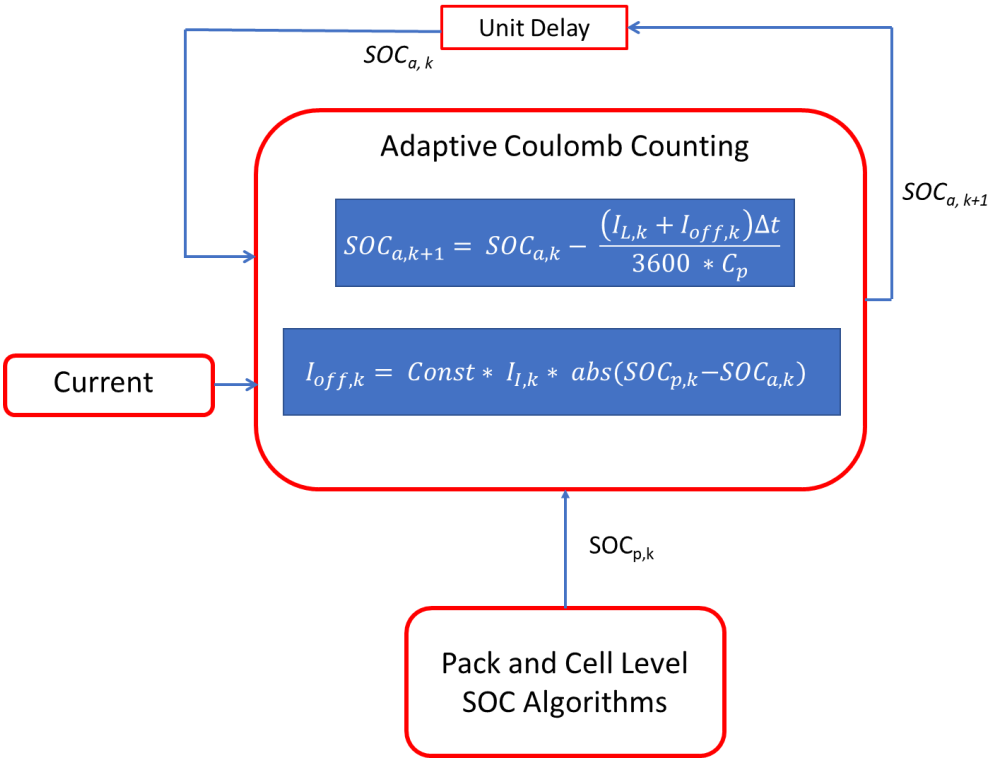

Figure 6-11: Adaptive coulomb counting technique for ensuring algorithm SOC tracking.

The algorithm works in a similar way as normal coulomb counting, except the pack level SOC is used to adapt the final SOC (represented as SOC_a). Equation (6-24) shows the adaptive coulomb counting equation.

$$SOC_{a,k+1} = SOC_{a,k} - \frac{(I_{L,k} + I_{off,k})\Delta t}{3600 * C_p} \quad (6\text{-}24)$$

where SOC_a represents the final algorithm SOC output, C_p is the capacity of the battery pack and $I_{off,k}$ is the offset current based on the pack level SOC. Employing an expression for coulomb counting at the top level ensures logical SOC tracking for the battery pack. For example, if the battery is at rest and the pack level SOC indicates that the SOC should decrease, the coulomb counting equation will ensure that the SOC remains constant. Therefore, rapid fluctuations in SOC that is often observed in Kalman filter approaches can be mitigated using this technique.

The magnitude of $I_{off,k}$ is proportional to the error between the SOC of the filter and the SOC from coulomb counting, as shown below.

$$Error_{soc} = abs(SOC_{a,k} - SOC_{p,k}) \tag{6-25}$$

The general idea is to slowly and logically adapt the algorithm SOC, in a manner that minimizes the term $SOC_{p,k} - SOC_{a,k}$. An expression can now be derived for the offset current $I_{off,k}$.

$$I_{off,k} = I_{I,k} * \underbrace{K_{const} * Error_{soc}}_{A\ fraction\ of\ the\ applied\ current} \tag{6-26}$$

where K_{const} is a tunable constant and $I_{I,k}$ is the applied current at that particular time step. Since only a fraction of the applied current is used, the displayed SOC value will not only behave logically, but will also have low estimation error. The value of K_{const} can be tuned based on how quickly the user wants to minimize the deviation between $SOC_p - SOC_a$. From this work, it is observed that using a K_{const} value between 0.5 and 10 produces reliable results.

In addition, the K_{const} can be either negative or positive depending on the operating conditions. Since the sign of the current switches as the battery moves from charge to discharge, the offset current needs to adapt to this change. The table below shows the sign of the K_{const} variable for different scenarios.

Table 6-1: The sign of K_{const} variable to account for both charging and discharging scenarios.

	$SOC_p > SOC_a$	$SOC_p < SOC_a$
Charging current	**Positive**	**Negative**
Discharging current	**Negative**	**Positive**

To better understand how the algorithm works, consider the following scenario. The battery is charging and the Kalman filter (SOC_p) is suggesting that the true SOC is higher than the SOC reported by adaptive coulomb counting (SOC_a). Therefore, an additional offset current will be added to the applied current to raise the rate at which SOC increases. Using this approach, the SOC will gradually increase to meet the SOC of the Kalman filter slowly and in a well-behaved manner. The robustness of the adaptive coulomb counting algorithm will be examined in greater detail in Section 6.4.1.

6.4 Results and Discussion

The purpose of this section is to evaluate the performance of the proposed SOC algorithm under different operating conditions. More specifically, the following questions will be addressed:

1. When does illogical SOC behavior occur and how can the proposed algorithm solve this issue?
2. Can the proposed algorithm accurately account for measurement noise in the current sensor?
3. What is the highest SOC error that can be encountered in a battery pack and how does this error change as the battery enters the lower and upper SOC regions.
4. Can the proposed algorithm accurately track SOC when the battery pack is unbalanced?

To answer these four questions, the experimental tests were carried out on two types of battery chemistries: lithium iron phosphate (LFP) and lithium nickel manganese cobalt oxide (NMC). Each pack will consist of four batteries connected in series, where the capacity of each pack is between 20 Ah to 40 Ah. Nuvation BMS is used to measure the voltage, temperature and current at each time step. The obtained experimental data is then fed to the proposed SOC algorithm, which is implemented in MATLAB. The algorithm output is compared to actual SOC estimates and conclusions can be drawn about algorithm accuracy. It should be noted that the current profile, specifically designed to answer each of the four questions, is summarized in Section 6.2.3.

6.4.1 SOC Current Drift - Results

One of the main advantages of using a closed-loop SOC estimator is that an offset present in the current shunt can be accurately removed. To test whether this statement applies to the proposed algorithm, the first validation test was executed for NMC batteries at ambient conditions. The voltage response of each cell within the battery is shown in Figure 6-12. It should be noted that the voltage profile never reached the upper or lower voltage thresholds of the battery pack. Therefore, the BMS cannot calibrate its SOC and so the offset error will gradually increase over time.

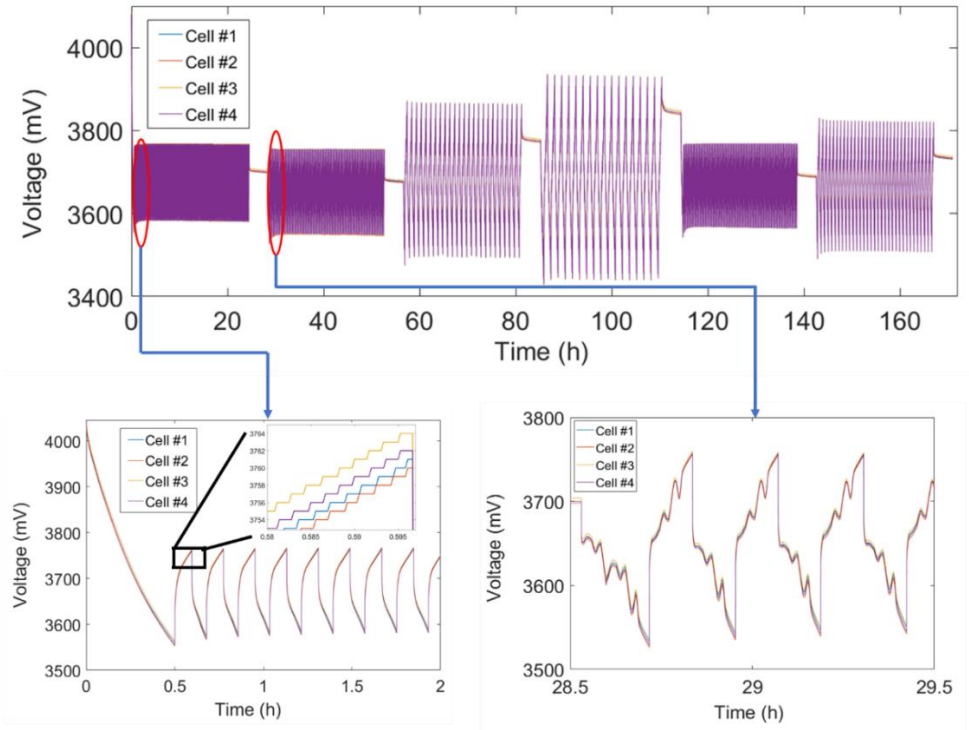

Figure 6-12: Voltage response for NMC battery pack for the first SOC validation test.

Figure 6-12 illustrates the battery voltage response for NMC under different current transients. During constant current charge for the first 24 hours, the voltage gradually rises and decays as the battery is charged and discharged. As the applied load switches to a frequency regulation type profile, more rapid changes in voltage are observed as shown in the bottom right of Figure 6-12. The validation test stresses the battery under these different current transients to ensure that the algorithm will work under various battery cycling conditions. Figure 6-12 also shows that the voltage within the cells in series are within 5 mV of each other. Therefore, this test does not account for any pack imbalance upon cells.

Upon completion of the validation test, the battery was charged up to full to determine the final SOC value of the pack. Using this point, the offset error present in the current shunt can be determined. This offset error was then removed before applying the coulomb counting algorithm, to ensure that a proper benchmark was used. The results acquired from the validation test are shown in Figure 6-13.

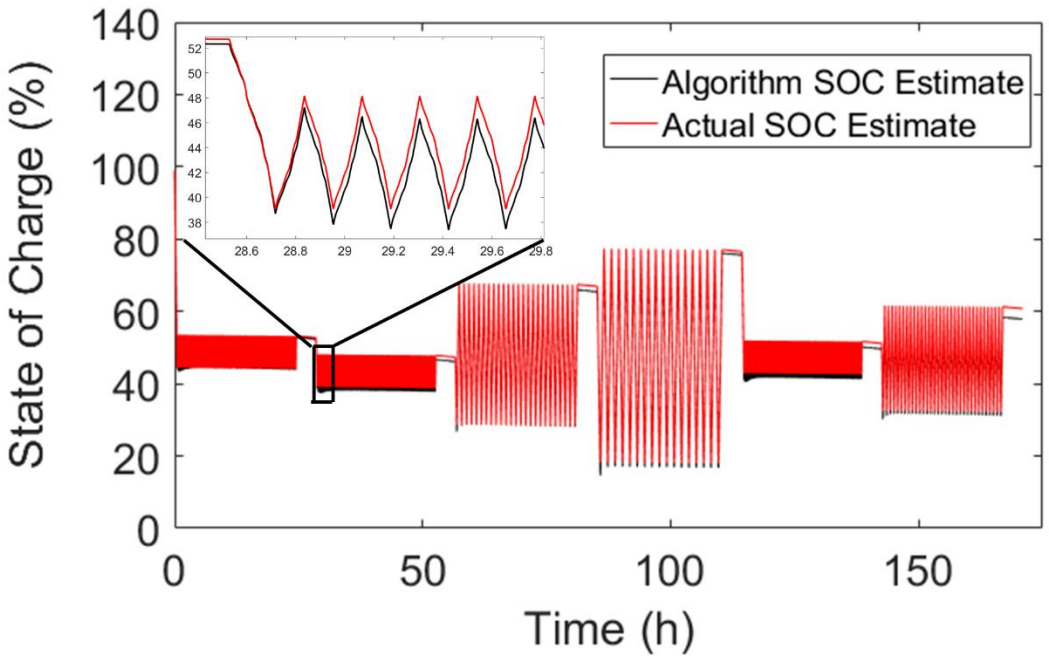

Figure 6-13: SOC estimated by the algorithm in comparison to coulomb counting, which in this test is used as the benchmark.

Figure 6-13 depicts excellent agreement between coulomb counting results and the proposed SOC estimates, with the maximum observed error less than 4% and an average error of 1.2%. Unlike coulomb counting, the accuracy of the algorithm does not diminish as the battery is cycled over a period of several days, nor does the algorithm require calibration at any point. The results indicate that the proposed algorithm provides excellent SOC tracking and can be used in BMS applications that do not reach critical voltage thresholds.

Although the offset that was inherent to the current shunt was successfully removed, an additional current offset can be introduced in simulation to evaluate the robustness of the algorithm to measurement noise. For this particular simulation, an offset of 25 mA was introduced, a value commonly encountered for a hall effect sensor. The percent SOC error is shown in Figure 6-14 below.

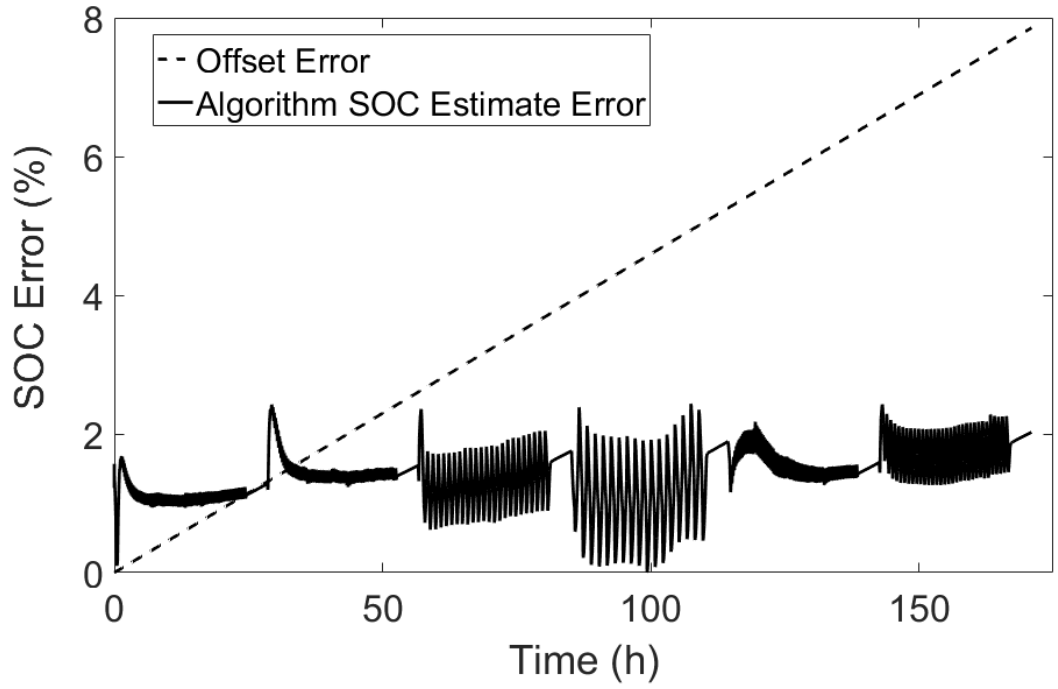

Figure 6-14: Accumulation of SOC error over time for coulomb counting and the proposed algorithm when an offset error is introduced.

In this situation, coulomb counting is no longer accurate since a 25-mA offset error is introduced in the current measurements. The steadily increasing dashed line in Figure 6-14 is indicative of what would happen if coulomb counting was used in determining SOC. After a period of 7 days, an SOC error around 8% is observed and this value will continue to increase in a linear fashion until the BMS is calibrated by carrying out a full cycle. The solid line depicts the proposed algorithm error, where the simulated offset has no effect on performance accuracy. This result is beneficial to BMS manufacturers as it allows them to reduce hardware costs associated with a more precise current shunt.

6.4.2 SOC Logical Behavior – Results

Illogical SOC tracking is frequently observed in LFP batteries due to the flat characteristic of the OCV-SOC curve. For example, a battery that shifts from 60% to 40% SOC experiences a total voltage change of only 7 mV. Consequently, even small measurement noise or model error can produce a substantial estimation error in the SOC estimate. To test the accuracy of SOC tracking in this region, a battery pack composed of four LFP cells, were cycled in the battery test station

using the current profile generated in Section 6.2.3.2. The results of the algorithm with and without adaptive coulomb counting, are shown in Figure 6-15.

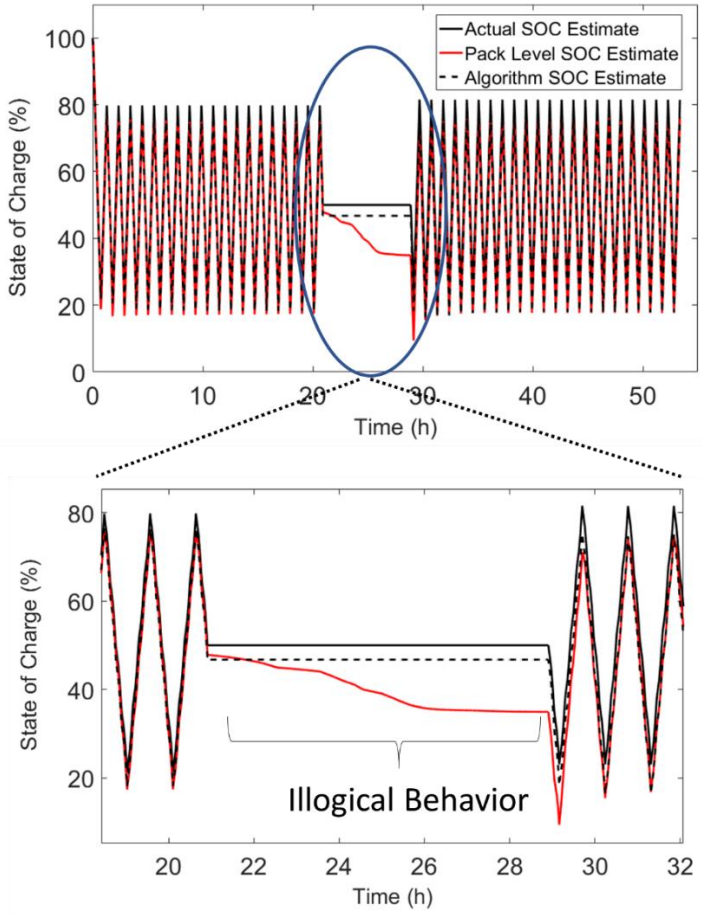

Figure 6-15: Results of the SOC estimation algorithm with and without adaptive coulomb counting.

The red line represents SOC tracking when no adaptive coulomb counting algorithm is included. It can be seen that during the 8-hour rest period, the SOC of the Kalman filter slowly tracks downward when it should remain constant. By incorporating the adaptive coulomb counting algorithm, the SOC estimates are shown to behave logically (dashed black line). In addition, the Kalman filter SOC error incurred during the rest period can be significantly reduced using the proposed three-level approach. A maximum SOC error can be reduced from 15% to under 7% by incorporating the adapting coulomb counting algorithm into the SOC estimation framework. Therefore, it can be concluded that by combining the adaptive capability of Kalman filtering with coulomb counting, a more reliable and accurate SOC estimate can be obtained.

6.4.3 SOC End-Points Error – Results

The purpose of this section is twofold. First, it is important to quantify the maximum error that could occur when the LFP battery pack is continuously cycled within the 40% to 60% SOC region. As discussed in Section 6.4.2, this is an extremely difficult area for SOC estimation since the gradient of the OCV-SOC curve is small. Second, it is essential to explore the change in SOC error as the battery pack is discharged to empty or charged to full. As the battery nears its upper and lower voltage limits, the OCV-SOC curve gradient is considerably higher and a more accurate estimate is conceivable. The error obtained throughout the test is summarized in Figure 6-16.

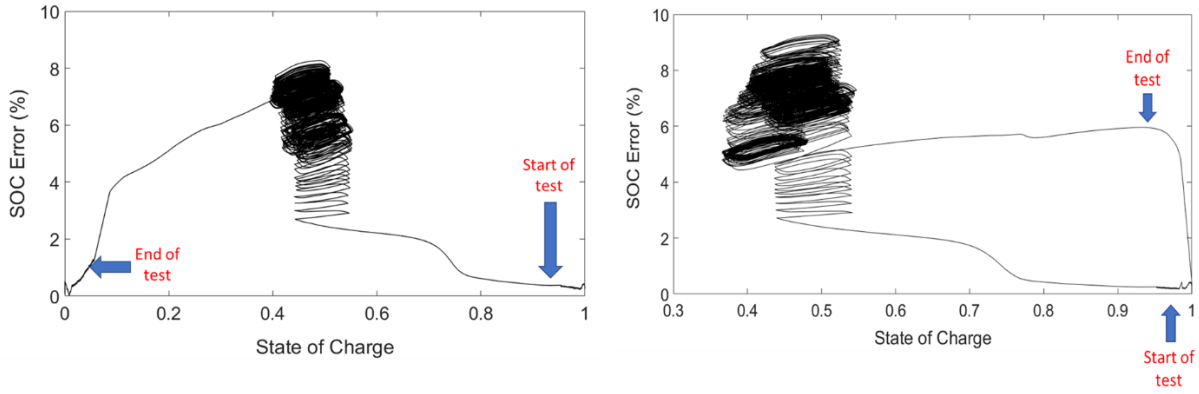

Figure 6-16: Algorithm performance throughout the validation test as a function of SOC.

Figure 6-16 A) illustrates the change in SOC error as a function of battery SOC for the first validation test. Recall that the consecutive steps involved in this experiment are: a discharge to 50%, constant battery cycling in the 45% to 55% SOC region for 24 hours and a discharge to empty. Following the SOC error curve in Figure 6-16 A) as the battery is discharged to 50%, the SOC error is initially under 4%. Subsequently, as the battery is cycled in the mid-band SOC region, the error begins to increase and reaches a maximum at around 8%. The higher error at this point is a result of the flat OCV observed in this region. However, it is important to notice that the error is significantly reduced as the battery reaches its lower SOC limits; the error at 10% SOC is once again back under 4%. Therefore, the magnitude of the SOC estimation error is dependent on the gradient of the specific battery chemistry. Using the proposed algorithm, although a high SOC error might be incurred at the mid SOC region, the error drops as the battery is discharged to empty. The same trend can be observed in Figure 6-16 B), where the cell is charged to full.

6.4.4 SOC Unbalanced Pack – Results

Two different validations tests were carried out to assess algorithm accuracy. It is worth noting that very little work currently exists in literature that examine SOC estimation for an unbalanced battery pack. The first test, described in Section 6.2.3.4, explores the scenario of an unbalanced battery pack, where no balancing algorithm is available. Two cells in the pack were brought to an SOC of 40%, while the other two cells were charged up to 50%. The algorithm SOC estimates for the *min* and *max* cell are first compared with the actual SOC estimate and the results are shown in Figure 6-17.

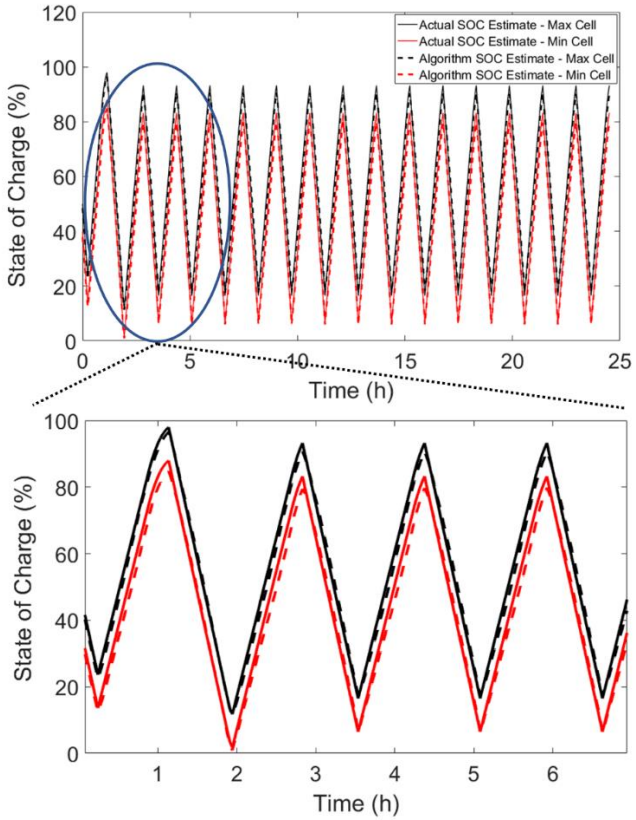

Figure 6-17: Algorithm SOC estimates for *min* and *max* cell compared to actual SOC values for an unbalanced pack.

The key take-away from the results in Figure 6-17 is that the algorithm accurately estimates both the *min* and *max* cell. The maximum SOC estimation error was found to be below 3% throughout the test. Therefore, for a fresh battery pack, using voltage as an indicator for the *min* and *max* cell can yield favorable results. Next, it is important to monitor pack SOC tracking as the

battery is charged and discharged. The actual pack SOC should begin to match the SOC of the highest cell when the battery is almost full. At the middle SOC region, the pack SOC value should be an average of two cells. And finally, as the cell is discharged to empty, the SOC should gradually move towards the cell with the smallest SOC. The pack level results are shown in Figure 6-18.

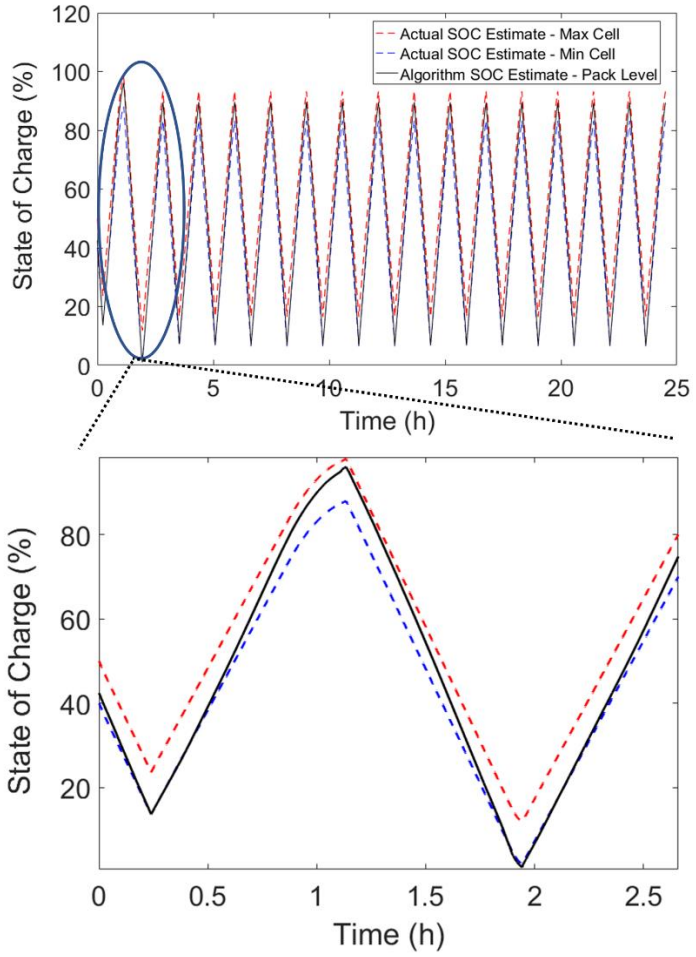

Figure 6-18: SOC track behavior of the proposed algorithm for an unbalanced battery pack.

Examining Figure 6-18, it is important to notice that the algorithm SOC gradually shifts from the *min* cell to the *max* cell as expected. This indicates that the algorithm is able to accurately account for the smaller capacity that is present due to battery imbalance.

The second validation test, already described in Section 6.2.3.4, explores the scenario of a battery pack that is initially unbalanced but gradually becomes balanced upon cycling. The initial

imbalance can be a result of a number of factors, including cell replacement in the battery pack. To understand the effect of balancing, consider the *min* and *max* SOC estimates for both the algorithm SOC and coulomb counting SOC (Figure 6-19).

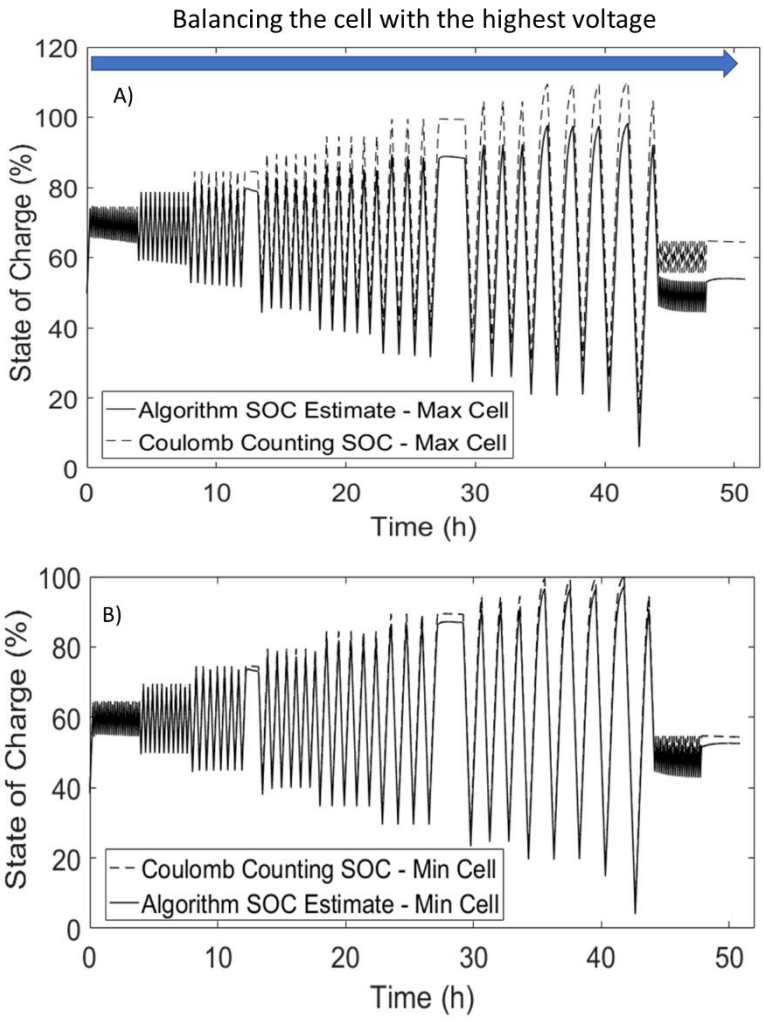

Figure 6-19: Coulomb counting and algorithm SOC for min and max cell in the battery pack

Since balancing is based on the cell with the highest voltage, the SOC of the *min* cell is not affected by BMS balancing. This is the reason why there is a strong agreement between the algorithm and coulomb counting SOC results shown in Figure 6-19 A). The deviation between algorithm and coulomb counting is more pronounced for the *max* cell as illustrated in Figure 6-19 B) and this difference continues to increase as the cell is cycled. This divergence over time is a direct result of balancing occurring on the *max* cell. The algorithm SOC is able to accurately estimate SOC of the *max* cell, whereas coulomb counting is unable to account for the capacity

discharged through balancing. These results indicate that the algorithm proposed in this work can successful resolve any changes in cell SOC due to balancing in order to provide a more reliable estimate compared to coulomb counting.

6.5 Conclusions

In this work, a comprehensive SOC estimation algorithm is proposed, consisting of three levels. The first level involves using RLS to estimate model parameters coupled with an EKF for updating the battery SOC. This approach is executed for the *min* and *max* cells within the pack, where the individual cells were selected based on the maximum and minimum terminal voltages. The second level takes the *min* and *max* SOC values and estimates a pack level SOC. Finally, an adaptive coulomb counting level is applied at the top to ensure the algorithm SOC output behaves logically. The algorithm is validated for NMC and LFP battery chemistries, and the following conclusions can be made

1. One computationally efficient approach to ensure logical and more accurate SOC tracking is to use the proposed adaptive coulomb counting approach
2. The SOC tracking in all situations behaves logically. This means that the SOC does not change during periods of rest and only increases or decreases when the battery is subjected to charging and discharging.
3. The proposed algorithm is able to account for a current offset as high as 25 mA. This indicates that a cheaper current shunt can be implemented for some ESS units, saving money for the BMS manufacturer.
4. The algorithm is shown to converge to the true SOC value at the upper and lower SOC limits. This is advantageous since a large number of decision are normally made in this regime.
5. The SOC algorithm is shown to accurately track between the *min* and *max* cell for an unbalanced battery pack. In addition, the algorithm can account for any changes to the cell SOC that is a direct result of BMS balancing.

Chapter 7: Simulation of Cell Replacement in a Lithium-Ion Battery Pack

The following chapter is based on the paper by Manoj Mathew, Quing Kong, Jake McGrory, and Michael Fowler published in *Journal of Power Sources* (JPS): **"Simulation of lithium ion battery replacement in a battery pack for application in electric vehicles".**

The author's specific contribution was in developing the cell replacement framework and algorithms, conducting experiments, carrying out the simulations, preparing the results, graphs and manuscript. Michael Fowler offered guidance on the research, while Quing Kong and Jake McGrory were co-operative education undergraduate student who assisted with implemented the code in MATLAB.

7.1 Introduction

The use of lithium-ion batteries (LIB) in vehicles is becoming increasingly prevalent and their market share is only projected to grow. Lithium-ion (Li-ion) batteries are considered to be the best battery choice for most applications at this time due to their high energy-density and high power-density. However, over time, the battery pack in an electric vehicle (EV) will age, decreasing its capacity to store energy (i.e. capacity fade) and losing its ability to deliver maximum power (i.e. power fade), until it is eventually not suitable for use in a vehicle [153].

It is generally accepted that the end of life (EOL) of a vehicle battery pack can be defined as when its maximum capacity fades to 80% of its nominal maximum capacity [62]. As it stands, a vehicle battery pack is either disposed of or repurposed for stationary applications at EOL [154]. However, due to cell-to-cell variations or position within the pack, not all the cells will degrade at the same rate. This can be due to variation in cell resistance, uneven thermal management of the pack, differences in active material and several other factors that are characteristic of the manufacturing process and pack configuration [155]. Therefore, this implies that in a battery pack that has reached its EOL, one can find cells that have lost more or less than 20% of their nominal capacity. Using a routine preventative maintenance strategy, degraded cells may be identified so that they can be replaced to prolong the service life of the pack as a whole. Also, any cell that may have failed for any other reason could also be replaced. This will require consideration in the

design phase of the battery pack, pack configuration or assembly, as well as consideration within the battery management system (BMS). In order to prolong the primary in-service lifetime of the battery pack, damaged cell or modules can be replaced with new ones.

This concept of routine maintenance and refurbishment is an established practice in the automotive industry in which a system, such as an engine, is not replaced entirely upon failure, but has certain parts replaced with regular maintenance. For some systems, the replacement of every component on a certain interval can extend the system's life indefinitely [156]–[158]. The American automotive remanufacturing industry is a multi-billion dollar industry for fossil fuel vehicles, and the economic, environmental and legislative benefits of remanufacturing are well-documented [156]. Therefore, it is of interest to investigate this model as it pertains to future technologies such as LIB's in vehicles by changing out degraded cells in the battery pack as they fail without replacing the entire pack. The goal of this is to maintain the capacity and available power of the battery pack above a defined EOL criterion.

Significant efforts have been made in going from single-cell battery models to pack-level models, taking into account cell to cell variability [159]–[161]. With respect to state-of-charge (SOC) estimation, many new considerations and challenges arise at the battery pack level [147]–[149], [151], [162]–[164]. For example, Sun et al. [164] employed an average pack model and model bias correction, taking into account model and parameter uncertainty in order to estimate SOC. The shift in focus towards the battery pack from the cell is important, because it is the battery pack that is implemented in electric vehicles (EVs), and it is the battery pack that must be accurately monitored and modelled. A battery pack configuration that is rigid is not advantageous to EV manufacturers since the performance of cells in series is limited by the weakest cell. Therefore, the idea of reconfigurable and/or maintainable battery packs have gained attention in recent years, where if certain cells or modules fail, they can be replaced or removed from the battery pack circuit.

Although a few studies in literature have explored the idea of reconfigurable battery packs, little research currently exists on simulating a battery pack with the concept of cell change out, and none on a vehicle scale. Adany et al. [165] have conducted preliminary work in switchable configurations, where the BMS removes a cell that is deemed to negatively impact the rest of the battery pack. Ugle et al. [166] proposed a metric called worthiness of replacement, a quantitative

measure of whether a battery module that has degraded needs to be replaced with a new one. Although not specifically addressed by Ugle, nor examined in detail in this work, the concept of battery change-out could be applied to a single cell, a group or 'gang' cells, a 'string' of cells, or a 'module'. Ganesan et al. [167] investigated the idea experimentally in the context of state-of charge (SOC) estimation, and showed that the concept can extend the useful life of a battery pack. However, the investigation by Ganesan et al. lacked the scope that the current work will attain in terms of battery pack size and lifetime. Similarly, although there have been numerous articles that have proposed a comprehensive battery simulator that take into account degradation [168]–[170], none of these studies have examined the effects of replacing a damaged cell with a new one. The goal of this chapter is to provide a simulation framework for cell replacement in a battery pack for electric vehicles. This simulation results will then be used to examine how quickly the cells need to be replaced in order to maintain the state-of-health (SOH) of the battery pack above a certain threshold. If the model simulations show that cell change-out extends pack life indefinitely while maintaining pack performance at steady-state, the concept would be of interest to EV and battery manufacturers for its economic benefits. The change-out concept would hopefully lead to a reduced load of batteries on the recycling and disposal infrastructure as a 'good' or long-lasting cell would remain in service for extended longer period of time. This environmental benefit could also be legislatively advantageous if LIB disposal policy becomes strict [171].

7.2 Experimental

The two different battery chemistries used in this study were lithium iron phosphate (LFP) and a mixed cathode chemistry of lithium nickel magnesium cobalt oxide (NMC) and lithium magnesium oxide (LMO). Both were automotive patterned cells with a pouch configuration. Experimental data was collected in order to develop a robust battery pack model, where each battery in the pack has a slightly different voltage profile and degradation rate. This was accomplished by testing four different LFP cells and four different NMC/LMO cells. The variation in the parameters obtained from these cells were then used to develop a distribution that was applied to stochastically generate the parameters for each individual cell in the battery pack simulation. The manufacturer specifications for each battery are given in Table 7-1.

Table 7-1: Manufacturer specifications for the batteries tested

Parameter	Value	
Cathode Chemistry	Lithium Iron Phosphate (LFP)	Lithium Nickel Magnesium Cobalt Oxide (NMC) / Lithium Magnesium Oxide (LMO)
Type of Cell	Pouch	Pouch
Nominal Capacity (Ah)	20	15
Rated Voltage Range (V)	2.00 – 3.65	2.80 – 4.15

7.2.1 Experimental Set-up and Procedure

All tests were carried out using a BioLogic EC-Lab VSP multi-channel potentiostat/galvanostat. The equipment is equipped with 4 channels, where each channel can provide a maximum of 400 mA. In order to test the pouch cells, a 100Amp booster was attached, allowing a maximum current of 100 Amps and a voltage range of 0V to 5V.

In order to determine the parameters of the equivalent circuit model (ECM), the following procedure was applied: The cell was initially charged at 1C constant current to its upper voltage limit followed by constant voltage charge until the current was below C/25. The hybrid pulse power characterization test (HPPC), proposed by the Department of Energy (DOE), was then carried out at 10% intervals from 100% to 0% SOC. The HPPC test consists of a 1C discharge for 10 seconds, a 40 second rest period and a ¾ C charge for 10 seconds. Constant current 1C discharge was applied to move to different SOC levels and a one-hour rest was conducted in between HPPC tests in order to ensure that the battery reached equilibrium.

The open circuit voltage (OCV) curve was determined by subjecting the cells to a C/25 discharge current for 25 hours followed by an hour of rest and a C/25 charge current for another 25 hours. The OCV curve was then calculated by taking the average of the charge and discharge curves.

7.3 Algorithm Development/Simulation Framework

The cell-level voltage response model and pack-level simulation framework were the exact same for each battery chemistry. The only difference between battery chemistries were the circuit

parameters values in the model and the degradation model chosen for the simulation. The decision to test the simulation with different battery chemistries was made to determine the robustness of the change-out concept.

7.3.1 Cell-Level Voltage Response Model Development

The cell-level model was built on the concept of an ECM due to constraints in computation time. The Thevenin ECM was used to represent cell voltage response since the model provided a good balance of accuracy and computational efficiency. This ECM was also chosen based on its merits in representing fundamental characteristics of LFP and NMC/LMO batteries [172], [173]. The ECM consists of the R_0 parameter, which represents the internal resistance of the cell and RC parameters R_1 and C_1, which model the transient voltage response to changing current. The voltage source of the ECM represents the open-circuit voltage (OCV) of the cell and is varied with SOC. The ECM is shown in Figure 7-1.

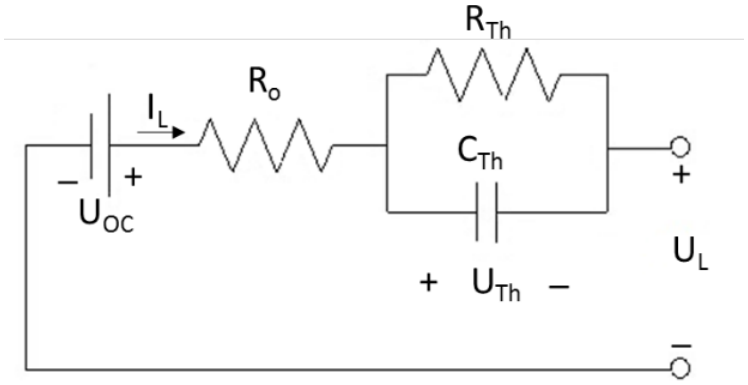

Figure 7-1: Thevenin ECM used for voltage response in the cell change out simulator.

The ECM can be written in the form of a differential equation as shown below.

$$\frac{d(U_{th})}{dt} = -\frac{U_{th}}{R_1 C_1} + \frac{I_L}{C_1} \tag{7-1}$$

$$U_L = U_{oc} - U_{th} - I_L R_o \tag{7-2}$$

The parameters R_o, R_1 and C_1 can be determined using the procedure outlined in Section 7.2.1. For a given current and SOC, solution of Equations (7-1) and (7-2) can yield the terminal voltage.

7.3.2 Degradation Model Development

The voltage response model needs to be coupled with a degradation model in order to adequately predict the degradation profile of a battery pack. During the simulation of the battery pack, the degree of degradation of the particular cell will continuously be evaluated based on its charge history. Several cycling aging models have been proposed in the literature, including both empirical and fundamental approaches. Generally, cycling aging models consider the effects of charge throughput, depth of discharge (DoD), current rate and average cell SOC [62], [174], [175] on capacity and power fade.

The empirical degradation model based on concepts originally proposed by Schmalstieg et al. [174] was used in this work to model degradation in the LFP cells. The model considers the effects of the depth of discharge of the cell as well as the average voltage of the cell throughout the current profile. The model was simplified slightly to depend only on cycling aging factors and neglect calendar aging. Equations (7-3) to (7-5) show the degradation equations modeling capacity fade and resistance increase. Although Chapter 4 and 5 focused only of resistance estimation, it should be noted that both capacity fade and power fade is modeled in this work. This is because Chapter 4 and 5 was tailored towards stationary applications, whereas this chapter attempts to develop a comprehensive model that can be applied to both stationary and vehicle applications. The terms β_{cap} and β_{res} represent fitting parameters and were calculated in the same form, shown in Equation (7-5), but with different values of *a*, *b*, *c* and *d*. [174].

$$CAP_{cyc} = 1 - \beta_{cap}\sqrt{Q_{processed}} \tag{7-3}$$

$$Res_{cyc} = 1 + \beta_{res}Q_{processed} \tag{7-4}$$

$$\beta_{cap/res} = a\left(V_{avg} - b\right)^2 + c + d * DoD \tag{7-5}$$

The term CAP_{cyc} represents the ratio of current cell capacity to the initial cell capacity. A ratio of one occurs when there is zero amp-hours processed, which indicates a new cell. This value decreases over time due to degradation of the cell. In a similar way, Res_{cyc} represents the ratio of the current cell resistance to the initial cell resistance. As the resistance increases over time, the ratio increases. The ECM, shown in Equations (7-1) and (7-2) can be solved for a given current

profile in order to determine the average voltage used in Equation (7-5). The depth of discharge (DoD) can be estimated from the coulomb counting block in Figure 7-2.

The degradation model proposed by Cordoba-Arenas et al. [176] formed the basis of the degradation model applied to the NMC/LMO chemistry. It also considered average SOC and charge throughput, but neglected depth of discharge (DoD). It additionally considers C-rate and temperature, although the temperature was taken to be constant 298 K in the simulation. This degradation model is governed by Equations (7-6) to (7-9), where R = 8.314 J K^{-1} mol^{-1}.

$$CAP_{loss} = a_c * exp\left(\frac{-E_{ac}}{R_g T}\right) * Q_{processed}^{z} \tag{7-6}$$

$$Res_{inc} = a_r * exp\left(\frac{-E_{ar}}{R_g T}\right) * Q_{processed} \tag{7-7}$$

$$a_c = \alpha_c + \beta_c * Ratio^{e} + \gamma_c (SOC_{min} - SOC_{0c})^{f} \tag{7-8}$$

$$a_r = \alpha_r + \beta_r (SOC_{min} - SOC_{0r})^{q} + \gamma_r * exp[g(CR_0 - CR) + h(SOC_{min} - SOC_{0r})] \tag{7-9}$$

The terms a_c and a_r represent the capacity and resistance severity factors that depend on C-rate (*CR)*, the minimum SOC (SOC_{min}), and the ratio between the time spent depleting and regenerating charge (*Ratio).* The terms *e, f, z,* α_c, β_c, γ_c, SOC_{oc} α_r, β_r, γ_r, SOC_{or}, CR_o, *g, h, and q* represents constants in the fitting equation, while E_{ac} and E_{ar} are the cell activation energy for the capacity fade and resistance increase processes respectively. The output from the models Cap_{loss} and Res_{inc}, represent the percent capacity loss [%] and resistance increase [%] respectively.

The above models, developed by Schmalstieg et al. [174] and Cordoba-Arenas et al. [176] were used for two main reasons. First, using an empirical model instead of a theoretical one is essential for reducing computational time, which can become a significant issue when simulating a large number of cells, especially with stochastic considerations. Secondly, both models contain fitting parameters that can be varied stochastically allowing one to develop a more realistic battery pack, where certain cells degraded more quickly than others. Note that in this work variation in the degradation associated with location of the cell within a pack not considered but left to future works (e.g. different cells will experience different thermal histories). The variability of the cells is a factor that will be considered in the simulation, and the effects of having cells that have a high degree of variability will be discussed with respect to cell change out.

7.3.3 Pack level voltage model

The pack-level model acts to aggregate results from an array of single cell models and to summarize the overall performance of the pack. It assumes a series orientation for all of the cells contained in an array of cells and simplifies a series of n Thevenin-based ECM to a single Thevenin-based ECM with n RC circuits. The pack-level model also outputs pack-level voltage, OCV, and SOC information with respect to the current profile, which is then used to evaluate the performance of the overall pack as it degrades.

The other role of the pack-level model is to consistently update cell-level circuit parameters in the pack. This ensures that the overall pack model reflects realistic series pack performance, in which all cells are subjected to the same current profile. It should be noted, however, that variation in degradation rate of each cell will result in variance in cycling characteristics for each cell such as DoD and SOC.

7.3.4 Simulation Framework

The simulation framework proposed in this paper combines the cell level voltage response model, the cell level degradation model and the pack level model. The simulation procedure was conducted in a MATLAB using object-oriented programming. Working in an object-oriented environment allows one to emulate individual cells that have unique characteristics. In this study, the pack used for the simulation was made up of 40 randomly generated cells in series. Therefore, the scale of the simulation was more one of a 'module' than a full EV 'pack'. The cells in the pack would vary in their equivalent circuit resistances and capacitance values as well as in how quickly they degrade. By stochastically varying these parameters, the simulation provides a more realistic prediction on how the pack would degrade over time. The battery pack was subjected to a charge/discharge cycle of 1C, between 20 and 80% average SOC. As the cells varied in capacity, the current profile was generated based on the average capacity of all the cells in the pack, in order to scale the 1C duty. Note that one cycle refers to one complete charge and discharge from 20% to 80% SOC. Therefore, if the cell was discharged from 80% SOC to 50 % SOC and charged back up to 80% SOC, this would only be considered as half a cycle. The framework used for the simulation is illustrated in Figure 7-2.

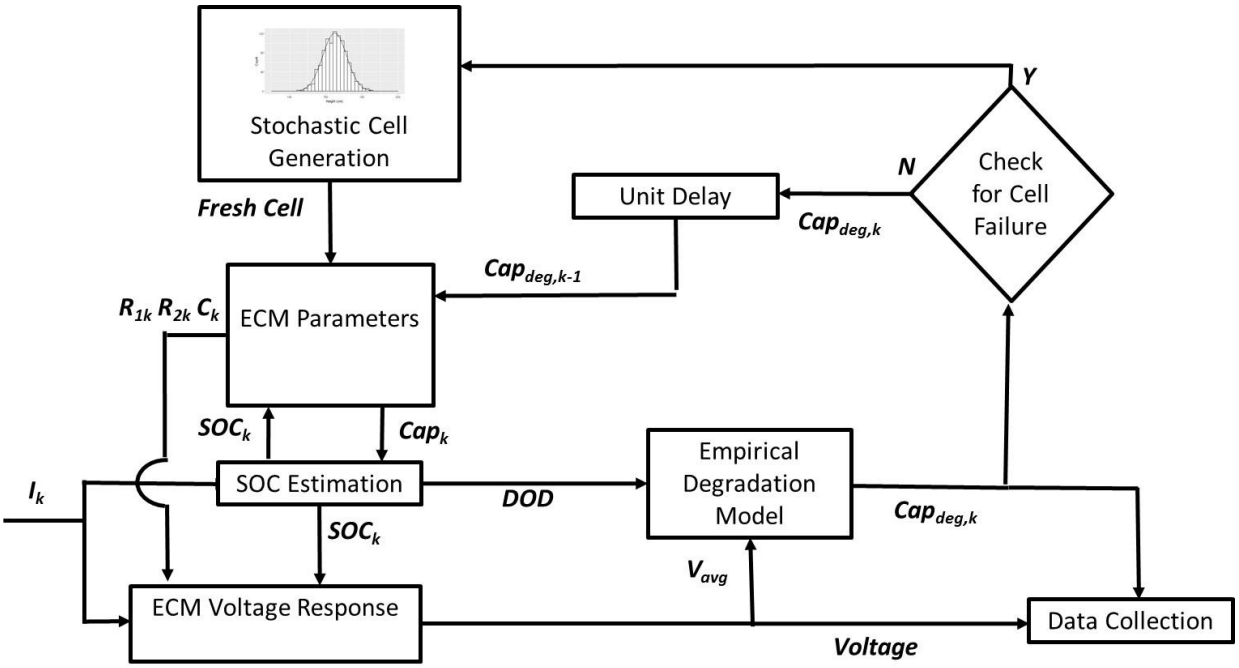

Figure 7-2: Framework of the cell change-out simulator for a battery pack.

At the beginning of the simulation, 40 new cells were created, each with its own unique parameters for the voltage response and degradation. Each cell has a meantime to failure (MTTF), which is defined as the amount of time it takes for the product, in this case a particular lithium ion battery cell, to reach its EOL. Stochastic variation was introduced by generating a distribution from the experimental data collected on the four LFP cells and four NMC/LMO cells drawing the ECM parameters from the distribution. Degradation rate was varied by stochastically varying the parameters the degradation model equations for both LFP and NMC/LMO (i.e. Equations (7-3) to (7-9)). Variations in capacity, cell parameters and degradation are well-documented in the literature [155], [161].

For a given current and array of cells in the battery pack, the first step is to calculate the SOC of each cell. One of the simplest SOC estimation methods is based on the notion that one can count the coulombs entering and leaving the battery. The equation for calculating the SOC is:

$$SOC = SOC_0 - \frac{1}{C_n} \int \frac{I_L}{3600}\, dt \qquad (7\text{-}10)$$

Where I_L is the current measured in coulombs/second, and C_n is the maximum battery capacity. The simulation starts from an SOC value of 80% for each cell and by integrating the amount of current, the current SOC value can be determined.

Using the ECM model described in Equation (7-2), the voltage for each of the cells in the pack is determined. Note that each battery in the simulator will produce a slightly different voltage response due to variations in the individual cells. The degradation model then takes the voltage and SOC for the cell as an input in order to calculate the capacity fade.

The capacity of each of the cells in the entire pack will be checked at discrete interval to ensure that all the cells are above the cell failure limit. The interval at which cell degradation was checked and cells were replaced will be referred to as maintenance event interval and cells that have capacity below a critical value will be removed and replaced with new ones. The number of cells replaced during a maintenance event will be referred to as replacement rate. This concept is widely used in remanufacturing models, where a "perfectly maintained system" is one where the replacement check is done continuously and "discretely maintained system" refers to a system that is checked at discrete intervals. Note that the maintenance event interval is an important parameter in this discussion since in electric vehicle applications, the replacement of cells or modules in a battery pack utilized in an electric vehicle can only be carried out at discrete intervals. For example, in a typical vehicle, the cells or modules might be inspected for degradation during the car's regular seasonal maintenance check.

One of the consequences of discretely maintained systems like EV battery pack is that irregular checks could theoretically miss the exact moment at which a cell exceeds its EOL capacity fade, and the cell would not be replaced until the next scheduled check for replacement took place. Therefore, the SOH of the battery pack could fall below 80% since an individual cell could fall below 80% in between checking intervals. Therefore, the individual cells need to be replaced when their capacity fade is above 80% in order to ensure that the entire pack does not degrade past 80%.

The capacity of each of the cells is recorded throughout the simulation procedure and a pack capacity is determined based on the capacity of the weakest cell. The ratio of the degraded cell capacity of the weakest cell with the nominal cell capacity allows for the estimation of SOH for the pack as shown in Equation 7-11.

$$SOH_{pack,cap} = \frac{\min(C_{cll1},\ C_{cell2}\ , \ldots, C_{cellN})}{C_{nominal}} * 100 \qquad (7\text{-}11)$$

Where $C_{nominal}$ represents the initial capacity of the specific battery. Although power fade is another metric that is often used to model SOH, previous works [176], [177] have shown that, for LFP and NMC/LMO batteries, the effect of resistance rise (via power fade) on cell performance is not significant compared to that of capacity fade for vehicle application. Although the analysis is not carried out in this work, examining stationary application will require battery resistance estimation rather than capacity estimation.

7.4 Results and Discussion

7.4.1 Cell Level Voltage Model Validation

Following the HPPC procedure taken by Scott [144], the ECM parameters were determined at various SOC's for 4 LFP cells. The results are plotted in Figure 7-3 (a-c). It was concluded that the parameters were constant enough in the range of SOC that would be simulated not to vary the parameters with SOC. This simplification improved computational time and the stability of the model. The C/25 charge-discharge cycles allowed for the calculation of nominal cell capacities and helped in developing the OCV curve.

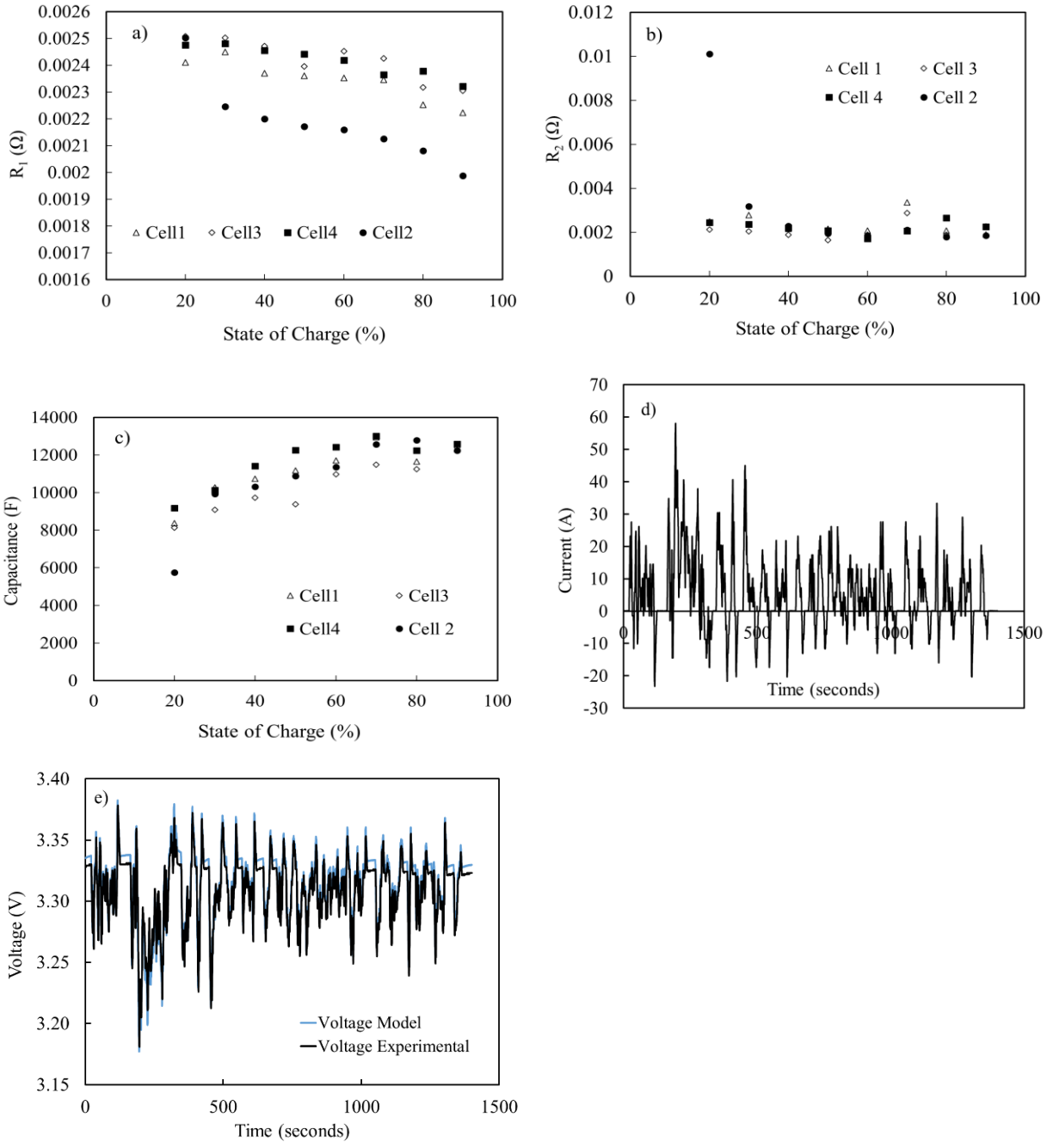

Figure 7-3: (a-c) ECM parameters estimated for 4 LFP cells; (d) current profile of the UDDS cycle used for model validation (e) comparison of model voltage vs experimental voltage for a UDDS drive cycle.

Examining Figure 7-3 (a-c), it can be seen that for all four LFP cells, the same trend is observed for the parameters R_0, R_1 and C_1. In terms of the internal resistance R_0, it can be seen that the value

decreases as the SOC increases. The resistance in the RC pair, represented by R_1 was found to be constant while the capacitance in the RC pair, represented by C_1, was found to increase with as the SOC increases. The variation in the parameters for the four LFP cells was used to generate the varying ECM parameters for the cell change out simulator.

Urban Dynamometer Driving Schedule (UDDS), is a drive cycle that is used to represent driving conditions in the city. Since the change out concept will be used for an electric vehicle battery pack, it is important to validate the voltage response model using a drive cycle. Figure 7-3 (d), shows the current from a UDDS drive cycle that was applied to a new LFP battery. The experimental values obtained were compared to the values obtained from the ECM model. From Figure 7-3 (e), it can be seen that there is a good agreement between the model and experiment for the drive cycles. The maximum model error was calculated to be 1.56%. Although adding additional RC pairs would lower the model error, for the purpose of simulating cell change-out, these values were deemed to be adequate.

7.4.2 Cell Level Degradation

Having selected the degradation model proposed by Schmalstieg et al. [174], the model was parameterized to degradation rates found in the literature for LFP cells. Degradation rates were found to be highly varied, because the cycling conditions used by different sources were very different. Degradation rates found in the surveyed literature for cycling conditions similar to the simulation (1C current, 60% DOD) are summarized in Table 7-2.

Table 7-2: Summary of Relevant Degradation Rates for LFP Batteries

Cycling Conditions	**Cell Life (# of Cycles)**	**Source**
Current unspecified, 60% DOD	4000-5000	[32]
0.7C, 100% DOD	4000	[33]
2C, 50% DOD	3000-4000	[34]

For the purpose of this simulation, the approximate meantime to failure of the LFP cells was taken to be 4000 cycles. Given the rated capacity of the LFP cells (20Ah) and the DoD of the simulation cycles, this corresponded to 96000Ah of charge throughput. Ahmadi et al. [153] proposed an empirical capacity fade model based on charge throughput for constant cycling conditions. Collection of long-term degradation data was not in the scope of this work, which focuses on introducing the cell change-out concept and showing its feasibility

The predictive model proposed by Ahmadi et al. [153] was sufficient for the purposes of this paper as it adequately describes capacity fade in an electric vehicle until the capacity fade reaches 20%. Therefore parameters in the degradation model for capacity fade were determined by fitting the degradation equation shown in Equation (7-3) and (7-5) to the curve obtained Ahmadi et al. [153] using least-squares regression. The results are shown in Figure 7-4.

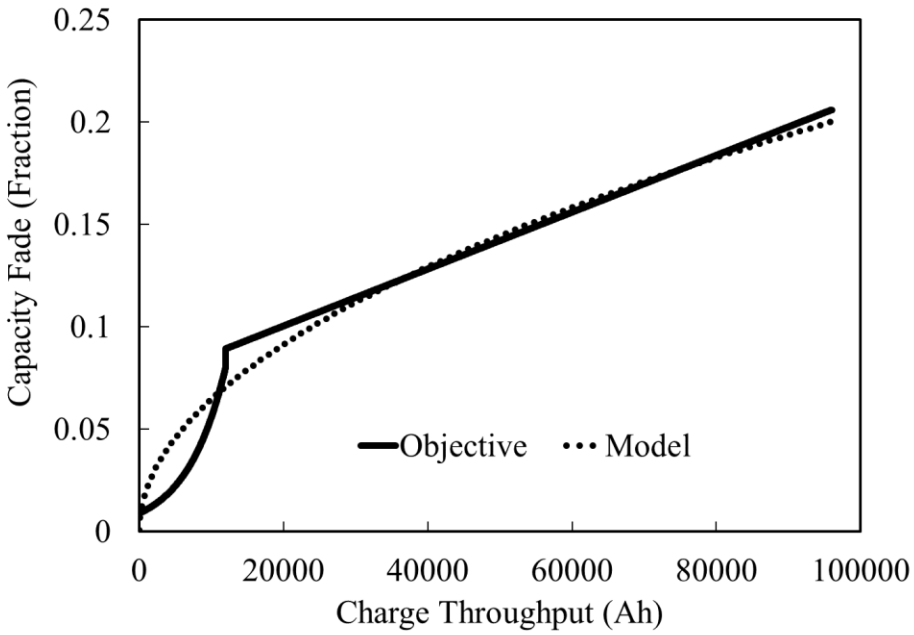

Figure 7-4: Parameterized degradation curve used in the model compared with the objective degradation function.

Although the model is not able to fully capture the initial exponential growth of the capacity prediction model, the two curves do align once the charge throughput is greater than 40,000 Ah, which is important as cell change out will normally occur towards the end of the cycle. In a similar way, the parameters for resistance increase can be identified according to LFP data from Zhang et

al. [28]. The estimated empirical parameters for capacity fade and resistance increase are described in Table 7-3 for LFP.

Table 7-3: Parameters for the LFP cell degradation model

Parameter	Capacity Fade	Resistance Rise	Units
a	0.00142	$2.780*10^{-5}$	$\sqrt{\mathrm{Ah} * \mathrm{V}}^{-1}$
b	3.274	3.199	V
c	0.00119	$-2.237*10^{-5}$	$\sqrt{\mathrm{Ah}}^{-1}$
d	$-9.219*10^{-4}$	$7.361*10^{-5}$	$\sqrt{\mathrm{Ah}}^{-1}$

The same approach can be applied for NMC/LMO cells, where the MTTF is 4000 cycles. The parameter values for the capacity fade and resistance increase models are summarized below.

Table 7-4: Parameters for the NMC/LMO cell degradation model

Parameter	Value
E_{ac}	$2.16*10^4$ [J mol^{-1}]
E_{ar}	$4.76*10^4$ [J mol^{-1}]
z	0.516
α_c	144.5 [Ah^{-z}]
β_c	420.1 [Ah^{-z}]
γ_c	$9.39*10^3$ [Ah^{-z}]
e	0.343
f	3
α_r	$3.46*10^5$ [Ah^{-z}]
β_c	$1.29*10^9$ [Ah^{-z}]
γ_r	$3.96*10^3$ [Ah^{-z}]
q	6
g	1.02
h	1.75
SOC_{0r}	0.228
CR_0	4.430

It should be noted that although it is possible to use the degradation model from [1] directly, the degradation model of [27] was used in this paper for three reasons.

1. One of the main goals of this paper is to provide a simulation framework for cell replacement that can be used by other researchers for understanding the feasibility of this concept for different battery chemistries. Part of this framework is selecting a degradation model that is computationally efficient and to illustrate how this model can be coupled with the voltage response model in order to simulate cell change out.
2. The degradation model that was selected has inputs of average voltage (or SOC) and depth of discharge, in addition to charge throughput. When degradation data is available, this model can be used to determine capacity fade under different operating conditions.
3. The chosen degradation model has fitted parameters a, b, c and d, which can be varied stochastically in order to generate variability among different batteries and these models can be coupled to power fade models.

7.4.3 Simulation Results – Variability in Degradation

One of the first simulations that will be discussed in this paper is the effect of variability in degradation rate on the cell change-out results. Depending on the type of battery and the battery pack manufacturer, there can be a significant difference in how quickly one cell degrades when compared to another. Therefore, the effect of varying degradation on the feasibility of cell change-out is a topic that needs to be addressed. This was investigated by changing the standard deviation of the distributions from which the degradation model parameters came from. Standard deviation of 10%, 5% and 2% of the mean value were tested.

As previously mentioned, the simulation of the battery pack was carried out for 40 cells for a total of 15,000 charge-discharge cycles between 20% and 80% SOC. The simulation protocol illustrated in Figure 7-2 was utilized in order to generate the simulation results. In this particular simulation, it was assumed that the battery pack is a “perfectly maintained system”, which means that the battery pack was checked continuously (or at a very small maintenance event interval) in order to determine whether one or more of the cells had degraded. The minimum capacity for which a cell will be replaced was taken to be 85% of its nominal capacity for this particular simulation.

The capacities of each individual cell, the pack capacity, the end-of-charge and end-of-discharge voltages, and the voltage profiles were recorded throughout the simulation. The charge throughput history of each cell was updated at the end of each cycle, as it is required for updating the degradation status of the cells.

The simulation results are summarized in Figure 7-5 below. The plot shows the SOH of the battery pack as a function contains three different simulations carried out with different variability in the degradation parameters. The MTTF of the cell was taken to be 4000 cycles for this simulation presented in this section. For the simulation results shown below, the total number of cells replaced was found to be 227, 235 and 238 for a percent deviation from the mean of 10%, 5% and 2% respectively.

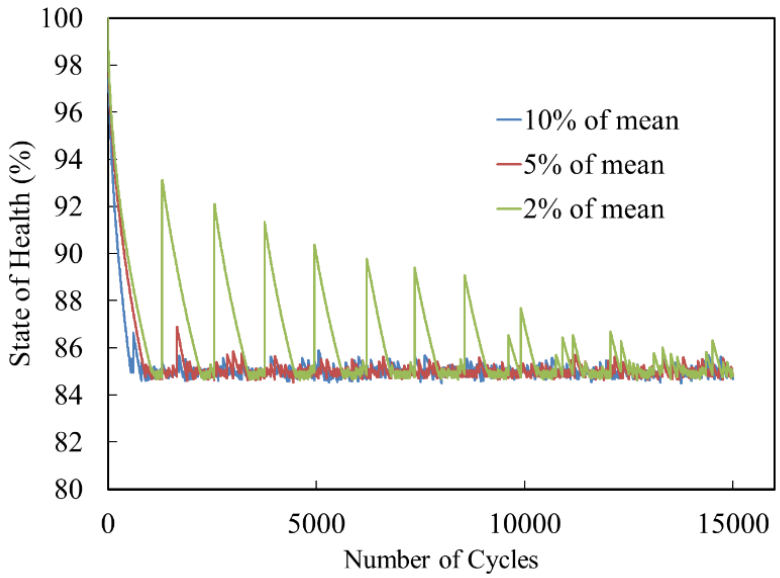

Figure 7-5: The effect of variability in the degradation parameters on the SOH of the battery pack during cell change out simulation.

Examining Figure 7-5, it can be seen that regardless of the variability in the cell degradation, the SOH of the battery pack reaches steady state after 15,000 cycles. These findings have been shown to hold true by [157], [158], who developed reliability models for the remanufacturing of a system with parts that can be replaced after failure. The results from this group showed that the average age of parts in a system can be maintained below their failure age indefinitely by remanufacturing. However, the findings by [157], [158] cannot necessarily be applied to the

battery pack since the capacity (analogous to age) of a serial battery pack is limited entirely by its weakest cell; the average age of the cells is not a consideration. Therefore, the findings from this study are important to EV manufacturers as it shows that by employing a cell replacement strategy, the state of the health of the battery pack can be maintained indefinitely.

The results from this simulation also show that regardless of what the variability in the cell degradation parameters, by using the cell change out concept, the SOH of the battery pack does not fall below 80%. A lower degree of variability results in larger oscillations in SOH as shown in Figure 7-5. This is due to the fact that a lower degree of variability means most of the cells will reach the maximum SOH value required for cell replacement at the same time, resulting in the large oscillations seen in Figure 7-5.

7.4.4 Simulation Results - Degradation Rate and Maintenance Event Interval

As previously mentioned, it is not possible to conduct cell change-out continuously as soon as one cell reaches its minimum capacity. Rather, the cell change out concept can only realistically be done at discrete intervals. The following section examines the relationship between the rate at which the cells degrade and how quickly the cells need to be replaced in order to ensure that the pack capacity does not drop below 80%. This is an important factor to considered for EV manufactures as this allows them to develop guidelines and how quickly the car needs to be taken in for service and what degree of degradation in the individual cell is acceptable.

Once again, the simulation of the battery pack was carried out by developing a battery pack of 40 cells in series and carried out a 1C charge/discharge for a total of 30,000 cycles. The first simulation was carried out for cells with a MTTF of 4,000 cycles. As noted previously, since the goal of cell change out concept is to ensure that the pack capacity does not fall below a minimal threshold value, it is important to change out the individual cells that are at a capacity higher than this value in order to ensure the pack SOH always remains above the threshold value. This higher threshold for the individual cells will be referred to as minimal cell capacity and a value of 15% capacity fade will be used in this simulation. The results are shown in the below.

Figure 7-6 (a) shows simulation results for cell change out for three different scenarios: when there is perfect replacement (replacement every 100 cycles), replacement every 1000 cycles and

replacement every 2000 cycles. The dashed line represents 80% SOH for the pack, where the battery pack normally has to be replaced.

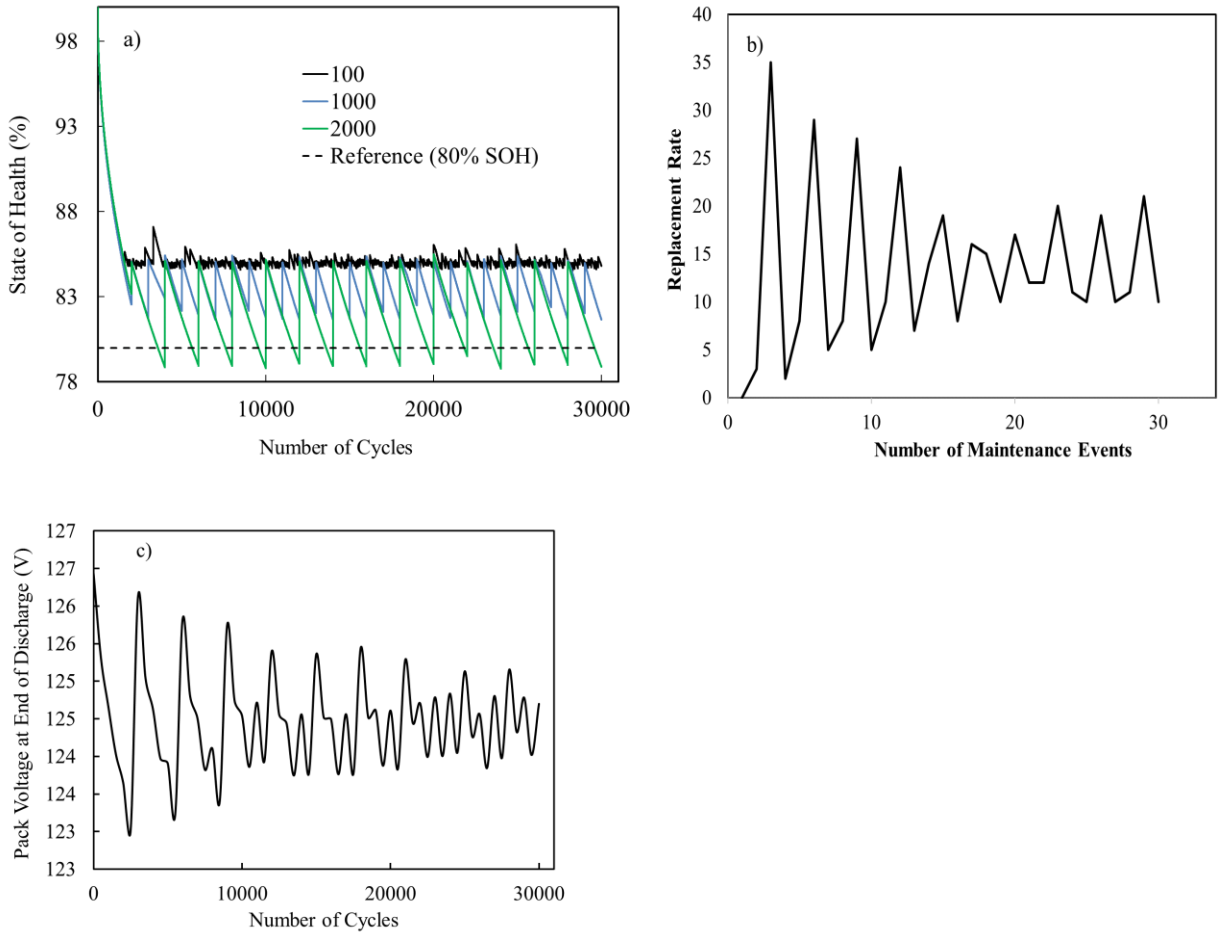

Figure 7-6: The simulated SOH for a battery pack that has a MTTF of 4000 cycles, where the cells are replaced at discrete intervals of 100, 1000 and 2000 cycles (b) The replacement rate (or number of cells replaced) during each maintenance event for a lithium ion battery pack with a MTTF of 4000 cycles and maintenance event interval of 2000 cycles (c) The pack voltage at the end of discharge for a Li-ion battery pack with a MTTF of 4000 cycles and maintenance event interval of 2000 cycles.

The results show that when the maintenance event interval is 1000 cycles, the battery pack is maintained at a SOH that is above the 80% mark. However, at 2000 cycles, the SOH value dips below the required threshold. Therefore, this means that for this particular battery chemistry and battery life, the degraded cells must be replaced at least at a discrete interval of 2000 cycles in

order to ensure the capacity fade of the battery pack does not exceed 20%. These results are important since they illustrate that by using simulation, car manufactures will be able to determine how quickly the battery pack in an electric vehicle needs to be serviced in order to prolong the pack life.

It is also important to consider the number of cells that need to be replaced during a maintenance event. Figure 7-6 (b) shows 30 consecutive maintenance events and the number of cells that have been replaced during each event. The results in Figure 7-6 (b) show that as the number of maintenance events increase, the number of cell that are replaced during these events appears to reach a steady state value.

In addition to capacity fade, the voltage of the battery pack will also decrease (power fade) as the battery is cycled. Figure 7-6 (c) shows the pack voltage at the end of discharge, recorded every 500 cycles. The initial decrease in voltage is due to an increase in resistance as the battery pack is cycled. The voltage of the battery pack increases when a maintenance event occurs where damaged batteries are replaced. Similar to the SOH of the battery, the pack voltage is found to reach a steady state value as the number of cycles increases.

The same simulation was carried out only this time the assumed MTTF of the cell was decreased to 2000 and 1000 cycles. The degradation data for an EV battery pack obtained by [153] was still utilized, only the data was scaled to match the lower MTTF of the cell. The results are shown in the two figures below.

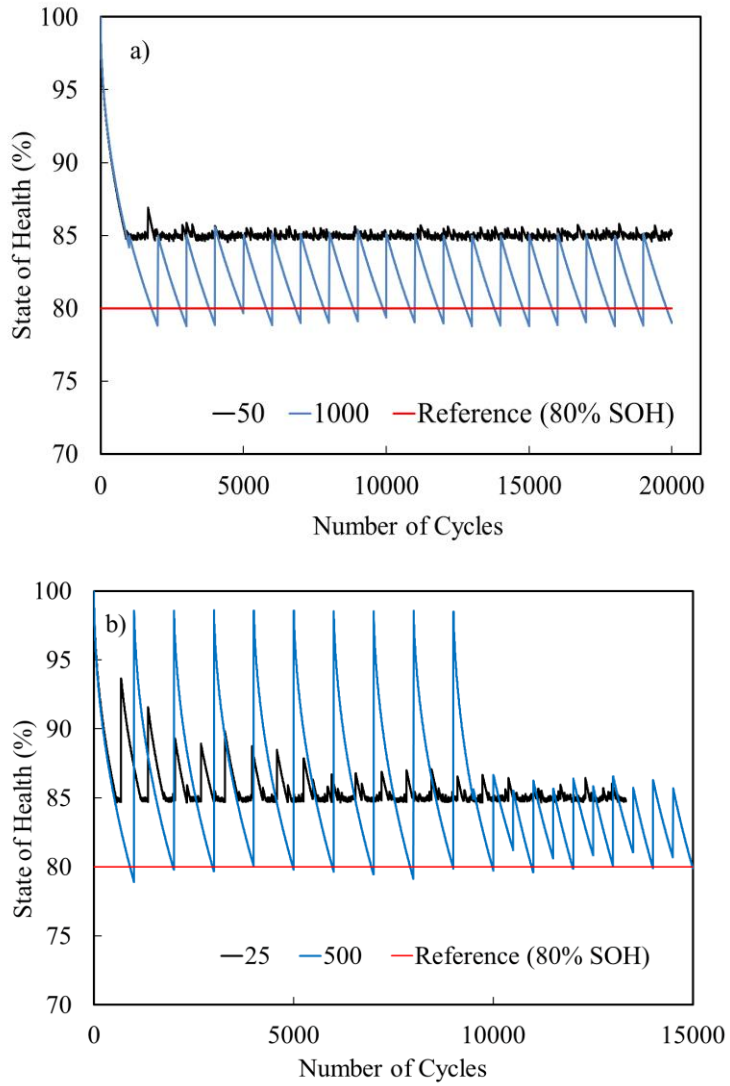

Figure 7-7: The simulated SOH for a battery pack that has a meantime to failure of (a) 2000 cycles, where the cells are replaced at discrete intervals of 50 and 1000 cycles (b) 1000 cycles, where the cells are replaced at discrete interval of 25 and 500 cycles.

When the meantime to failure of the cell is taken to be 2000 cycles, the minimum maintenance event interval also decreased to 1000 cycles. The trend holds when the MTTF is decreased even further to 1000 cycles, as shown in Figure 7-7, where at a maintenance event interval of 500 cycles the SOH dips below 80%. For this particular chemistry, it appears that a ratio of meantime to failure to maintenance interval of 2 is required in order to ensure the pack is able to meet its capacity demands.

These results from Figure 7-6 and Figure 7-7 show that in order to decrease the number of maintenance events (or the number of replaced batteries), the meantime to failure needs to be increased. The meantime to failure for a particular battery depends on the battery chemistry as well as the operating conditions under which the battery pack is used. Therefore, the simulator presented in this paper can be utilized to access the feasibility of a particular battery for cell change out. Also, discrete change-out of the individual cell at lower minimum capacity threshold is viable, where the EOL chosen should be tuned to the meantime to failure of the cell and how often the cell can be checked for replacement. If a longer monitoring interval is selected, an earlier cell EOL will be required.

7.4.5 Simulation Results – Comparison of LMC/NMC Chemistry

The simulation results described above were obtained for a battery pack primary composed on LFP battery cells. In order to test the robustness of the cell change out application for electric vehicles, the change out concept was implemented on a different chemistry; this time a mixed cathode chemistry of NMC/LMO. It is important to understand whether the trends obtained in the above section for LFP is observed for other battery chemistries such as NMC/LMO. The meantime to failure for NMC/LMO cells was deliberately chosen to be the same as that of LFP cells and the standard deviation used in generating the stochastic degradation parameters was also chosen to be 5% of mean for both cases. New parameters for the ECM were developed based on HPPC tests carried out for NMC/LMO cells and the degradation model shown in Equations (7-6) to (7-9) was applied.

The simulation was once again carried out for 30,000 cycles for the perfect replacement case as well as discrete replacement case. For the discrete replacement example, a maintenance event interval of 2000 cycle was used for checking to determine whether the individual cell needs to be replaced. The results are summarized below.

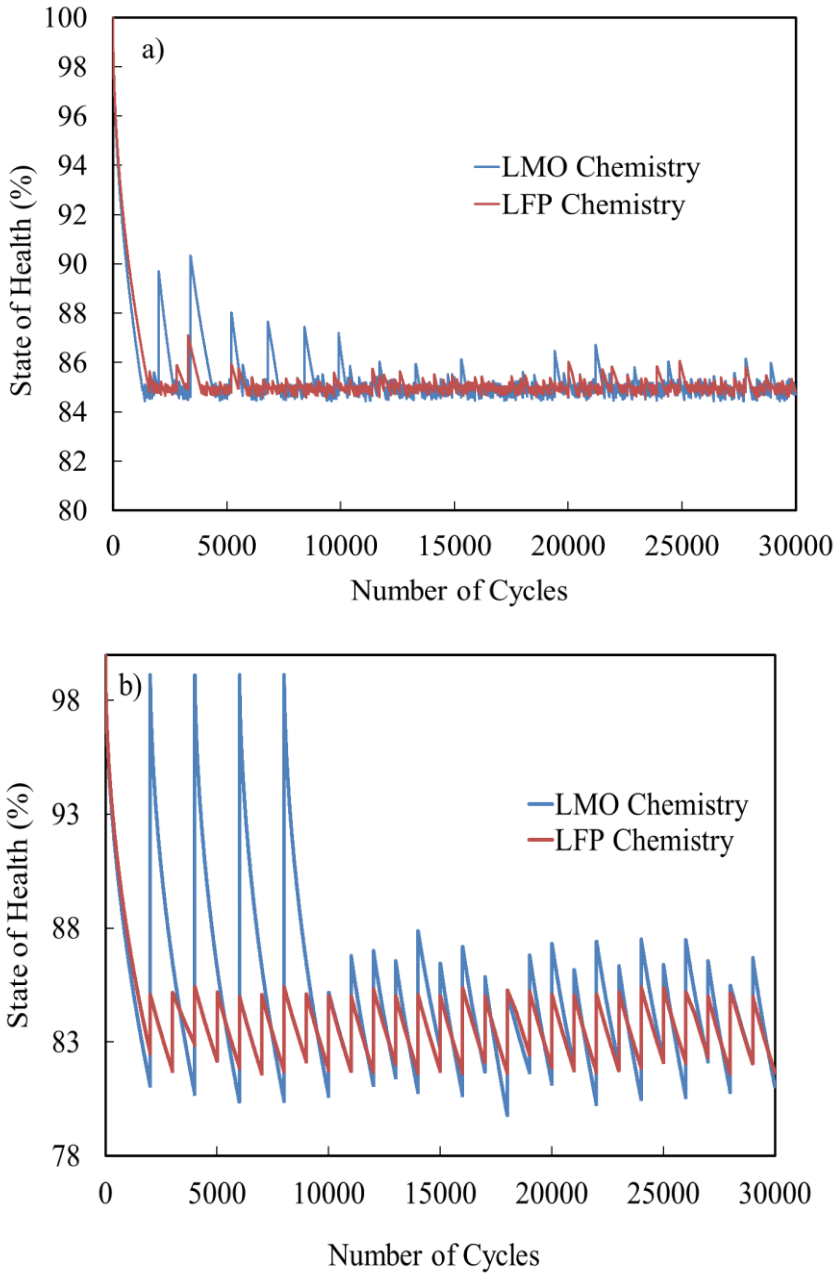

Figure 7-8: The simulated SOH for a battery pack that has battery cells with a chemistry of LFP and NMC/LMO for the (a) perfect replacement and (b) discrete replacement cycles.

The findings from Figure 7-8 show that regardless of the chemistry of the battery, the SOH of the battery pack does reach steady state if the pack undergoes regular maintenance events where degraded cells are replaced. How quickly the SOH reaches steady state differs between the two chemistries, and on the mean time to failure assumed for the cells. As Figure 7-8 shows,

NMC/LMO chemistry has a greater degree of oscillation and takes longer to reach its steady state value using cell change out. This is an important consideration since a larger degree of oscillations in the SOH of the battery pack can have implications on how quickly the cells need to be checked for replacement i.e. how high pack maintenance event should be. Finally, the results illustrate that the cell change out concept is able to maintain battery SOH indefinitely with regular maintenance events where degraded cells are changed out regardless of the battery chemistry.

Besides the somewhat common LFP and NMC/LMO battery chemistries, novel chemistries have been proposed in [35], [36]. While these Lithium-Vanadium and Sodium-based chemistries were not considered in this work, the fact that the ultimate result of the simulation was consistent between different degradation models and cathode chemistries suggests that the change-out concept would hold for any battery chemistry. The frequency of maintenance events and the SOH threshold for these would need to be adjusted for new battery types, an adjustment that would be based on eventual experimental data. Future work could be carried out by considering these new battery chemistries as well as other battery configurations such as prismatic and spiral wound cells.

It should be noted that the battery pack used in this study is composed of cells connected in series. Therefore, the overall performance of the battery pack was limited by the most degraded battery. The old batteries act as a limiter on how much of the new batteries' capacity is used during cycling. Future work will be carried out in developing a battery pack composed of multiple battery strings in parallel. When using such a battery pack, the interaction effect between a new and old battery would be greatest since the resistance rise in one string would lead to more current being diverted to other strings. Applying the cell change out concept for this particular battery pack would be something that will be considered in future works.

7.5 Conclusions

Various studies in literature have carried out simulations of battery packs, while few have discussed the concept of cell change-out. This paper attempts to combine the two concepts by creating a battery pack model and utilizing the model to understand the concept of cell change-out. The battery pack model is developed by modeling each individual cell using a Thevenin equivalent circuit and an empirical degradation model. The individual cell parameters in the voltage response model as well as the parameters in the degradation model can vary stochastically in the simulation. The individual cells that have degraded below 80% capacity in the simulation

are changed out during maintenance events resulting in an overall cell replacement rate that appears to reach steady state as the number of maintenance events increase. The overall pack performance also reaches a steady state with the replacement of individual degraded cells during maintenance events. The paper provides a simulation framework for conducting cell change out and from the simulation results, the following conclusions can be observed:

- By changing out individual cells that have dropped below their minimum capacity, the overall SOH of the battery pack can be maintained indefinitely above a target specification of 80% pack capacity;
- The maintenance event rate at which the cells are replaced is directly related to the average mean time to failure assumed for the individual cells which is simulated using stochastic parameters. As expected a higher mean time to failure results in a longer period between maintenance events required to maintain the SOH. Therefore, by using the simulation protocol outlined in this paper, the optimal maintenance period for a particular pack can be established;
- The results show that regardless of the chemistry, the cell change out concept will result in a battery pack that reaches steady state performance with regular maintenance.

The contributions from this paper illustrates that if at some point the concept of cell change-out does become economically feasible, applying this approach would ensure that the battery pack operates for a much longer period of time in service.

Chapter 8: Conclusions and Recommendations

8.1 Conclusions and Contributions

The focus of this work has been on the development of algorithms for pack state-of-charge (SOC) and state-of-health (SOH) estimation along with the advancement of simulation tools for modeling battery and pack dynamics. The following sections summarizes the five main research contributions from this thesis, one from each chapter.

8.1.1 Contribution to Battery Modeling

The ability to predict battery behavior at various operating conditions and for different battery chemistries is an essential tool in generating robust SOC and SOH algorithms. Development of these models often requires complex modeling software, in the case of electrochemical models, or conducting a large number of experiments, which is often the case for equivalent circuit models (ECM). Therefore, the first contribution of this thesis is the building of a characterization protocol that requires a minimal number of steps. A face-centered central composite design (CCD) was utilized in order to extract as much information as possible about the ECM parameter response surface. A more in-depth statistical analysis was conducted, where replicate runs were utilized for estimating the noise variance. The model was then incorporated into a comprehensive battery simulator and the results show that the developed algorithm can accurately estimate both the voltage and temperature of the battery under various conditions. Furthermore, the prediction error, using the proposed approach was compared with existing techniques. The results show that by using the design of experiments (DOE) approach, the same degree of accuracy can be obtained while significantly reducing the required characterization time. This new model identification protocol can be used by future battery management system (BMS) developers as a tool for characterizing and modeling a battery in a short period of time.

8.1.2 Contribution to Resistance Estimation

Resistance estimation algorithms in literature normally involve modeling the battery, using some sort of ECM, and updating the model parameters in real-time. The ohmic resistance is then used for predicting the health of the Li-Ion battery. Although this approach works for a single cell, it can be challenging when implementing the algorithm for a large battery pack. Model parameters,

error co-variances matrices and algorithm parameters needs to be stored for each individual cell and the algorithm also needs to be executed at the cell level. Therefore, this research examined the feasibility of using a simple direct resistance estimation (DRE) approach for identifying problematic cells in the pack. The developed algorithm uses a moving window to search for rapid changes in the current and voltage and it estimates the resistance only when a significant change in these measurements is observed. In addition, an exponentially weighted moving average (EWMA) filter was utilized for filtering measurement noise and obtaining a smoother signal. This approach was compared to more advanced techniques such as the EKF and RLS. It was shown that while all three algorithms produced similar results, the direct resistance algorithm required significantly less computational time. Therefore, the second research contribution is a resistance estimation algorithm that is not only accurate but is computationally efficient enough for execution on an embedded platform.

8.1.3 Contribution to State-of-Health Estimation

Although a number of publications in literature attempt to determine the internal resistance of the battery, few papers examine how to convert these estimates into a stable SOH metric. A number of challenges can arise, including outlier resistance estimates, noisy data and the dependence of battery resistance on temperature and SOC. An adaptive control chart was applied to remove outliers present in the resistance data. In addition, variation in the estimated SOH was minimized by filtering the internal resistance, based on a small temperature and SOC window, and passing the values through an EWMA filter. The results show a good agreement between the proposed approach and HPPC data over a period of 27 days, with an average error of 1.1%. The contributions from this research can help advance the implementation of SOH techniques on the BMS.

8.1.4 Contribution to State-of-Charge Estimation

Estimation of SOC for a large battery pack is still a challenging topic for commercial applications. The algorithm needs to be accurate, while being computationally efficient for implementation on a micro-processor. The proposed technique needs to account for imbalance in SOC among the cells and for variation in cell model parameters. In addition, the algorithm needs to behave logically to the battery user. To address these concerns, a comprehensive SOC algorithm was proposed. A RLS approach was used to estimate model parameters, while an EKF technique was applied for updating the SOC. A novel adaptive coulomb counting algorithm is proposed to ensure

logical behavior of the li-ion battery. Unlike previous approaches, this algorithm was applied to both the *min* and *max* cell within the pack to evaluate its performance under a variety of different conditions. Results show that the algorithm is able to remove current offset and behave logically even when the battery pack is unbalanced. It is hoped these results will advance research in the area of SOC estimation at the pack level.

8.1.5 Contribution to Simulation of Cell Replacement

The concept of cell replacement, where an aged cell or module is replaced within a pack, is a relatively new idea. Currently, no work exists in literature that has examined the effects of changing out an aged cell within the battery pack. Therefore, the final contribution of this thesis is the development of a pack simulator that can predict the pack SOH as old cells are changed out. The findings indicate that the overall SOH can be maintained above a certain threshold value. In addition, the simulation framework can be used to determine the optimal maintenance period for a particular pack. The approach presented in this work can be used by battery manufacturers to develop optimal battery pack design.

8.2 Recommendations and Future Work

Although this work has started to explore the subtle details of pack-level SOC and SOH estimation, a significant amount of work still needs to be carried out in this area. The following points are offered to aid future research.

- The regression approach describe in Chapter 3 consists of two-stages; the first stage estimates battery parameters which are subsequently used in the second stage as dependent variables. The regression approach carried out in this research can be used if the variance is assumed to be homogenous. In situations, where a non-constant variance is observed, a more advanced regression approach is required, such as weight least squares. Therefore, in future works a more detailed statistical analysis can be conducted for the equivalent circuit parameter model, in order to ensure these assumptions are valid.

- In this work, the ECM parameter surface was only assumed to change with temperature and SOC. For future work, the battery degradation can be considered as a third factor and the design-of-experiments approach can be extended to include this additional variable. A

central composed design can be constructed with rotatable properties in order to ensure equal prediction variance in all directions. Two cells with varying SOH values will be used to validate the model prediction.

- Although the ohmic resistance provides insights into the degradation of the cell, the estimated value can be incorrect if the battery pack has additional resistance elements. For example, an eroded bus-bar can indicate a high cell resistance, when the problem lies with the cell connectors. Therefore, future work needs to be carried out in determining the optimal way to account for cell-to-cell tab resistance. One approach is to carry out a base-line after the battery pack is installed. The increase in resistance over time is then compared to this base-line value. This approach can be used to eliminate, to a certain degree, the effect of bus-bar resistance.

- In this work, the *min* and *max* cells were identified using the maximum and minimal terminal voltage. This approach works for a fresh pack that is unbalanced or an aged pack that is balanced. Research is still required to access the feasibility of using this approach on an unbalanced pack with significant degradation. One approach is to carry out SOC estimation on a different time scale than updating battery resistance parameters. This prevents divergence issues that could occur due to the coupled estimation of a large number of parameters. Upon estimation of the battery capacity and resistance, the *min* and *max* cell could be determined and an SOC estimation algorithm can be executed. The method described here assumes that capacity and resistance does not change in a period of days, a condition which is often found to be valid.

- Battery hysteresis is a term that was briefly introduced in this thesis but was not incorporated into the battery model. The hysteresis effect has been shown to be significant for lithium iron phosphate (LFP) batteries [178]–[180] and accurately modeling this behavior has been shown to improve the accuracy of the SOC estimation algorithm. Therefore, additional research can be carried out in developing new ways to incorporate hysteresis into the SOC estimation framework. Research is also required in constructing well-designed current profiles that can be used to identify the hysteresis parameters. The

hybrid-pulse power characterization test that is commonly used, might not be sufficient in all cases.

- Research can also be carried out to expand on the cell replacement simulation by examining the economic feasibility of this concept. Economic analysis could explore under what conditions (if any) replacement of the cell can be profitable for battery manufactures. In addition, there are a large number of degradation models available in literature, for a variety of different chemistries. By incorporating these models into the simulation framework developed in this research, conclusions can be made on the optimal chemistry and configuration for an electric vehicle battery pack. The simulation results will also provide insights into what are considered optimal servicing intervals for a particular battery chemistry.

References

[1] J. . Tarascon and M. Armand, “Issues and challenges facing rechargeable lithium batteries,” *Nature*, vol. 414, no. November, pp. 359–367, 2001.

[2] L. Huat, Y. Ye, and A. A. O. Tay, “Integration issues of lithium-ion battery into electric vehicles battery pack,” *J. Clean. Prod.*, vol. 113, pp. 1032–1045, 2016.

[3] S. Manzetti and F. Mariasiu, “Electric vehicle battery technologies : From present state to future systems,” *Renew. Sustain. Energy Rev.*, vol. 51, pp. 1004–1012, 2015.

[4] J. Eyer and G. Corey, “Energy Storage for the Electricity Grid : Benefits and Market Potential Assessment Guide A Study for the DOE Energy Storage Systems Program,” *Sandia Rep.*, 2010.

[5] H. Rahimi-eichi, U. Ojha, F. Baronti, and C. Mo-Yuen, “Battery Management System: An Overview of Its Applications in Smart Grid and Elctric Vehicles,” *IEEE Ind. Electron. Mag.*, pp. 4–16, 2013.

[6] R. Milan, “STATIONARY STORAGE AND AUTOMOTIVE Li-ion BATTERY PACKS,” *Yole Development*, 2016. [Online]. Available: https://www.i-micronews.com/report/product/stationary-storage-and-automotive-li-ion-battery-packs.html#companies-cited.

[7] M. Ye, H. Guo, and B. Cao, “A model-based adaptive state of charge estimator for a lithium-ion battery using an improved adaptive particle filter,” *Appl. Energy*, vol. 190, pp. 740–748, 2017.

[8] Y. Wang, C. Zhang, and Z. Chen, “On-line battery state-of-charge estimation based on an integrated estimator,” *Appl. Energy*, vol. 185, pp. 2026–2032, 2017.

[9] Z. Wei, J. Zhao, D. Ji, and K. Jet, “A multi-timescale estimator for battery state of charge and capacity dual estimation based on an online identified model q,” *Appl. Energy*, vol. 204, pp. 1264–1274, 2017.

[10] Z. Wei, K. Jet, N. Wai, T. Mariana, and M. Skyllas-kazacos, “Adaptive estimation of state of charge and capacity with online identified battery model for vanadium redox flow battery,” *J. Power Sources*, vol. 332, pp. 389–398, 2016.

[11] H. Mu, R. Xiong, H. Zheng, Y. Chang, and Z. Chen, “A novel fractional order model based state-of-charge estimation method for lithium-ion battery,” *Appl. Energy*, vol. 207, pp. 384–393, 2017.

[12] H. Sheng and J. Xiao, “Electric vehicle state of charge estimation: Nonlinear correlation and fuzzy support vector machine,” *J. Power Sources*, vol. 281, pp. 131–137, 2015.

[13] C. Burgos, S. Doris, M. E. Orchard, and C. Roberto, “Fuzzy modelling for the state-of-charge estimation of lead-acid batteries,” *J. Power Sources*, vol. 274, pp. 355–366, 2015.

[14] H. Chaoui and C. C. Ibe-ekeocha, “State of Charge and State of Health Estimation for Lithium Batteries Using Recurrent Neural Networks,” *IEEE Trans. Veh. Technol.*, vol. 66, no. 10, pp. 8773–8783, 2017.

[15] H. Chaoui, C. C. Ibe-ekeocha, and H. Gualous, “Aging prediction and state of charge estimation of a LiFePO 4 battery using input time-delayed neural networks,” *Electr. Power Syst. Res.*, vol. 146, pp. 189–197, 2017.

[16] X. Dang, L. Yan, K. Xu, X. Wu, H. Jiang, and H. Sun, “Open-Circuit Voltage-Based State of Charge Estimation of Lithium-ion Battery Using Dual Neural Network Fusion Battery Model,” *Electrochim. Acta*, vol. 188, pp. 356–366, 2016.

[17] Z. Wei, C. Zoi, B. H. Soong, and K. J. Tseng, “Online Model Identification and State-of-Charge Estimate for Lithium-Ion Battery With a Recursive Total Least Squares-Based Observer,” *1336 IEEE Trans. Ind. Electron.*, vol. 65, no. 2, pp. 1336–1346, 2018.

[18] Z. Wei, S. Meng, B. Xiong, D. Ji, and K. J. Tseng, “Enhanced online model identification and state of charge estimation for lithium-ion battery with a FBCRLS based observer,” *Appl. Energy*, vol. 181, pp. 332–341, 2016.

[19] C. Zou, C. Manzie, D. Nesic, and A. G. Kallapur, “Multi-time-scale observer design for state-of-charge and state-of-health of a lithium-ion battery,” *J. Power Sources*, vol. 335, pp. 121–130, 2016.

[20] B. Xia, C. Chen, Y. Tian, W. Sun, Z. Xu, and W. Zheng, “A novel method for state of charge estimation of lithium-ion batteries using a nonlinear observer,” *J. Power Sources*, vol. 270, pp. 359–366, 2014.

[21] L. Zhong, C. Zhang, Y. He, and Z. Chen, “A method for the estimation of the battery pack state of charge based on in-pack cells uniformity analysis,” *Appl. Energy*, vol. 113, pp. 558–564, 2014.

[22] M. Farkhondeh, M. Pritzker, M. Fowler, and C. Delacourt, “Electrochemistry Communications Transport property measurement of binary electrolytes using a four-electrode electrochemical cell,” *Electrochem. commun.*, vol. 67, pp. 11–15, 2016.

[23] M. Mastali, M. Farkhondeh, S. Farhad, R. A. Fraser, and M. Fowler, “Electrochemical Modeling of Commercial LiFePO 4 and Graphite Electrodes : Kinetic and Transport Properties and Their Temperature Dependence,” *J. Electrochem. Soc.*, vol. 163, no. 13, 2016.

[24] M. Farkhondeh, M. Pritzker, M. Fowler, and C. Delacourt, “Mesoscopic Modeling of a LiFePO 4 Electrode : Experimental Validation under Continuous and Intermittent Operating,” vol. 164, no. 11, pp. 3040–3053, 2017.

[25] N. Damay, C. Forgez, M. P. Bichat, and G. Friedrich, “Thermal modeling of large prismatic LiFePO4/graphite battery. Coupled thermal and heat generation models for characterization and simulation,” *J. Power Sources*, vol. 283, pp. 37–45, 2015.

[26] X. Lin *et al.*, “A lumped-parameter electro-thermal model for cylindrical batteries,” *J.*

Power Sources, vol. 257, pp. 1–11, Jul. 2014.

[27] L. H. Saw, K. Somasundaram, Y. Ye, and A. A. O. Tay, "Electro-thermal analysis of Lithium Iron Phosphate battery for electric vehicles," *J. Power Sources*, vol. 249, pp. 231–238, 2014.

[28] M. Mastali, S. Farhad, M. Farkhondeh, R. A. Fraser, and M. Fowler, "Simplified electrochemical multi-particle model for LiFePO 4 cathodes in lithium-ion batteries," *J. Power Sources*, vol. 275, pp. 633–643, 2015.

[29] R. Ahmed, M. El Sayed, I. Arasaratnam, J. Tjong, and S. Habibi, "Reduced-Order Electrochemical Model Parameters Identification and SOC Estimation for Healthy and Aged Li-Ion Batteries Part I: Parameterization Model Development for Healthy Batteries," *IEEE J. Emerg. Sel. Top. Power Electron.*, vol. 2, no. 3, pp. 659–677, Sep. 2014.

[30] R. Ahmed, S. Member, M. El Sayed, I. Arasaratnam, J. Tjong, and S. Habibi, "Reduced-Order Electrochemical Model Parameters Identification and SOC Estimation for Healthy and Aged Li-Ion Batteries Part I : Parameterization Model Development for Healthy Batteries," vol. 2, no. 3, pp. 659–677, 2014.

[31] D. Linden and T. Reddy, *Handbook of Batteries*, Third Edit. New York: McGraw-Hill, 2001.

[32] V. Pop, H. Jan Bergveld, D. Danilov, P. Regtien, and P. Notten, *Battery Management Systems: Accurate State-of-Charge Indication for Battery-Powered Applications*. London, 2008.

[33] G. L. Plett, "Extended Kalman filtering for battery management systems of LiPB-based HEV battery packs," *J. Power Sources*, vol. 134, no. 2, pp. 277–292, Aug. 2004.

[34] F. Sun, R. Xiong, and H. He, "Estimation of state-of-charge and state-of-power capability of lithium-ion battery considering varying health conditions," *J. Power Sources*, vol. 259, pp. 166–176, Aug. 2014.

[35] J. Remmlinger, M. Buchholz, M. Meiler, P. Bernreuter, and K. Dietmayer, "State-of-health monitoring of lithium-ion batteries in electric vehicles by on-board internal resistance estimation," *J. Power Sources*, vol. 196, no. 12, pp. 5357–5363, Jun. 2011.

[36] X. Hu, S. Li, and H. Peng, "A comparative study of equivalent circuit models for Li-ion batteries," *J. Power Sources*, vol. 198, pp. 359–367, Jan. 2012.

[37] A. Seaman, T. S. Dao, and J. McPhee, "A survey of mathematics-based equivalent-circuit and electrochemical battery models for hybrid and electric vehicle simulation," *J. Power Sources*, vol. 256, pp. 410–423, 2014.

[38] Liaw, Jungst, and Doughty, "Modeling of lithium ion cells?A simple equivalent-circuit model approach," *Solid State Ionics*, vol. 175, no. 1–4, pp. 835–839, Nov. 2004.

[39] J. Newman and W. Tiedeman, "Porous-Electrode Theory with Battery Applications," *Am.*

Inst. Chem. Eng., vol. 21, no. 1, pp. 25–41, 1975.

[40] G. L. Plett, "Extended Kalman filtering for battery management systems of LiPB-based HEV battery packs," *J. Power Sources*, vol. 134, no. 2.

[41] M. Kassem, J. Bernard, R. Revel, S. Pélissier, F. Duclaud, and C. Delacourt, "Calendar aging of a graphite / LiFePO 4 cell," *J. Power Sources*, vol. 208, pp. 296–305, 2012.

[42] S. Grolleau *et al.*, "Calendar aging of commercial graphite/LiFePO4 cell – Predicting capacity fade under time dependent storage conditions," *J. Power Sources*, vol. 255, pp. 450–458, 2014.

[43] M. Broussely *et al.*, "Main aging mechanisms in Li ion batteries," *J. Power Sources*, vol. 146, no. 1–2, pp. 90–96, Aug. 2005.

[44] J. Vetter *et al.*, "Ageing mechanisms in lithium-ion batteries," *J. Power Sources*, vol. 147, no. 1–2, pp. 269–281, Sep. 2005.

[45] Q. Badey, G. Cherouvrier, Y. Reynier, M. Duffault, J, and S. Franger, "Ageing forecast of lithium- ion batteries for electric and hybrid vehicles," *Curr. Top. Electrochem.*, vol. 16, pp. 65–79, 2011.

[46] M. Safari and C. Delacourt, "Aging of a Commercial Graphite/LiFePO4 Cell," *J. Electrochem. Soc.*, vol. 158, no. 10, p. A1123, 2011.

[47] V. Agubra and J. Fergus, "Lithium Ion Battery Anode Aging Mechanisms," *Materials (Basel).*, vol. 6, no. 4, pp. 1310–1325, Mar. 2013.

[48] V. Pop, H. J. Bergveld, D. Dmitry, and P. Notten, "Adaptive State-of-Charge Indication System for Li-ion Battery-Powered Devices," *World Electr. Veh. Assoc. J.*, vol. 1, no. May 2014, pp. 38–45, 2007.

[49] X. Zhang, X. Tang, X. Lin, Y. Zhang, M. A. Salman, and C. Y. K, "Method for Battery Capacity Estimation," US 8084996, 2011.

[50] M. A. Roscher, J. Assfalg, and O. S. Bohlen, "Detection of Utilizable Capacity Deterioration in Battery Systems," *IEEE Trans. Veh. Technol.*, vol. 60, no. 1, pp. 98–103, 2011.

[51] X. Jin *et al.*, "System and Method of Battery Capacity Estimation," US 7418356 B2, 2004.

[52] B. S. Bhangu, P. Bentley, D. A. Stone, and C. M. Bingham, "Nonlinear Observers for Predicting State-of-Charge and State-of-Health of Lead-Acid Batteries for Hybrid-Electric Vehicles," *IEEE Trans. Veh. Technol.*, vol. 54, no. 3, pp. 783–794, 2005.

[53] B. S. B. P. Bentley, D. A. Stone, and C. M. Bingham, "State-of-Charge and State-of-Health prediction of Lead-acid Batteries for Hybrid Electric Vehicles using non-linear observers Keywords Abstract," *Proc. Eur. Conf. Power Electron. Appl.*, pp. 1–10, 2005.

[54] F. Zhang, G. Liu, S. Member, and L. Fang, "Battery State Estimation Using Unscented

Kalman Filter," *IEEE Int. Conf. Robot. Autom.*, pp. 1863–1868, 2009.

[55] X. Tang, X. Mao, J. Lin, and B. Koch, "Li-ion Battery Parameter Estimation for State of Charge," in *American Control Conference*, 2011.

[56] X. Tang, Y. Zhang, A. C, B. Frisch, and B. J. K. L. R., "Dynamic Battery Capacity Estimation," US 2012/0136594 A1, 2012.

[57] C. Hu, B. D. Youn, and J. Chung, "A multiscale framework with extended Kalman filter for lithium-ion battery SOC and capacity estimation," *Appl. Energy*, vol. 92, pp. 694–704, 2012.

[58] S. Lee, J. Kim, J. Lee, and B. H. Cho, "State-of-charge and capacity estimation of lithium-ion battery using a new open-circuit voltage versus state-of-charge," *J. Power Sources*, vol. 185, pp. 1367–1373, 2008.

[59] G. L. Plett, "Sigma-point Kalman filtering for battery management systems of LiPB-based HEV battery packs Part 2 : Simultaneous state and parameter estimation," *J. Power Sources*, vol. 161, pp. 1369–1384, 2006.

[60] M. Einhorn, F. V. Conte, C. Kral, S. Member, and J. Fleig, "A Method for Online Capacity Estimation of Lithium Ion Battery Cells Using the State of Charge and the Transferred Charge," *IEEE Trans. Ind. Appl.*, vol. 48, no. 2, pp. 736–741, 2012.

[61] C. Weng, Y. Cui, J. Sun, and H. Peng, "On-board state of health monitoring of lithium-ion batteries using incremental capacity analysis with support vector regression," *J. Power Sources*, vol. 235, pp. 36–44, 2013.

[62] A. Millner, "Modeling Lithium Ion battery degradation in electric vehicles," in *2010 IEEE Conference on Innovative Technologies for an Efficient and Reliable Electricity Supply*, 2010, pp. 349–356.

[63] K. S. Champlin, "Method and Apparatus for Determining Battery Properties from Complex Impedance/Admittance," US 6037777, 2000.

[64] K. S. Champlin and K. Bertness, "A Fundamentally New Approach to Battery Performance Analysis Using DFRATM / DFISTM Technology," *Proc. 22nd Int. Telecom- munications Energy Conf.*, pp. 348–355, 2000.

[65] B. S. Bhangu, P. Bentley, D. A. Stone, and C. M. Bingham, "Observer techniques for estimating the State-of-Charge and State-of-Health of VRLABs for Hybrid Electric Vehicles," in *2005 IEEE Vehicle Power and Propulsion Conference*, 2005, pp. 780–789.

[66] I. Kim, "A Technique for Estimating the State of Health of Lithium Batteries Through a Dual-Sliding-Mode Observer," *EEE Trans. POWER Electron.*, vol. 25, no. 4, pp. 1013–1022, 2010.

[67] Y. Chiang and W. Sean, "Dynamical Estimation of State-of-Health of Batteries by Using Adaptive Observer," *2nd Int. Conf. Power Electron. Intell. Transp. Syst.*, 2009.

[68] D. Mu, J. Jiang, and C. Zhang, “Online Semiparametric Identification of Lithium-Ion Batteries Using the Wavelet-Based Partially Linear Battery Model,” *Energies*, vol. 6, pp. 2583–2604, 2013.

[69] W.-Y. Chang, “The State of Charge Estimating Methods for Battery: A Review.,” *ISRN Appl. Math.*, pp. 1–7, 2013.

[70] W. Waag, C. Fleischer, and D. U. Sauer, “Critical review of the methods for monitoring of lithium-ion batteries in electric and hybrid vehicles,” *J. Power Sources*, vol. 258, pp. 321–339, Jul. 2014.

[71] M. A. Hannan, M. S. H. Lipu, A. Hussain, and A. Mohamed, “A review of lithium-ion battery state of charge estimation and management system in electric vehicle applications : Challenges and recommendations,” *Renew. Sustain. Energy Rev.*, vol. 78, no. August 2016, pp. 834–854, 2017.

[72] Z. Li, J. Huang, B. Y. Liaw, and J. Zhang, “On state-of-charge determination for lithium-ion batteries,” *J. Power Sources*, vol. 348, pp. 281–301, Apr. 2017.

[73] G. L. Plett, “Extended Kalman filtering for battery management systems of LiPB-based HEV battery packs,” *J. Power Sources*, vol. 134, no. 2, pp. 262–276, Aug. 2004.

[74] G. L. Plett, “Extended Kalman filtering for battery management systems of LiPB-based HEV battery packs,” *J. Power Sources*, vol. 134, no. 2, pp. 252–261, Aug. 2004.

[75] S. Sepasi, L. Roose, and M. Matsuura, “Extended Kalman Filter with a Fuzzy Method for Accurate Battery Pack State of Charge Estimation,” *Energies*, vol. 8, no. 6, pp. 5217–5233, Jun. 2015.

[76] R. Xiong, F. Sun, Z. Chen, and H. He, “A data-driven multi-scale extended Kalman filtering based parameter and state estimation approach of lithium-ion olymer battery in electric vehicles,” *Appl. Energy*, vol. 113, pp. 463–476, 2014.

[77] R. Xiong, X. Gong, C. C. Mi, and F. Sun, “A robust state-of-charge estimator for multiple types of lithium-ion batteries using adaptive extended Kalman filter,” *J. Power Sources*, vol. 243, pp. 805–816, 2013.

[78] M. Mastali, J. Vazquez-Arenas, R. Fraser, M. Fowler, S. Afshar, and M. Stevens, “Battery state of the charge estimation using Kalman filtering,” *J. Power Sources*, vol. 239, pp. 294–307, 2013.

[79] S. Sepasi, R. Ghorbani, and B. Y. Liaw, “SOC estimation for aged lithium-ion batteries using model adaptive extended Kalman filter,” in *2013 IEEE Transportation Electrification Conference and Expo (ITEC)*, 2013, pp. 1–6.

[80] R. Xiong, F. Sun, H. He, and T. D. Nguyen, “A data-driven adaptive state of charge and power capability joint estimator of lithium-ion polymer battery used in electric vehicles,” *Energy*, vol. 63, pp. 295–308, 2013.

[81] F. Sun, X. Hu, Y. Zou, and S. Li, “Adaptive unscented Kalman filtering for state of charge

estimation of a lithium-ion battery for electric vehicles," *Energy*, vol. 36, pp. 3531–3540, 2011.

[82] H. He, R. Xiong, and J. Peng, "Real-time estimation of battery state-of-charge with unscented Kalman filter and RTOS μCOS-II platform," *Appl. Energy*, vol. 162, pp. 1410–1418, 2016.

[83] W. He, N. Williard, C. Chen, and M. Pecht, "State of charge estimation for electric vehicle batteries using unscented kalman filtering," *Microelectron. Reliab.*, vol. 53, no. 6, pp. 840–847, Jun. 2013.

[84] G. L. Plett, "Sigma-point Kalman filtering for battery management systems of LiPB-based HEV battery packs Part 1 : Introduction and state estimation," *J. Power Sources*, vol. 161, pp. 1356–1368, 2006.

[85] Y. Wang, C. Zhang, and Z. Chen, "A method for state-of-charge estimation of LiFePO4 batteries at dynamic currents and temperatures using particle filter," *J. Power Sources*, vol. 279, pp. 306–311, 2015.

[86] S. Schwunk, N. Armbruster, S. Straub, J. Kehl, and M. Vetter, "Particle filter for state of charge and state of health estimation for lithium–iron phosphate batteries," *J. Power Sources*, vol. 239, pp. 705–710, 2013.

[87] C. Cai, D. Du, Z. Liu, and J. Ge, "State-of-Charge (SOC) Estimation of High Power Ni-MH Rechargable Battery With Artificial Neural Network," *Proc. 9th Int. Conf. Neural Inf. Process.*, vol. 2, pp. 824–828, 2002.

[88] W. He, N. Williard, C. Chen, and M. Pecht, "State of charge estimation for Li-ion batteries using neural network modeling and unscented Kalman filter-based error cancellation," *Int. J. Electr. Power Energy Syst.*, vol. 62, pp. 783–791, 2014.

[89] X. Chen, W. Shen, M. Dai, Z. Cao, J. Jin, and A. Kapoor, "Robust Adaptive Sliding-Mode Observer Using RBF Neural Network for Lithium-Ion Battery State of Charge Estimation in Electric Vehicles," *IEEE Trans. Veh. Technol.*, vol. 65, no. 4, pp. 1936–1947, 2016.

[90] M. A. Awadallah and B. Venkatesh, "Accuracy improvement of SOC estimation in lithium-ion batteries," *J. Energy Storage*, vol. 6, pp. 95–104, 2016.

[91] S. Santhanagopalan, Q. Guo, P. Ramadass, and R. E. White, "Review of models for predicting the cycling performance of lithium ion batteries," *J. Power Sources*, vol. 156, no. 2, pp. 620–628, 2006.

[92] M. Farkhondeh and C. Delacourt, "Mathematical Modeling of Commercial LiFePO4 Electrodes Based on Variable Solid-State Diffusivity," *J. Electrochem. Soc.*, vol. 159, no. 2, p. A177, 2012.

[93] M. Mastali, M. Kohneh, E. Samadani, R. Fraser, and M. Fowler, "Three-Dimensional Electrochemical Analysis of a Graphite / LiFePO 4 Li-Ion Cell to Improve Its Durability," *SAE Tech. Pap.*, 2015.

[94] M. Mastali, E. Samadani, S. Farhad, R. Fraser, and M. Fowler, “Electrochimica Acta Three-dimensional Multi-Particle Electrochemical Model of LiFePO 4 Cells based on a Resistor Network Methodology,” *Electrochim. Acta*, vol. 190, pp. 574–587, 2016.

[95] S. Panchal, M. Mathew, R. Fraser, and M. Fowler, “Electrochemical thermal modeling and experimental measurements of 18650 cylindrical lithium-ion battery during discharge cycle for an EV,” *Appl. Therm. Eng.*, 2018.

[96] A. Seaman, T.-S. Dao, and J. McPhee, “A survey of mathematics-based equivalent-circuit and electrochemical battery models for hybrid and electric vehicle simulation,” *J. Power Sources*, vol. 256, pp. 410–423, 2014.

[97] E. Samadani *et al.*, “Electrochimica Acta Empirical Modeling of Lithium-ion Batteries Based on Electrochemical Impedance Spectroscopy Tests,” *Electrochim. Acta*, vol. 160, pp. 169–177, 2015.

[98] M. Mathew, Q. H. Kong, J. McGrory, and M. Fowler, “Simulation of lithium ion battery replacement in a battery pack for application in electric vehicles,” *J. Power Sources*, vol. 349, pp. 94–104, May 2017.

[99] K. Murashko, J. Pyrhonen, and L. Laurila, “Three-dimensional thermal model of a lithium ion battery for hybrid mobile working machines: Determination of the model parameters in a pouch cell,” *IEEE Trans. Energy Convers.*, vol. 28, no. 2, pp. 335–343, 2013.

[100] E. Samadani, M. Mastali, S. Farhad, R. A. Fraser, and M. Fowler, “Li-ion battery performance and degradation in electric vehicles under different usage scenarios,” *Int. J. energy Res.*, vol. 40, no. 2015, pp. 379–392, 2015.

[101] Y. Hu, S. Yurkovich, Y. Guezennec, and B. J. Yurkovich, “Electro-thermal battery model identification for automotive applications,” *J. Power Sources*, vol. 196, pp. 449–457, 2010.

[102] X. Lin *et al.*, “A lumped-parameter electro-thermal model for cylindrical batteries,” *J. Power Sources*, vol. 257, pp. 1–11, 2014.

[103] E. Samadani, L. Gimenez, W. Scott, M. Fowler, and R. Fraser, “Thermal Behavior of Two Commercial Li-Ion Batteries for Plug-in Hybrid Electric Vehicles,” *SAE Tech. Pap.*, 2014.

[104] J. Jaguemont, L. Boulon, and Y. Dube, “Characterization and Modeling of a Hybrid-Electric-Vehicle Lithium-Ion Battery Pack at Low Temperatures,” *IEEE Trans. Veh. Technol.*, vol. 65, no. 1, pp. 1–14, Jan. 2016.

[105] X. Liu, Y. He, J. Zhang, and G. Zeng, “A new state-of-charge estimation method for electric vehicle lithium-ion batteries based on multiple input parameter fitting model,” *Int. J. energy Res.*, pp. 23–40, 2017.

[106] E. Samadani, J. Lo, M. Fowler, R. A. Fraser, and L. Gimenez, “Impact of Temperature on the A123 Li-Ion Battery Performance and Hybrid Electric Vehicle Range,” *SAE Tech. Pap.*, 2013.

[107] M. Mastali *et al.*, “Electrochemical-thermal modeling and experimental validation of commercial graphite / LiFePO 4 pouch lithium-ion batteries,” *Int. J. Therm. Sci.*, vol. 129, pp. 218–230, 2018.

[108] I. N. Laboratory, “Battery test manual for plug-in hybrid electric vehicles,” 2008.

[109] W. Dreyer, J. Jamnik, C. Guhlke, R. Huth, J. Moškon, and M. Gaberšček, “The thermodynamic origin of hysteresis in insertion batteries,” *Nat. Mater.*, vol. 9, 2010.

[110] L. Rao and J. Newman, “Heat-Generation Rate and General Energy Balance for Insertion Battery Systems,” *Electrochem. Soc.*, vol. 144, no. 8, pp. 2697–2704, 1997.

[111] M. Mastali, “Electrochemical-Thermal Modeling of Lithium-ion Batteries,” *Univ. Waterloo Thesis*, 2016.

[112] T. M. Bandhauer, S. Garimella, and T. F. Fuller, “A Critical Review of Thermal Issues in Lithium-Ion Batteries,” *J. Electrochem. Soc.*, vol. 158, no. 3, 2011.

[113] K. Jalkanen, T. Aho, and K. Vuorilehto, “Entropy change effects on the thermal behavior of a LiFePO 4 / graphite lithium-ion cell at different states of charge,” *J. Power Sources*, vol. 243, pp. 354–360, 2013.

[114] M. Farag, H. Sweity, M. Fleckenstein, and S. Habibi, “Combined electrochemical , heat generation , and thermal model for large prismatic lithium-ion batteries in real-time applications,” *J. Power Sources*, vol. 360, pp. 618–633, 2017.

[115] J. Sun *et al.*, “Online internal temperature estimation for lithium-ion batteries based on Kalman filter,” *Energies*, vol. 8, no. 5, pp. 4400–4415, 2015.

[116] S. Rodrigues, N. Munichandraiah, and A. K. Shukla, “AC impedance and state-of-charge analysis of a sealed lithium-ion rechargeable battery,” *J. Solid State Electrochem.*, vol. 3, pp. 397–405, 1999.

[117] T. Momma, M. Matsunaga, D. Mukoyama, and T. Osaka, “Ac impedance analysis of lithium ion battery under temperature control,” *J. Power Sources*, vol. 216, pp. 304–307, 2012.

[118] W. Waag, S. Käbitz, and D. U. Sauer, “Experimental investigation of the lithium-ion battery impedance characteristic at various conditions and aging states and its influence on the application,” *Appl. Energy*, vol. 102, pp. 885–897, 2013.

[119] S. J. Moura, N. A. Chaturvedi, and M. Krstic, “Adaptive Partial Differential Equation Observer for Battery Estimation Via an Electrochemical Model,” *J. Dyn. Syst. Meas. Control*, vol. 136, 2014.

[120] L. Zheng, L. Zhang, J. Zhu, G. Wang, and J. Jiang, “Co-estimation of state-of-charge, capacity and resistance for lithium-ion batteries based on a high-fidelity electrochemical model,” *Appl. Energy*, vol. 180, pp. 424–434, 2016.

[121] Y.-H. Chiang, W.-Y. Sean, and J.-C. Ke, “Online estimation of internal resistance and

open-circuit voltage of lithium-ion batteries in electric vehicles," *J. Power Sources*, vol. 196, no. 8, pp. 3921–3932, Apr. 2011.

[122] X. Wei, B. Zhu, and W. Xu, "Internal Resistance Identification in Vehicle Power Lithium-Ion Battery and Application in Lifetime Evaluation," in *2009 International Conference on Measuring Technology and Mechatronics Automation*, 2009, vol. 3, pp. 388–392.

[123] H. Dai, T. Xu, L. Zhu, X. Wei, and Z. Sun, "Adaptive model parameter identification for large capacity Li-ion batteries on separated time scales," *Appl. Energy*, vol. 184, pp. 119–131, 2016.

[124] A. Lievre, A. Sari, P. Venet, A. Hijazi, M. Ouattara-Brigaudet, and S. Pelissier, "Practical online estimation of lithium-ion battery apparent series resistance for mild hybrid vehicles," *IEEE Trans. Veh. Technol.*, vol. 65, no. 6, pp. 4505–4511, 2016.

[125] H. Dai, X. Wei, and Z. Sun, "A new SOH prediction concept for the power lithium-ion battery used on HEVs," *5th IEEE Veh. Power Propuls. Conf. VPPC '09*, pp. 1649–1653, 2009.

[126] Y. Cai, "D-UKF Based State of Health Estimation for 18650 Type Lithium Battery," vol. 0, no. 2, pp. 754–758, 2016.

[127] D. Andre, A. Nuhic, T. Soczka-guth, and D. U. Sauer, "Engineering Applications of Artificial Intelligence Comparative study of a structured neural network and an extended Kalman filter for state of health determination of lithium-ion batteries in hybrid electric vehicles," *Eng. Appl. Artif. Intell.*, vol. 26, no. 3, pp. 951–961, 2013.

[128] Y. Zou, X. Hu, H. Ma, and S. E. Li, "Combined State of Charge and State of Health estimation over lithium-ion battery cell cycle lifespan for electric vehicles," *J. Power Sources*, vol. 273, pp. 793–803, 2015.

[129] E. A. Wan, R. Van Der Menve, and N. W. W. Rd, "The Unscented Kalman Filter for Nonlinear Estimation," pp. 153–158.

[130] W. Waag, C. Fleischer, and D. U. Sauer, "Critical review of the methods for monitoring of lithium-ion batteries in electric and hybrid vehicles," *J. Power Sources*, vol. 258, pp. 321–339, 2014.

[131] H. He, X. Zhang, R. Xiong, Y. Xu, and H. Guo, "Online model-based estimation of state-of-charge and open-circuit voltage of lithium-ion batteries in electric vehicles," *Energy*, vol. 39, no. 1, pp. 310–318, 2012.

[132] S. B. Samsuri, H. Zamzuri, M. Rahman, S. A. Mazlan, and A. Rahman, "Computation cost analysis of extended kalman filter in simultaneous localization & mapping (EKF-SLAM) problem for autonomous vehicle," *J. Eng. Appl. Sci.*, vol. 10, no. 17, pp. 7764–7768, 2015.

[133] G. Madhuri, B. V. Kumar, V. S. Raja, and M. Shasidhar, "Performance Analysis of Adaptive Algorithms for Noise Cancellation," *2011 Int. Conf. Comput. Intell. Commun. Syst. Perform.*, 2011.

[134] M. Berecibar, I. Gandiaga, I. Villarreal, N. Omar, J. Van Mierlo, and P. Van den Bossche, "Critical review of state of health estimation methods of Li-ion batteries for real applications," *Renew. Sustain. Energy Rev.*, vol. 56, pp. 572–587, 2016.

[135] G. Piłatowicz, A. Marongiu, J. Drillkens, P. Sinhuber, and D. U. Sauer, "A critical overview of definitions and determination techniques of the internal resistance using lithium-ion, lead-acid, nickel metal-hydride batteries and electrochemical double-layer capacitors as examples," *J. Power Sources*, vol. 296, pp. 365–376, 2015.

[136] J. Kim and B. H. Cho, "State-of-Charge Estimation and State-of-Health Prediction of a Li-Ion Degraded Battery Based on an EKF Combined With a Per-Unit System," *IEEE Trans. Veh. Technol.*, vol. 60, no. 9, pp. 4249–4260, Nov. 2011.

[137] A. Millner, "Modeling Lithium Ion battery degradation in electric vehicles," in *2010 IEEE Conference on Innovative Technologies for an Efficient and Reliable Electricity Supply*, 2010, pp. 349–356.

[138] A. Farmann, W. Waag, A. Marongiu, and D. U. Sauer, "Critical review of on-board capacity estimation techniques for lithium-ion batteries in electric and hybrid electric vehicles," *J. Power Sources*, vol. 281, pp. 114–130, 2015.

[139] H. Blanke *et al.*, "Impedance measurements on lead – acid batteries for state-of-charge , state-of-health and cranking capability prognosis in electric and hybrid electric vehicles," vol. 144, pp. 418–425, 2005.

[140] D. U. Waag, Wladislaw, Schaeper, Christoph, Sauer, "Self-adapting on-board diagnostic algorithms for lithium-ion batteries," *Adv. Batter. Dev. Automot. Util. Appl. their Electr. Power Grid Integr.*, no. March, 2011.

[141] U. . E. P. Agency, "Detailed Test Information," 2014. [Online]. Available: http://www.fueleconomy.gov/feg/fe_test_schedules.shtml.

[142] PJM, "Ancillary Services," 2017. [Online]. Available: http://www.pjm.com/markets-and-operations/ancillary-services.aspx.

[143] X. H. Rui, Y. Jin, X. Y. Feng, L. C. Zhang, and C. H. Chen, "A comparative study on the low-temperature performance of LiFePO4/C and Li3V2(PO4)3/C cathodes for lithium-ion batteries," *J. Power Sources*, vol. 196, no. 4, pp. 2109–2114, 2011.

[144] W. Scott, "Impact of High Fidelity Battery Models for Vehicle Applications," 2015.

[145] Z. Chen, B. Xia, and C. C. Mi, "A novel state-of-charge estimation method for lithium-ion battery pack of electric vehicles," *2015 IEEE Transp. Electrif. Conf. Expo, ITEC 2015*, pp. 1–6, 2015.

[146] J. Kim and B. H. Cho, "Screening process-based modeling of the multi-cell battery string in series and parallel connections for high accuracy state-of-charge estimation," *Energy*, vol. 57, pp. 581–599, 2013.

[147] R. Xiong, F. Sun, X. Gong, and H. He, "Adaptive state of charge estimator for lithium-ion

cells series battery pack in electric vehicles," *J. Power Sources*, vol. 242, pp. 699–713, 2013.

[148] G. L. Plett, "Efficient Battery Pack State Estimation using Bar-Delta Filtering," in *EVS24 International Battery, Hybrid and Fuel Cell Electric Vehicle Symposiu*, 2016.

[149] H. Dai, X. Wei, Z. Sun, J. Wang, and W. Gu, "Online cell SOC estimation of Li-ion battery packs using a dual time-scale Kalman filtering for EV applications," *Appl. Energy*, vol. 95, pp. 227–237, 2012.

[150] Y. Hua, A. Cordoba-Arenas, N. Warner, and G. Rizzoni, "A multi time-scale state-of-charge and state-of-health estimation framework using nonlinear predictive filter for lithium-ion battery pack with passive balance control," *J. Power Sources*, vol. 280, pp. 293–312, 2015.

[151] L. Zhong, C. Zhang, Y. He, and Z. Chen, "A method for the estimation of the battery pack state of charge based on in-pack cells uniformity analysis," *Appl. Energy*, vol. 113, pp. 558–564, 2014.

[152] W. Weizhong Wang, P. Malysz, D. Deqiang Wang, R. Ran Gu, H. Hong Yang, and A. Emadi, "Efficient multi-cell SOC estimation for electrified vehicle battery packs," in *2016 IEEE Transportation Electrification Conference and Expo (ITEC)*, 2016, pp. 1–5.

[153] L. Ahmadi, M. Fowler, S. B. Young, R. A. Fraser, B. Gaffney, and S. B. Walker, "Energy efficiency of Li-ion battery packs re-used in stationary power applications," *Sustain. Energy Technol. Assessments*, vol. 8, pp. 9–17, Dec. 2014.

[154] X. Zeng, J. Li, and N. Singh, "Recycling of Spent Lithium-Ion Battery: A Critical Review," *Crit. Rev. Environ. Sci. Technol.*, vol. 44, no. 10, pp. 1129–1165, May 2014.

[155] S. Paul, C. Diegelmann, H. Kabza, and W. Tillmetz, "Analysis of ageing inhomogeneities in lithium-ion battery systems," *J. Power Sources*, vol. 239, pp. 642–650, Oct. 2013.

[156] V. M. Smith and G. A. Keoleian, "The Value of Remanufactured Engines: Life-Cycle Environmental and Economic Perspectives," *J. Ind. Ecol.*, vol. 8, no. 1–2, pp. 193–221, Feb. 2008.

[157] Z. H. Jiang, L. H. Shu, and B. Benhabib, "Steady-State Reliability Analysis of Repairable Systems Subject to System Modifications," *J. Mech. Des.*, vol. 121, no. 4, p. 614, 1999.

[158] L. H. Shu and W. C. Flowers, "Reliability Modeling in Design for Remanufacture," *J. Mech. Des.*, vol. 120, no. 4, p. 620, 1998.

[159] M. Dubarry, N. Vuillaume, and B. Y. Liaw, "From single cell model to battery pack simulation for Li-ion batteries," *J. Power Sources*, vol. 186, no. 2, pp. 500–507, Jan. 2009.

[160] J. Li and M. S. Mazzola, "Accurate battery pack modeling for automotive applications," *J. Power Sources*, vol. 237, pp. 215–228, 2013.

[161] M. Dubarry, N. Vuillaume, and B. Y. L. Ã, "Origins and accommodation of cell variations

in Li-ion battery pack modeling," no. December 2009, pp. 216–231, 2010.

[162] M. Paschero, G. L. Storti, A. Rizzi, F. M. F. Mascioli, and G. Rizzoni, "A novel mechanical analogy based battery model for SoC estimation using a multi-cell EKF," Jan. 2016.

[163] C. Truchot, M. Dubarry, and B. Y. Liaw, "State-of-charge estimation and uncertainty for lithium-ion battery strings," *Appl. Energy*, vol. 119, pp. 218–227, 2014.

[164] F. Sun, R. Xiong, and H. He, "A systematic state-of-charge estimation framework for multi-cell battery pack in electric vehicles using bias correction technique," *Appl. Energy*, vol. 162, pp. 1399–1409, 2016.

[165] R. Adany, D. Aurbach, and S. Kraus, "Switching algorithms for extending battery life in Electric Vehicles," *J. Power Sources*, vol. 231, pp. 50–59, 2013.

[166] R. Ugle, Y. Li, and A. Dhingra, "Equalization integrated online monitoring of health map and worthiness of replacement for battery pack of electric vehicles," *J. Power Sources*, vol. 223, pp. 293–305, 2013.

[167] N. Ganesan *et al.*, "Physics based modeling of a series parallel battery pack for asymmetry analysis, predictive control and life extension," *J. Power Sources*, vol. 322, pp. 57–67, 2016.

[168] O. Erdinc, B. Vural, and M. Uzunoglu, "A dynamic lithium-ion battery model considering the effects of temperature and capacity fading," in *2009 International Conference on Clean Electrical Power*, 2009, pp. 383–386.

[169] M. Dubarry and B. Y. Liaw, "Development of a universal modeling tool for rechargeable lithium batteries," *J. Power Sources*, vol. 174, no. 2, pp. 856–860, Dec. 2007.

[170] J. Vazquez-Arenas, M. Fowler, X. Mao, and S. Chen, "Modeling of combined capacity fade with thermal effects for a cycled LixC6–LiyMn2O4 cell," *J. Power Sources*, vol. 215, pp. 28–35, Oct. 2012.

[171] M. A. Seitz, "A critical assessment of motives for product recovery: the case of engine remanufacturing," *J. Clean. Prod.*, vol. 15, no. 11, pp. 1147–1157, 2007.

[172] X. Hu, S. Li, and H. Peng, "A comparative study of equivalent circuit models for Li-ion batteries," *J. Power Sources*, vol. 198, pp. 359–367, Jan. 2012.

[173] H. He, R. Xiong, and J. Fan, "Evaluation of Lithium-Ion Battery Equivalent Circuit Models for State of Charge Estimation by an Experimental Approach," *Energies*, vol. 4, no. 12, pp. 582–598, Mar. 2011.

[174] J. Schmalstieg, S. Käbitz, M. Ecker, and D. U. Sauer, "A holistic aging model for Li(NiMnCo)O2 based 18650 lithium-ion batteries," *J. Power Sources*, vol. 257, pp. 325–334, Jul. 2014.

[175] Y. Zhang, C.-Y. Wang, and X. Tang, "Cycling degradation of an automotive LiFePO4

lithium-ion battery," *J. Power Sources*, vol. 196, no. 3, pp. 1513–1520, Feb. 2011.

[176] A. Cordoba-Arenas, S. Onori, Y. Guezennec, and G. Rizzoni, "Capacity and power fade cycle-life model for plug-in hybrid electric vehicle lithium-ion battery cells containing blended spinel and layered-oxide positive electrodes," *J. Power Sources*, vol. 278, pp. 473–483, 2015.

[177] Y. Zhang, C.-Y. Wang, and X. Tang, "Cycling degradation of an automotive LiFePO4 lithium-ion battery," *J. Power Sources*, vol. 196, no. 3, pp. 1513–1520, Feb. 2011.

[178] L. Zhu, Z. Sun, H. Dai, and X. Wei, "A novel modeling methodology of open circuit voltage hysteresis for LiFePO<inf>4</inf> batteries based on an adaptive discrete Preisach model," *Appl. Energy*, vol. 155, pp. 91–109, 2015.

[179] F. Baronti, N. Femia, R. Saletti, C. Visone, and W. Zamboni, "Preisach modelling of lithium-iron-phosphate battery hysteresis," *J. Energy Storage*, vol. 4, pp. 51–61, 2015.

[180] F. Baronti, N. Femia, R. Saletti, and W. Zamboni, "Comparing open-circuit voltage hysteresis models for lithium-iron-phosphate batteries," in *IECON 2014 - 40th Annual Conference of the IEEE Industrial Electronics Society*, 2014, pp. 5635–5640.